Development and calibration of “calcite rafts” as a proxy for Holocene aquifer conditions in anchialine settings, Quintana Roo, Yucatán Peninsula, Mexico

Development and calibration of "calcite rafts" as a proxy for Holocene aquifer conditions in anchialine settings, Quintana Roo, Yucatán Peninsula, Mexico

SHAWN EDWARD KOVACS
Honours B.Sc. McMaster University

A Thesis

Submitted to the School of Graduate Studies

in Partial Fulfillment of the Requirements

for the Degree

Doctor of Philosophy

McMaster University

© Copyright by Shawn Edward Kovacs, August 2017

McMaster University
Doctor of Philosophy (2017)
Hamilton, Ontario, Canada
School of Geography and Earth Sciences

TITLE:

Development and calibration of "calcite rafts" as a proxy for Holocene aquifer conditions in anchialine settings, Quintana Roo, Yucatán Peninsula, Mexico

AUTHOR: Shawn Edward Kovacs B.Sc. (Honours)
McMaster University

SUPERVISOR: Eduard G. Reinhardt Professor
McMaster University

NUMBER OF PAGES: xvi, 131

ABSTRACT

Coastal karst aquifers are important water resources, often providing the only source of freshwater to coastal communities for agriculture, industrial usage and human consumption. In order to implement management strategies and preventative measures for future perseveration of this resource, it is imperative to understand how coastal groundwater conditions are controlled by the interaction of freshwater/seawater on local and regional scales, but also over recent and past time periods. However, there is a limited resource of published hydrological data on recent aquifer conditions. In the Yucatán Peninsula and other anchialine environments, this lack of information inhibits the understanding of the spatial and temporal interaction of the meteoric and marine water masses. Documenting how the aquifer is responding to forcing mechanisms such as large precipitation events, seasonal cycles and short-term sea level rise (e.g. storm surge) will assist in understanding modern aquifer condition but also the interpretation of paleo-records. Utilization of water level and salinity sensors in strategic positions in the aquifer demonstrate that meteoric water mass salinity varies over wet and dry seasons with the movement of the halocline, but also on a short-term basis though large rainfall events. Salinity in the meteoric water mass is influenced by mixing with the marine water mass during intense precipitation events associated with Hurricane Ingrid (2013), Tropical Storm Hanna (2014) and a series of unnamed events in 2015. During wet periods, induced flow from increase precipitation causes turbulent mixing with the marine water mass, increasing salinity in the upper meteoric lens. On the contrary, during dry periods, mixing is reduced, therefore making the meteoric lens less saline.

This contemporary understanding of meteoric/marine water mass dynamics can be applied to developing and calibrating the geochemical record of calcite rafts, calcite precipitation

at the air-water interface of cave pools, as a hydrological proxy for aquifer conditions. Our monitoring of calcite raft formation, deposition and geochemistry shows that raft accumulations (e.g., raft piles/cones) can offer a good paleoenvironmental archive of changing hydrological conditions. Based on a 2-year observational record, results indicate that calcite raft precipitation/formation occurs continuously but with only minor biases with intense rainfall events altering supersaturation conditions in the surface waters. Testing the use of calcite rafts in sediment cores from Hoyo Negro show that geochemical analyses ($^{87}Sr/^{86}Sr$, $\delta^{18}O$, $\delta^{13}C$, Sr/Ca and Cl/Ca) show that meteoric water mass salinity varied during the Holocene (~ 8.5 Ka – present) likely due to changing rainfall and or cave passage geomorphology, which is coherent with other independent climate records. Prior to this study, calcite rafts have never been considered a paleo-hydrological archive for aquifer conditions, however, the consistency and cross-validation with independent records demonstrates great potential for future paleohydrological reconstructions.

ACKNOWLEDGEMENTS

```
---
title: "Acknowledgments"
author: "Shawn E. Kovacs"
date: '2017-06-05'
output:
  html_document: default
  pdf_document: default
---
```

```{r setup, include=FALSE}
knitr::opts_chunk$set(echo = TRUE)
graphics.off()
rm(list = ls())
```

Please "*Knit* this **R markdown** document" to HTML for an illustrated representation of my academic achievement (*egregia cum laude*):

elölről ...

```{r package_options, echo=TRUE, message=F, warning=TRUE}
if(!require(dplyr)) { install.packages("dplyr"); require(dplyr)} #load dplyr
if(!require(ggplot2)) { install.packages("ggplot2"); require(ggplot2)} #load ggplot2
if(!require(ggthemes)) { install.packages("ggthemes"); require(ggthemes)} #load ggthemes
```

```{r pressure, echo=TRUE}
### START SCRIPT ###
x <- 1:100
y <- -27*0.955^x + 100
z <- sort(sample(seq(as.Date('2012/06/25'), as.Date('2017/06/05'), by="day"),100))
data <- dplyr::data_frame(x,y,z)
### END SCRIPT ###
```

```{r, fig.width=11, fig.height=10, echo=FALSE, message=F}
ggplot(data = data,aes(z, y)) + geom_point() + geom_line() + stat_smooth(span = 0.7) +
labs(title= "Learning Curve", x = "Date", y = "Proficiency", subtitle =
expression(paste(italic("What is a scientist after all? It is a curious man looking through a keyhole, the keyhole of nature, trying to know what's going on (Jacques-Yves Cousteau).")))), caption = "Figure 1. - Special acknowledgement must be given to the individuals who made this lifelong aspiration possible: My Mother, Father, Močiutė, Brother, Sister\n (+the little one on the way), Gang and the love of my life. Credit must also be given to Senelis Paul, Nagymama Ann, Nagypapa Viktor, Nagybácsi\nJoe, and Nagybácsi Victor, who in spirit, provided inspiration for success despite the inherent obstacles. I am forever in their debt for the love,       \nsupport and encouragement – I dedicate this achievement to you. Through perseverance, determination and belief in oneself, anything is \npossible.I would also like to sincerely thank my academic father, Dr. Eduard G. Reinhardt, for the opportunity, supervision as well as                    \nunconditional guidance through my entire academic career – intellectual advice that will continue to assist me in my future endeavors.                    ") + theme_gdocs()
```

```{r, echo=F}
print(sessionInfo())
```

DECLARATION OF ACADEMIC ACHIEVEMENT

CHAPTER 2 – HURRICANE INGRID AND TROPICAL STORM HANNA'S EFFECTS ON THE SALINITY OF THE COASTAL AQUIFER, QUINTANA ROO, MEXICO

For this project that led to subsequent publication in the *Special Issue – Journal of Hydrology: Investigation and Management of Coastal Aquifers*, strategy for sensor placement was completed by S. E. Kovacs, E. G. Reinhardt, C. Werner, F. Devos, C. Le Maillot and S. V. Collins. Sensor download and data retrieval was completed by all authors listed above in addition to numerous volunteers assisting during the 2014 – 2016 Mexico Cave Exploration Project (MCEP) Science gatherings. MCEP and Centro Investigador del Sistema Acuífero de Quintana Roo (CINDAQ) provided logistical support in Mexico, while dive logistics/support was provided by Zero-Gravity Mexico and staff. Hydrolab® CTD profiles from Cenote Angelita and The Pit were provided by Patricia Beddows and Simon Richards. A component of the weather data was collected by S. V. Collins, while the greater part was acquired by S. E. Kovacs. Data harvesting, munging, formatting, analyses and visualization was completed by S. E. Kovacs. Wavelet analyses were completed by M. Stastna and A. Coutino. Manuscript, figures and tables were prepared by S. E. Kovacs, E. G. Reinhardt, C. Werner, M. Stastna and A. Coutino with comments and insight provided by F. Devos, C. Le Maillot and S. V. Collins.

CHAPTER 3 – SEASONAL TRENDS IN CALCITE RAFT FORMATION FROM CENOTES RAINBOW, FENO AND MONKEY DUST, QUINTANA ROO, MEXICO – IMPLICATIONS FOR PALEOENVIRONMENTAL STUDIES

The Calcite Raft Monitoring Project (CRMP) which consisted of monitoring coastal karst basins (cenotes) within the Quintana Roo region was proposed by S. E. Kovacs and E. G. Reinhardt. Field implementation, sensor placement, and retrieval of samples (i.e. calcite rafts, surface water samples, sediment traps) was fulfilled by S. E. Kovacs E. G. Reinhardt, C. Werner, F. Devos, C. Le Maillot, and 2014 – 2016 MCEP Science volunteers. Tasks would have included but not limited to monitoring setup, maintenance, data downloads and disassemble. Underwater photographs of Cenote Feno, with Cameron Russo present, were provided by Ali Perkins (Inspired to Dive Photography). All laboratory samples consisting of calcite rafts, surface water aliquots, and organic/inorganic cave sediments were processed by S. E. Kovacs. All data processing, formatting, aggregation and visualization was completed through a R-script designed by S. E. Kovacs. All figures were drafted by S. E. Kovacs with the aid/insight of E. G. Reinhardt. S. E. Kovacs and E. G. Reinhardt prepared the scientific manuscript for publication (*Paleogeography, Paleoclimatology, Paleoecology*) with comments and feedback provided by C. Werner, S. T. Kim, F. Devos, and C. Le Maillot.

CHAPTER 4 – CALCITE RAFT GEOCHEMISTRY AS A PROXY FOR HOLOCENE AQUIFER CONDITION IN HOYO NEGRO, QUINTANA ROO, MEXICO

For this manuscript, field data collection consisted of a joint effort from S. E. Kovacs, E. G. Reinhardt, J. C. Chatters, D. Rissolo, S. V. Collins, A. Nava Blank, A. Alvarez, R. Chavez and P. Luna Erreguerena. This comprised of cave surveying, cinematography, sediment cores, cave sediment (both organic and inorganic) samples and water aliquots. Laboratory samples were analyzed by S. E. Kovacs and J. C. Chatters. All data processing and formatting was completed by S. E. Kovacs. Figures were conscripted by S. E. Kovacs, E. G. Reinhardt. Cave map and 3-D model views were provided by A. Nava Blank, A. Alvarez, R. Chavez and D. Rissolo. Manuscript was prepared by S. E. Kovacs and E. G. Reinhardt and revised by J. C. Chatters, D. Rissolo, H. P. Schwarcz and S. T. Kim. This project was conducted under the auspices of the Subdirección de Arqueología Subacuática of the Instituto Nacional de Antropología e Historia (INAH), and with the permission of the Consejo de Arqueología del INAH. Manuscript was submitted to *Quaternary Science Reviews* (QSR) for publication.

TABLE OF CONTENTS

ABSTRACT ..... **iii**

ACKNOWLEDGEMENTS ..... **v**

DECLARATION OF ACADEMIC ACHIEVEMENT ..... **vi**

TABLE OF FIGURES ..... **xii**

LIST OF TABLES ..... **xvi**

CHAPTER 1 – INTRODUCTION ..... **- 1 -**

CHAPTER 2 – HURRICANE INGRID AND TROPICAL STORM HANNA'S EFFECTS ON THE SALINITY OF THE COASTAL AQUIFER, QUINTANA ROO, MEXICO ..... **- 5 -**

2.1 ABSTRACT ..... **- 6 -**

2.2 INTRODUCTION ..... **- 7 -**

2.3 STUDY AREA ..... **- 8 -**

2.3.1 REGIONAL GEOLOGY AND HYDROLOGIC SETTING ..... - 8 -

2.4 CLIMATE ..... **- 10 -**

2.4.1 HURRICANE INGRID – 2013 ..... - 10 -

2.4.2 TROPICAL STORM HANNA – 2014 ..... - 11 -

2.5 MATERIALS AND METHODS ..... **- 12 -**

2.5.1 MONITORING STATION LOCATION ..... - 12 -

2.5.2 SALINITY AND WATER LEVEL DATA ..... - 13 -

2.5.3 CLIMATE DATA ..... - 14 -

2.6 RESULTS AND DISCUSSION ..... **- 15 -**

2.6.1 PRECIPITATION ..... - 15 -

2.6.2 GROUNDWATER LEVELS ..... - 15 -

2.6.3 METEORIC WM SALINITY ..... - 16 -

2.6.3.1 METEORIC WM CHARACTERISTICS ..... - 16 -

2.6.3.2 YAX CHEN SALINITY TRENDS ..... - 18 -

2.6.3.3 LARGE-SCALE RAINFALL EVENTS ..... - 20 -

2.6.3.4 PERIODICITY OF THE SALINITY DATA ..... - 21 -

2.7 CONCLUSIONS ..... **- 22 -**

2.8 ACKNOWLEDGEMENTS ..... **- 23 -**

2.9 REFERENCES ..... **- 24 -**

2.10 TABLES ..... **- 28 -**

2.11 FIGURES ..... **- 29 -**

CHAPTER 3 – SEASONAL TRENDS IN CALCITE RAFT FORMATION FROM CENOTES RAINBOW, FENO AND MONKEY DUST, QUINTANA ROO, MEXICO - IMPLICATIONS FOR PALEOENVIRONMENTAL STUDIES ..... **- 40 -**

3.1 ABSTRACT ..... **- 40 -**

3.2 INTRODUCTION ..... **- 41 -**

3.2.1 CALCITE RAFTS ..... - 42 -

3.3 STUDY AREA ..... **- 44 -**

3.3.1 CLIMATE ..... - 46 -

3.4 MATERIALS AND METHODS ..... **- 47 -**

3.4.1 SITE CHARACTERISTICS ..... - 47 -

3.4.2 SENSORS ..... - 48 -

3.4.2.1 AIR TEMPERATURE (°C) AND RELATIVE HUMIDITY (%) ..... - 48 -

3.4.2.2 SALINITY (ppt) AND WATER TEMPERATURE (°C) - 48 -
3.4.2.3 WATER LEVEL (m) - 49 -
3.4.2.4 PRECIPITATION DATA (mm) - 49 -
3.4.2.5 CALCITE RAFT SURFACE AREA (%) - 50 -
3.4.2.6 SEDIMENT TRAPS (g) - 51 -
3.5 RESULTS - 52 -
3.5.1 PRECIPITATION - 52 -
3.5.2 AIR TEMPERATURE (°C) AND RELATIVE HUMIDITY (%) - 53 -
3.5.3 WATER TEMPERATURE (°C) - 53 -
3.5.4 WATER LEVEL (m) - 54 -
3.5.5 SALINITY (ppt) - 54 -
3.5.6 CALCITE RAFT SURFACE ABUNDANCE (%) - 55 -
3.5.7 SEDIMENT TRAP ACCUMULATION (g) - 56 -
3.6 DISCUSSION - 57 -
3.6.1 CALCITE RAFT FORMATION - 57 -
3.6.2 IMPLICATIONS FOR PALEOENVIRONMENTAL STUDIES - 58 -
3.7 CONCLUSIONS - 59 -
3.8 ACKNOWLEDGEMENTS - 60 -
3.9 REFERENCES - 61 -
3.10 TABLES - 65 -
3.11 FIGURES - 66 -

CHAPTER 4 – CALCITE RAFT GEOCHEMISTRY AS A HYDROLOGICAL PROXY FOR HOLOCENE AQUIFER CONDITION IN HOYO NEGRO, QUINTANA ROO, MEXICO - 77 -
4.1 ABSTRACT - 77 -
4.2 INTRODUCTION - 78 -
4.2.1 HOYO NEGRO (HN) - 79 -
4.2.2 HYDROLOGICAL SETTING - 81 -
4.2.3 CARIBBEAN SEA LEVEL AND GROUNDWATER LEVEL - 82 -
4.2.4 CALCITE RAFTS - 83 -
4.2.5 GEOCHEMICAL PROXIES OF PALEOSALINITY - 84 -
4.3 METHODOLOGY - 85 -
4.3.1 RADIOCARBON AGE DATING - 87 -
4.4 RESULTS - 88 -
4.4.1 AGE MODELS - 88 -
4.4.2 ISOTOPIC PROXIES: ^{87}Sr / ^{86}Sr, $\delta^{18}O$ AND $\delta^{13}C$ - 89 -
4.4.3 ELEMENTAL PROXIES Cl/Ca AND Sr/Ca - 90 -
4.4.4 DIAGENESIS - 91 -
4.5 DISCUSSION - 92 -
4.5.1 WATER LEVEL AND CALCITE RAFT DISTRIBUTION IN HN and IB - 92 -
4.5.2 AQUIFER SALINITY AND RELATIONSHIP WITH WET AND DRY PERIODS - 94 -
4.5.2.1 CONSISTENCY BETWEEN GEOCHEMICAL PROXIES - 94 -
4.5.2.2 HYDROLOGICAL IMPLICATIONS - 95 -
4.6 CONCLUSIONS - 99 -
4.7 ACKNOWLEDGMENTS - 100 -
4.8 REFERENCES - 101 -
4.9 TABLES - 106 -
4.10 FIGURES - 115 -

CHAPTER 5 – CONCLUSIONS - 126 -

REFERENCES.....- 129 -

TABLE OF FIGURES

CHAPTER 2

Fig. 1 – Study area along the Caribbean Coast of the Yucatán Peninsula, Mexico. Filled black squares denote the position of the weather stations and the red hatched location demarks the study area.

Fig. 2 – Location of monitoring sites used in this study.

Fig. 3 – Time series plots from May 2012 to 2016 (GMT) for: 1) precipitation (mm) from Cancun, Cozumel and Sian Ka'an and Puerto Aventuras weather stations; 2) Yax Chen groundwater level (m) and salinity (ppt) from the two monitoring sites (H2S, −9.14 and −10.36 m depth; ISOD 2, −9.14 and −10.06 m depth). Precipitation and water level are plotted as departure from the mean over the analysis period while salinity (ppt) is plotted as 30-min time intervals. Monthly trends are also plotted which are monthly mean departure values. Gaps in the records are due to sensor malfunction and battery depletion, and flat-lined data (salinity) is due the sensor going out of range (>9 ppt). Hurricanes (orange) and tropical storms (blue) are highlighted over the analysis period.

Fig. 4 – Cross-plots showing the relationship between the mean monthly precipitation (mm) and water level (m) from the weather stations and monitoring sites. Mean values best represent seasonal changes over the analysis period.

Fig. 5 – Hydrolab® CTD (MS5) profiles of salinity (ppt) from various cenotes and caves in the area. Profiles measured over the analysis period showing the depth of the halocline moving towards the coast (Angelita to Ponderosa). Arizona and Lil Chen are in the Yax Chen cave system and close to our two monitoring stations (H2S and ISOD2).

Fig. 6 – Cross-plot showing the halocline depth (m) relationship with distance from the coast (km) which increases by −1.6 m/km.

Fig. 7 – Hydrolab® CTD (MS5) profiles of salinity (ppt) with depth (m) along the sensor chain for monitoring sites (H2S and ISOD2) in Yax Chen over various time periods.

Fig. 8 – a) Cross-plots between daily meteoric WM salinity (ppt) and departure from mean water depth (m) from H2S and ISOD2. Slope of lower threshold line represents seasonal change in salinity with wet and dry periods, and higher salinity departures from this threshold (arrow) represent mixing during precipitation events. b) Data with outlying values removed.

Fig. 9 – Cross-plots between monthly mean salinity (ppt) and water depth (m) as well as cross plots between monthly standard deviation of these two parameters. Negative relationships with the mean represents the seasonal mixing, while the positive relationship with standard deviation represents the effects of rapidly changing water level (precipitation events) on salinity and mixing.

Fig. 10 – Detailed time-series plots (GMT) spanning three rainfall events: Hurricane Ingrid in 2013, Tropical Storm Hanna, 2014, and an un-named series of events in 2015. Plots use the same parameters as described in Fig. 3.

Fig. 11 – The departure from mean water depth (m) time series (top), the global wavelet spectrum (GWS) (left) and the wavelet power spectrum (right) for H2S −9.14 m salinity records. The GWS is a temporal average of the wavelet spectrum and can be considered as an approximation of their respective Fourier spectrum. Within the GWS, the hatched line represents the mean red noise spectrum, while the arrows indicate peaks in the power of the GWS. The wavelet power spectrum plot compares the period to time with a cone-of-influence indicated by the green contour (results outside this area are affected by boundaries and should not be considered as valid) and 95% confidence interval compared to the background red noise indicated by the blue contour.

CHAPTER 3

Fig. 1 – Regional map of the Yucatán Peninsula (Mexico) showing the study area.

Fig. 2 – Location of monitoring stations (red circles; Rainbow = RainB, Feno, Monkey Dust = MonkD) and Hydrolab® CTD (MS5) profiles (yellow triangles).

Fig. 3 – Hydrolab® CTD (MS5) profiles showing WM characteristics for respective locations. Dates represented as day, month and year.

Fig. 4 – a) Monitoring station sensor placement (Cenote Feno). b) Cenote Feno showing sediment trap placements. c) Underwater perspective of sensor and sediment trap position.

Fig. 5 – a) Time lapse photographs of monitoring sites showing range of calcite raft surface areas. b) Example of outlining process for surface area estimates (1 – 3).

Fig. 6 – Time series plots from May 2014 to 2016 (GMT) for: Cozumel precipitation (mm), air temperature (°C), relative humidity (%), calcite raft surface area (%, plotted as the mean value of the over/under estimates of surface area), meteoric WM salinity (ppt; ~ 30 cm depth), water temperature (°C), water level (m, ± from mean over study period).

Fig. 7 – Correlation matrix of time-series data which has been aggregated to monthly values to emphasize seasonal trends. Upper right portion represents correlation coefficients of each monitoring site as well as collectively together (Cor.). Each relationship is also colour coordinated based on the strength of the collective Cor. Coefficient. Strong positive correlations are represented by the darker shades of green, strong negative correlations are represented by the darker shades of orange, with weaker associations in between represented by the yellowish shade. Diagonally, when each variable is cross-referenced with itself, the data represents a density plot. The bottom portion represents

calculated coefficients of determination represented by r^2, explaining the portion of variance in the dependent variable is predictable from the independent variable.

Fig. 8 – Cross-plots between daily meteoric WM salinity (ppt) and departure from mean water depth (m) from Rainbow, Feno and Monkey Dust. Slope of lower threshold line represents seasonal change in salinity with wet and dry periods, and higher salinity departures from this threshold (arrow) represent mixing during precipitation events. Relationship is well defined in Cenote Rainbow, but less so in Feno and Monkey Dust.

Fig. 9 – Total sediment (g ± 1 std) accumulated in the 5 traps over six month periods.

Fig. 10 – Detailed time-series plots (GMT) spanning three precipitation events: a) T.S. Hanna (2014), b) Precipitation Event #2 (PE2) and c) Precipitation Event #3 (PE3). Plots use the same parameters as described in Fig. 6.

Fig. 11 – Time-series records (GMT) showing interrelationship between the three monitoring sites (Blue = Rainbow, Red = Feno and Green = Monkey Dust).

CHAPTER 4

Fig. 1 – Map showing the geographical position of HN, other known deep karst basins (> 30 m water depth), and additional cenotes used in this study. Bathymetric contours are represented in meters. Inset shows location of Cariaco Basin (Venezuela) and the summer/winter position of the Atlantic Intertropical Convergence Zone (ITCZ).

Fig. 2 – Cross-section of the cave system showing core locations. Depths are relative to local water level which is ~ 1 - 2 m above msl (see text for details). Inset shows a plan view of cave passages connecting to HN and cenotes in the immediate area.

Fig. 3 – HydroLab™ physico-chemical water mass profiles recorded in HN. The halocline transition zone is shown as a hatched line. Depths are relative to local water level.

Fig. 4 – Compilation of relative sea-level data used to infer flooding history of HN. Depths are in meters relative to mean sea-level (msl). Data includes peat and coral records (Medina-Elizalde, 2013; Milne and Peros, 2013). The red hatch line represents a linear extrapolation for determining initial flooding (inundation) of the HN. The blue hatch line represents the global relative sea level model (Medina-Elizalde, 2013) while light blue fill represents the glacial isostasy adjustment-corrected model for relative sea level rise (Bard et al., 2010).

Fig. 5 – Scanning electron microscope (SEM) images showing cross-sectional profiles through calcite rafts from varying depths in C9. Depths were selected at random A) 1-2 cm interval, B) 11-12cm interval, C) 24-25cm interval and D) 33-34cm interval.

Fig. 6 – Underwater photomosaic of HN compiled from 2200 images aligned on a 3-D model and projected in 2-D. Detailed 3-D image shows the geometry of the calcite raft pile and core locations (C9 and C10). Pit bottom is ~ 62 min diameter.

Fig. 7 – Salinity mixing curve empirically compiled with salinity (ppt) and $^{87}Sr/^{86}Sr$ measured from calcite rafts precipitating in nearby cenotes.

Fig. 8 – Reservoir correction based on paired seed and calcite raft radiocarbon ages from selected intervals using cores C4 and C9 from this study, as well as cores from Collins et al. (2015), (C3, C5, C6; 2015; Table 1).

Fig. 9 – Age Models of IB-C4 and HN-C9 produced using Clam 2.1 (R; Blaauw, 2010; Reimer et al., 2013). Grey area represents calibrated age ranges (yrs. BP) at 2σ confidence intervals.

Fig. 10 – Correlation between Cl/Ca and Sr/Ca data in C9 and C10. C9 was analyzed at 1 cm resolution vs. C10 which was intact, and analyzed sampled at 200 μm. Correlation coefficients (r value) between C9 and C10 are also shown. The optical and radiographic image of C10 shows slightly inclined bedding and laminae which is a reflection of calcite rafts accumulating from a point source and forming a cone-shaped pile. There were no cemented or indurated layers within the core.

Fig. 11 – Geochemical data for IB and HN plotted vs age (note different scales for C4 and C9) and comparisons with the (Ti) record from the Cariaco Basin (see Fig. 1 for geographical position; Haug et al., 2001) and Lake Miragoane in Haiti (Hodell et al., 1991). Inset figure provides reference to $^{87}Sr/^{86}Sr$ and salinity based on measured values.

LIST OF TABLES

CHAPTER 2

Table 1 – Summary statistics of precipitation data. Columns are as follows: Total precipitation represents the collective sum from Cancun, Cozumel, and Sian Ka'an and Puerto Aventuras weather stations, standard deviation (St.D.) as well as max daily sum precipitation (mm) from the recording weather stations.

CHAPTER 3

Table 1 – Total sediment trap (n = 5) weights (g ± 1 std) for each site over the collection period.

Table 2 – Sediment accumulation rates estimates for a 5.96 cm diameter core tube.

CHAPTER 4

Table 1 – Radiocarbon results from Ich Balam and HN.

Table 2 – Measured DIC in the water column of HN.

Table 3 – IB-C4 Geochemical data.

Table 4 – HN-C9 Geochemical data

CHAPTER 1 – INTRODUCTION

The coastal anchialine aquifer of the Yucatán Peninsula has been used as a primary source of potable water for both human consumption and agricultural means since the inception of coastal communities as early as the Late Pleistocene/Early Holocene era (Back, 1995; Chatters et al., 2014; Gonzalez et al., 2003; Veni, 1990). The limestone landscape of the Yucatán is characteristic of high permeability and porosity as a result of extensive karstification and other processes such as mixing-zone dissolution and glacioeustacy (Smart et al., 2006). During precipitation events, rainwater infiltrates though the porous substrate (vadose zone) directly to the unconfined coastal aquifer beneath. Likewise, as in other anchialine settings (coastal tidally-influenced subterranean estuary; see revised definition in Bishop et al., 2015), the aquifer is stratified where fresh groundwater forms a distinct water mass (meteoric lens) positioned on top of the intruding marine water mass, separated by a halocline (or pycnocline) due to density differences (Kambesis and Coke, 2013; Perry et al., 2003). Due to the porous nature of the karst resulting in subterranean drainage, surface water bodies are absent in the region (Metcalfe et al., 2000). Therefore, the fresh groundwater mass is the main source and supply of potable water for human consumption, industrial procedures and agricultural usage (Escolero et al., 2002). Water quality data has shown the effects of urbanization (exceeding the Mexican Drinking Water Standards; Alcocer et al., 1998) and the aquifers susceptibility to anthropogenic (Metcalfe et al., 2011) and saltwater contamination (Marin and Perry, 1994), which is of increasing concern with forecasted urban expansion (Municipalidad de Solidaridad, 2005). Despite these increased anthropogenic pressures on the aquifer, there remains a lack of understanding of the interaction between meteoric and marine water mass through time.

Currently, the basis of our understanding comes from short-term instrumental records which numerical models rely upon (Collins et al., 2015a, 2015b; Coutino et al., 2017; Kovacs et al., 2017a). Yucatán hydrogeology acts on different spatial (regional and local) as well as temporal time scales (Neuman and Rahbek, 2007). However, it is recognized that there is a gap in knowledge in how these variables are interconnected over time (van Hengstum et al., 2010), due to the lack of information on larger scale changes such as frequency and intensity of precipitation events (eg. hurricanes) and sea-level change (Alley, 2001; van Hengstum et al., 2016, 2013).

The coastal phreatic caves of Quintana Roo are considered to be hydrologically open-systems as groundwater predominately flows towards the ocean (Smart et al., 2006), with hydraulic gradients (considered as low) on the scale of 1–10 cm/km (Beddows, 2004; Gondwe et al., 2010; Moore et al., 1992). Circulation of the meteoric and marine water masses are unique, as the meteoric water mass flows coastward (one dominant direction) whereas the underlying marine water mass also flows in a landward direction (Fleury et al., 2007; Whitaker and Smart, 1990). The geochemistry of the two water masses are distinct; the meteoric water mass has a salinity of 1–7 parts per thousand (ppt) and an average temperature of ~25.0 °C, while the marine water mass has a 95% full marine salinity (35 ppt) and mean temperatures of ~27 °C (Stoessell, 1995; Stoessell and Coke, 2006). The depth of the transition zone (halocline) that separates these water masses (meteoric and marine) is a function of distance from the coast, increasing in depth as distance inland from the coast becomes greater (Smart et al., 2006; Werner, 2007). For the zone that is 0–0.4 km from the coast, Beddows (2004) documented that due to low conductivity (restricted size of the conduits) the salinity gradient is steep (referred to as mixing zone; Beddows, 2004). Whereas, the zone that encompasses >0.4 – 10 km (and in areas of high

conduit density), the gradient is less extreme and the halocline position was found to be lower than the predicted Ghyben-Herzberg principle (Beddows, 2004). A mixed layer below the freshwater lens may also be present close to the coast (<10 km) due to tidal mixing between the meteoric and marine water masses (Beddows, 2004; Beddows et al., 2007).

Records (i.e. microfossil, geochemical) obtained from sediment push-cores extracted phreatic cave environments have provided insight to paleoclimate and paleohydrological conditions, but only if processes influencing sedimentation were understood (van Hengstum et al., 2015, 2011). Limited knowledge regarding sedimentation sources, rates, microfossil transport, and other sedimentation processes hampered initial studies in the Aktun Ha cave system (Gabriel et al., 2009; van Hengstum et al., 2010). Once a karst window (collapse to the surface) forms, this initiates two important sedimentation processes: surface runoff of terrestrial organic matter / debris and calcite rafts to precipitate at the air-water interface as degassing can occur (Smart et al., 2006). For the former, Collins et al. (2015b) recognized the role of overlaying vegetation (mangrove type vs. forest) and cenote size (i.e. area for primary productivity to occur) on sediment accumulation through monitoring the sources of sediment and accumulation in the Yax Chen cave system (Ox Bel Ha; see references within for full description). The latter, despite its presence and abundance throughout the Yucatán, research focused on calcite raft sedimentation, geochemistry and potential for a paleo-proxy has received little to no attention. Calcite ($CaCO_3$) raft deposits form at the air-water interface of cave pools as a results of CO_2 degassing and/or evaporation (Taylor et al., 2004; Taylor and Chafetz, 2004; SEM photographs Kovacs et al., 2017b; van Hengstum et al., 2015, 2011). Based on the same systematics as speleothem formation, calcite precipitating at the air-water interface could offer additional insight to paleo-hydrological reconstructions (Taylor and Chafetz, 2004).

This dissertation is divided into three manuscripts for future publication. The first examines monitoring data collected from stations H2S and ISOD located within the Yax Chen Cave System (a segment of the greater Sistema Ox Bel Ha which is the longest underwater cave system in the world with > 270 174 m explored passages; Quintana Roo Speleological Survey, 2017) to determine the seasonal (wet and dry period) interaction between the meteoric and marine water masses. In addition, large short-term precipitation events such as hurricanes and tropical storms are examined to determine the response of the aquifer and the effect of mixing between the water masses.

The second manuscript characterizes environmental factors influencing calcite raft surface abundance and accumulations rates and their temporal trends (i.e. seasonality or environmental conditions that influence formation) to determine if there is any bias affecting their utility as a paleo-archive. Three monitoring sites in Cenotes Rainbow, Feno and Monkey Dust recorded environmental variables (precipitation, water depth, air and water temperature, relative humidity and salinity), time-lapse photography was used to document trends in calcite raft surface area, and sediment traps recorded sedimentation rates to the bottom.

The last manuscript examined the utilization of calcite raft geochemistry as a paleohydrological proxy in Hoyo Negro and Ich Balam. Multiple geochemical analyses including $^{87}Sr/^{86}Sr$, $\delta^{18}O$, $\delta^{13}C$, Sr/Ca and Cl/Ca were evaluated and utilized in this study, in addition to radiocarbon geochronology. Results show that calcite raft accumulations do record changing aquifer condition over long timescales (i.e. the Holocene) showing great potential in future studies.

CHAPTER 2 – HURRICANE INGRID AND TROPICAL STORM HANNA'S EFFECTS ON THE SALINITY OF THE COASTAL AQUIFER, QUINTANA ROO, MEXICO

*Manuscript published: (*doi:10.1016/j.jhydrol.2017.02.024)

Journal of Hydrology: Special Issue on Investigation and Management of Coastal Aquifers

Shawn E. Kovacs [a]*, Eduard G. Reinhardt [a], Marek Stastna [b], Aaron Coutino [b], Christopher Werner [c], Shawn V. Collins [d], Fred Devos [e], Christophe Le Maillot [e]

[a] McMaster University, School of Geography and Earth Sciences, Hamilton, Ontario, L8S 4K1, Canada

[b] University of Waterloo, Department of Applied Mathematics, Waterloo, Ontario, N2L 3G1, Canada

[c] Woodville Karst Plain Project, FL, USA

[d] Clarion University, Department of Biology and Geosciences, Clarion, Pennsylvania, 16214, USA

[e] Mexico Cave Exploration Project (MCEP), Centro Investigador del Sistema Acuifero de Quintana Roo A.C. (CINDAQ), Global Underwater Explorers (GUE), Mexico

* Corresponding author at: McMaster University, School of Geography and Earth Sciences, Hamilton Ontario, L8S 4K1, Canada. Email address: kovacs2@mcmaster.ca

Highlights:

- First long-term record (4-years) of groundwater salinity in the Yucatán.
- Salinity of the meteoric water mass increases with large precipitation events.
- Precipitation induced flow causes mixing with marine water mass.

Keywords: Hurricanes; Coastal karst aquifers; Yucatán; Halocline; Salinity; Potable water

2.1 ABSTRACT

There is a lack of information on aquifer dynamics in anchialine systems, especially in the Yucatán Peninsula of Mexico. Most of our knowledge is based on "spot" measurements of the aquifer with no long-term temporal monitoring. In this study spanning four years (2012–2016), sensors (water depth and conductivity (salinity)) were deployed and positioned (−9 and −10 m) in the meteoric Water Mass (WM) close to the transition with the marine WM (halocline) in 2 monitoring sites within the Yax Chen cave system to investigate precipitation effects on the salinity of the coastal aquifer. The results show variation in salinity (<1 ppt) of the freshwater over seasonal cycles of wet and dry (approx. 6.5–7.25 ppt), depending on the position of the halocline. The aquifer response to larger precipitation events (>95 mm) such as Hurricane Ingrid (2013) and Tropical Storm Hanna (2014) shows meteoric water mass salinity rapidly increasing (approx. 6.39 to >8.6 ppt), but these perturbations have a shorter duration (weeks and days). Wavelet analysis of the salinity record indicates seasonal mixing effects in agreement with the wet and dry periods, but also seasonal effects of tidal mixing (meteoric and marine water masses) occurring on shorter time scales (diurnal and semi-diurnal). These results demonstrate that the salinity of the freshwater lens is influenced by precipitation and turbulent mixing with the marine WM. The salinity response is scaled with precipitation; larger more intense rainfall events (>95 mm) create a larger response in terms of the magnitude and duration of the salinity perturbation (>1 ppt). The balance of precipitation and its intensity controls the temporal and spatial patterning of meteoric WM salinity.

2.2 INTRODUCTION

The regional geology of the Yucatán Peninsula of Mexico consists of biogenic limestone that accumulated during the Cenozoic era (Ward et al., 1985). This limestone has high permeability and porosity (Bauer-Gottwein et al., 2011). The landscape has been extensively karstified by the interaction of mixing-zone hydrology, littoral processes, and glacioeustacy (Smart et al., 2006). As a result, precipitation (i.e. rainwater) percolates though the porous substrate into the underlying unconfined coastal aquifer, where this meteoric water forms a distinct Water Mass (WM) positioned on top of the intruding marine WM from the coast. Due to density differences the WMs are separated by a halocline (or pycnocline) which is a sharp transition zone between the water bodies (anchialine; Kambesis and Coke, 2013; Perry et al., 2003). Due to the nature of the subterranean drainage as well as the low-lying topography, surface water bodies and streams are absent or very limited in the region (Metcalfe et al., 2000). For this reason, the main source of freshwater for human consumption in addition to industrial and agricultural usage is supplied from groundwater (Escolero et al., 2002).

Groundwater is sensitive and susceptible to contamination (Ford and Williams, 2013; Vesper et al., 2001), including both anthropogenic (Metcalfe et al., 2011) and saltwater contamination (Marin and Perry, 1994). Recent water quality data has shown the effects of urbanization, with groundwater contaminated with fecal coliform and nitrates near towns and developments which are often near or exceed the Mexican Drinking Water Standards (Alcocer et al., 1998; Metcalfe et al., 2011; Pacheco et al., 2001). This is of increasing concern, as development and planned expansion of tourism projects is projected to increase ten-fold over the next two decades (Municipalidad de Solidaridad, 2005). Increased groundwater usage with urban

development and agriculture may contribute to marine intrusion and salinization of groundwater (Alcocer et al., 1998; Back and Hanshaw, 1970; Delgado et al., 2010).

Despite these increased anthropogenic pressures on groundwater in the Yucatán, there remains a lack of information on how the meteoric WM and marine WM interact over seasonal cycles or large scale weather events (i.e. hurricanes), and there is no long-term monitoring data on which to base predictions. Here we present 4-years of monitoring data (salinity, water level and precipitation) showing seasonal forcing of the aquifer but also the effects of large rainfall events (hurricanes and tropical storms). This study is important, as it is the longest record available for testing numerical modeling results (Coutino et al., 2017), but also for interpreting paleo-environmental records of groundwater response to climate change (i.e. van Hengstum et al., 2010). The paleo-records can provide long-term perspective on groundwater condition, spanning millennia of wet/dry periods but also the effects of sea-level change and periods of more intense hurricane activity (van Hengstum et al., 2016, 2013). Atlantic hurricane frequency is projected to increase with a warmer climate due to greenhouse gas emissions (Sobel et al., 2016) and it is important to understand how the coastal aquifer will respond, so that informed management strategies, and preventative measures can be developed for the Mexican Caribbean (Manuel-Navarrete et al., 2011). An integrated approach using monitoring, modeling and long-term paleo data can provide that understanding, however, there is a lack of available research to base predictions upon.

2.3 STUDY AREA

2.3.1 REGIONAL GEOLOGY AND HYDROLOGIC SETTING

The Yucatán Peninsula is situated south of the Gulf of Mexico and West of the Caribbean Sea (Fig. 1). Regional topography is characterized by low lying limestone with high net

permeability, allowing for precipitation to infiltrate through the vadose zone and into the underlying unconfined aquifer (Beddows et al., 2007; Coke, 1991; Stoessell, 1995). The coastal phreatic caves are considered as hydrologically open-systems as the flow of the groundwater predominately flows towards the ocean (Smart et al., 2006), with hydraulic gradients (considered as low) on the scale of 1–10 cm/km (Beddows, 2004; Gondwe et al., 2010; Moore et al., 1992). The aquifer is stratified, containing the meteoric WM that floats above the denser marine WM that penetrates inland from the coast (Back and Hanshaw, 1970; Perry et al., 1989). The geochemistry of the two WMs is distinct, the meteoric WM has a salinity of 1–7 parts per thousand (ppt) and average temperature of ~25.0 °C, while the marine WM has a 95% full marine salinity (35 ppt) and mean temperatures of ~27 °C (Stoessell, 1995; Stoessell and Coke, 2006). External forcing mechanisms influencing the flow dynamics on a regional scale have been ascribed to fluctuations in sea-level and hydraulic head differences (Smart et al., 2006; Whitaker and Smart, 1990). Circulation of the WMs (meteoric and marine) are unique, as the meteoric WM flows coastward (one dominant direction) whereas the underlying marine WM flows in a landward direction (Whitaker and Smart, 1990). A halocline, or transition zone, separates the meteoric and marine WM and the depth of the halocline increases with distance inland from the coast (Smart et al., 2006; Werner, 2007). For the zone that is 0–0.4 km from the coast, Beddows (2004) documented that due to low conductivity (restricted size of the conduits) the salinity gradient is steep (referred to as mixing zone; Beddows, 2004). Whereas, the zone that encompasses >0.4 – 10 km (and in areas of high conduit density), the gradient is less extreme and the halocline position was found to be lower than the predicted Ghyben-Herzberg principle (Beddows, 2004). A mixed layer below the freshwater lens may also be present close to the coast

(<10 km) due to tidal mixing between the meteoric and marine water masses (Beddows, 2004; Beddows et al., 2007).

2.4 CLIMATE

Based on the Köppen-Geiger climate classification (Kottek et al., 2006), the Yucatán climate is tropical with cooler dry and warmer wet seasons, influenced by the position of the Intertropical Convergence Zone (ITCZ; Hastenrath and Greischar, 1993; Hughen et al., 1996). The ITCZ is the zonal belt of low pressure near the equator that encompasses subtropical high-pressure convergence of high-pressure belts from the Northern and Southern Hemisphere, consequently driving large scale precipitation patterns experienced within the tropics (Hastenrath, 2012; Peterson et al., 1991). The cool/dry climatic season (December to April) is a result of the ITCZ position being further south (~10 deg N latitude, i.e. below Central America; Ref. Fig. 1, Haug et al., 2003) and precipitation accumulation during this time is typically low (avg. < 100 mm per month; Negreros-Castillo et al., 2003), and often associated with effects of mid-latitude frontal systems (Stahle et al., 2016). This is in contrast to the wet season (May to November), where the ITCZ moves northward during the equatorial summer and the Yucatán Peninsula experiences increased precipitation (avg. 1000–1500 mm during the season; Hodell et al., 2007; Metcalfe et al., 2015).

2.4.1 HURRICANE INGRID – 2013

The synoptic history of Hurricane Manuel and Ingrid is unusual in that two hurricanes made landfall on opposite sides of Mexico within 24 h, a phenomenon not experienced since 1958 (Appendini et al., 2014). Manuel originated on September 12th 2013 from a strong low pressure

area south of Acapulco and intensified into a tropical storm that migrated northward and received category 1 hurricane status shortly after September 18th 2013, and made landfall at peak intensity on September 19th 2013 just west of Culiacán. The storm reached wind speeds near 100 km/hr (Table 2: Pasch and Zelinsky, 2014), numerous locations recorded excessive amounts of precipitation >250 mm (1110 mm recorded in Guerrero), which had a devastating economic impact exceeding $4.2 billion USD.

On the coast of the Gulf of Mexico, Ingrid originated from a tropical depression east-northeast of Veracruz, Mexico (September 12th 2013) and became a tropical storm September 13th 2013 which moved west-southwest ward before attaining category 1 hurricane status September 14th 2013 over Northeastern Mexico (Beven, 2014). The intense precipitation caused widespread flooding, (peak areas recorded excess of 500 mm of precipitation, Tuxpan, Veracruz), attaining peak wind speeds of 140 km/hr and estimated damages at $1.5 billion USD. Appendini et al. (2014) documented that the precipitation (~1000 mm) was the largest over the previous decade (1999–2013; Appendini et al., 2014). Collins et al. (2015b) documented flooding events in several cave systems in the area from Tulum to Puerto Aventuras and the effects of the hurricane on sedimentation in the Yax Chen cave system.

2.4.2 TROPICAL STORM HANNA – 2014

Tropical Storm Hanna originated (remnants of eastern Pacific Tropical Storm Trudy) as a tropical depression October 22nd 2014 over the bay of Campeche, moved eastward to east-southward toward the Yucatán Peninsula, making landfall in the proximity of the eastern/southern portion of Yucatán Peninsula and northern Belize (Cangialosi, 2014). It achieved Tropical storm status on October 27th 2014, and dissipated by Oct 30th 2014. This tropical cyclone was not well documented, but achieved 65 km winds (Cangialosi, 2014).

2.5 MATERIALS AND METHODS

2.5.1 MONITORING STATION LOCATION

Two monitoring stations were used to document WM response to seasonal and large rainfall events with all sensors (water depth and salinity) placed in the meteoric WM (Fig. 2). Sensors were attached to a plastic chain that was fixed to the cave ceiling and extended to the bottom of the cave anchored using weights that were buried into the sediment. The HOBO® conductivity (model U24-001) sensors in the Yax Chen cave system were fixed to the chains at water depths (~9 m and ~10 m) close to the halocline to show the effects of mixing between the meteoric WM and the marine WM, but also to document movement of the halocline. Yax Chen is a cave that is part of the larger Ox Bel Ha Cave system located south of Tulum (Fig. 2; also see Collins et al., 2015b,c). Two locations were used, the H2S station is located ~170 m downstream from the L-Shaped Cenote (20° 7′49.51″N, 87°28′32.08″W) and ISOD2 was < 100 m downstream from the ISOD2 Cenote (20° 7′59.56″N, 87°28′45.67″W; see Collins et al., 2015b,c for full description and map of the cave system). These two sites were selected as they were deep areas in the cave passage where the halocline was exposed. Most of the cave passage in Yax Chen is shallow (i.e.~−10 m) and only in the meteoric WM (see Collins et al., 2015b,c). The two stations are in close in proximity to each other (approx. 500 m) to determine spatial coherence of the data. At ISOD2, the conductivity sensors were fixed to the chain at −9.14 m and −10.06 m water depth, while the H2S sensors were at −9.14 m and −10.36 m. Water depth sensors (ReefNet Inc. Sensus Pro-Ultra pendant depth loggers) were also fixed to the chain in the meteoric WM at these two stations to document water level changes (Coutino et al., 2017).

2.5.2 SALINITY AND WATER LEVEL DATA

HOBO® Conductivity loggers (U24-001) measured specific conductance (µS/cm; ±0.5 µS/cm accuracy – 0 to 15,000 µS/cm conductivity range) at 30-min time intervals. Specific conductance measurements were converted to salinity (ppt) and corrected for sensor drift using the Data Assistant function in the HOBOware PRO v3.7.8 software using water samples that were retrieved every 6 months during data downloads. Water samples salinity were measured using a calibrated (in brackish range) handheld YSI (Model 30) and a Hydrolab® conductivity-temperature-depth (CTD) MS5. WM salinity was measured throughout the water column with the Hydrolab® CTD MS5. Profiles were measured by divers moving slowly down through the water column with the CTD held out from their body but also moving slightly forward and upstream to record undisturbed values. Locations were selected for a landward transect from the coast, but also based on their proximity to our monitoring sites as well as water depth so that both the meteoric and marine WMs could be measured.

Wavelet analysis was used to decompose the salinity time-series data into time-frequency space, which allowed for the determination of periodicity and temporal spacing of signals. The MATLAB wavelet package was used and see Coutino et al. (2017) for detailed description of the wavelet analysis (Torrence and Compo, 1998). The H2S −9.14 m was used for analysis as this provided the most continuous record.

ReefNet Inc. Sensus Ultra dive pendant loggers were used to collect water-level data (±1.3 cm resolution) at 30-min time intervals. The sensors were attached at fixed positions in the meteoric lens at the monitoring sites (H2S and ISOD2). Depths were corrected using barometric pressure and are shown as departures (+ and −) from mean water-level as described above.

2.5.3 CLIMATE DATA

Historical daily (March 1st 2012–July 10th 2016) weather data was obtained from Cancun International and Cozumel International airport weather stations using a web scraping technique (www.wunderground.com) and downloaded daily from Sian Ka'an Biosphere Reserve (Servicio Meteorológico Nacional, 2016) and Puerto Aventuras (See Fig. 2 for geographical reference). Malfunctioning equipment caused gaps in data and therefore the Sian Ka'an Biosphere and Puerto Aventuras were merged together to create a continuous precipitation record. This data was collected in 30 min intervals and aggregated to daily summed precipitation values (mm/day) for comparative purposes. A cumulative rainfall departure was used that determined a cumulative mean for the annual rainfall data set and then subtracting daily values to show departure variations relative to the mean (Weber and Stewart, 2004).

The wet/rainy season is typically defined as the months of May to November, whereas the dry season being the months of December to April (Carrillo-Bastos et al., 2010; Curtis et al., 1996). This criterion is based upon wet and dry periods encompassing the typical max duration. However, for our purposes, we defined wet and dry periods based on trends in our precipitation data for better comparison with groundwater response. Our wet period was defined statistically based upon the frequency of rainfall events per month (>4), a monthly mean precipitation >20 mm, for at least 2 consecutive months. Based on these conditions, the wet period for this study was defined as the months of May to December and the dry season January to April.

2.6 RESULTS AND DISCUSSION

2.6.1 PRECIPITATION

The seasonal trends of wet and dry seasons are documented in the Cancun International Airport, Cozumel International Airport, as well as the Puerto Aventuras and Sian Ka'an Biosphere Reserve weather station records (Fig. 3; May 2012–May 2016). Although there is variability in the amount of rainfall from location to location, seasonal patterns are evident in all locations (Fig. 3). Based on the calculated records of departure from mean precipitation (>0) the duration of the wet season was 8 months long and typically started in August to November, but also started earlier (i.e. May) and ended later (i.e. December) in some years compared to the norm (Table 1). The amount of precipitation during the wet season also varied in terms of the total amount delivered but also in terms of the intensity (i.e. Table 1: 2013 and 2015 wet seasons).

As discussed previously, there were several tropical storms and hurricanes from May 2012–2015 that caused intense rainfalls spanning several days and in some cases, there were multiple high rainfall events which occurred within weeks of each other. We have focused our analysis on three events Hurricane Ingrid (2013), Tropical Storm Hanna (2014) and an unnamed series of high rainfalls in 2015 (Fig. 3).

2.6.2 GROUNDWATER LEVELS

Groundwater level follows the seasonal trend in precipitation with wet seasons showing higher than mean water levels and lower levels during the dry season (Fig. 3). Monthly mean water level and precipitation show good correlations with positive relationships between rainfall and water level (Fig. 4). The mean monthly values better reflect the seasonal trend as they

account for lags in the response of water level to precipitation events, tidal fluctuations but also spatial heterogeneities in rainfall (Gondwe et al., 2010; Leyden et al., 1998). Groundwater level is a response to regional precipitation, so not all rainfall events were recorded in our weather stations but still may be having an effect on our water level data as the meteoric water moves toward the coast.

Cozumel provides the most consistent relationship with $r^2 = 0.45$ (Fig. 4). The magnitude of the variation in mean water level over wet and dry periods is fairly consistent between sites, with a maximum variation between high and low range of 30–40 cm. This consistency would be expected on a regional level, while the correlation with the individual weather stations is due to the relative change at each station, so precipitation magnitudes vary considerably (Fig. 4). Also, local to regional patterns in hydraulic conductivity may be causing the small-scale variations in water levels between sites as well as spatial variability of precipitation. It should be noted that some of the water level change during hurricanes may be due to storm tides, although during Hurricane Ingrid (2013) and Tropical Storm Hanna (2014), there was little storm surge damage reported on the coast. Groundwater level during these events rapidly increased and then gradually decreased (days to weeks) indicating most of the effect was from rainfall.

2.6.3 METEORIC WM SALINITY

2.6.3.1 METEORIC WM CHARACTERISTICS

WM characteristics follow previously documented trends with sites closer to the coast having a shallower halocline vs those further inland where the halocline is deeper (Fig. 6; Beddows, 2004). Based on our measured profiles, the halocline gets deeper by approx. 1.6 m/km moving inland and is comparable to ~2.0 m/km previous studies (Figs. 5 and 6; Smart et al.,

2006). The salinity of the meteoric WM also increases moving towards the coast, with inland areas having a salinity of ~1 ppt and coastal areas ranging from 3.5 to 6 ppt. The structure of the WMs also varies with some areas having a stepped meteoric WM with two haloclines (i.e. Yax Chen Arizona and Little Chen; Fig. 5) or a more gradual transition to the marine WM. Areas further inland generally have sharp halocline transitions while coastal areas tend to be more variable (i.e. Yax Chen and Ponderosa; Fig. 5). Intermediate and/or small steps in the halocline likely represent a mixing zone which can be thicker closer to the coast (Beddows, 2004).

The Hydrolab® CTD profiles are useful for documenting regional WM characteristics, but they are temporal measurements that do not provide long-term information on how the WMs respond to seasonal variation and storm perturbations. Hydrolab® CTD profiles recorded at the two monitoring sites in Yax Chen (H2S and ISOD2) show that over approximately 2 years the WM structure is relatively stable, but as documented in December 2011 the first salinity transition (7.78 to 16.01 ppt for H2S and 6.91 to 16.88 ppt for ISOD2) is slightly deeper (−0.3 m) than in 2012 and 2013 (Fig. 7). The salinity of the upper WMs also varies slightly (6–7 ppt) between time periods, but during the same time period the ISOD2 and H2S salinities are similar. This indicates that at least on a local level the WM characteristics are consistent as the ISOD2 monitoring site is approx. 500 m further upstream (landward) than the H2S monitoring site. Continuous monitoring salinity over seasonal cycles combined with Hydrolab® CTD measurements is advantageous as we can better document seasonal trends and forcing mechanisms.

2.6.3.2 YAX CHEN SALINITY TRENDS

Spanning four years of data, there are seasonal trends in salinity that correspond with relatively wet and dry periods as defined by our precipitation and groundwater level data. Two sensors were placed at common depths in both the H2S (−9.14 and −10.36 m) and ISOD2 monitoring sites (−9.14, −10.06 m) with the lowest-most sensor placed close to the first halocline in the meteoric WM (Fig. 7). The salinity trends with the lowermost sensors show the movement of the halocline with wet and dry periods (Fig. 3). The H2S sensor which is slightly closer (at −10.36 m) to the halocline shows the sensor going out of range (salinity >9 ppt, i.e. from 15/04/2013 to 01/06/2013) or fluctuating to high and low salinities over short time periods (6 ppt to >9 ppt; i.e. from 05/12/2012 to 25/12/2012; Fig. 3). During wet periods, salinities are generally in the 6–7 ppt range but rapidly rise >7 ppt for days or weeks in duration with rainfall events increased meteoric WM height (i.e. from 15/09/2013 to 25/09/2013, Fig. 3). This response is also documented in the -10.06 m ISOD2 sensor which is shallower and slightly further away from the halocline but the record is dominated by rapidly fluctuating salinity (6 ppt to >9 ppt; i.e. from 10/05/2012 to 20/05/2012). This salinity response with dry periods and lower groundwater height reflects a shallowing of the halocline due to reduced precipitation (approx. <20–30 cm). It is pronounced from 08/2012 to 07/2013 during a very dry period and rainfall totals were low during the wet season (from 05/2012 to 12/2012; Fig. 3). The rapid fluctuations of salinity (6 ppt to > 9 ppt) during dry periods are caused by smaller rainfall or tidal fluctuations causing turbulent mixing with meteoric WM or tidal pumping (esp. the −10.36 m sensor at ISOD2; Coutino et al., 2017). Tidal variations in the water depth sensor shows average tidal variations of approx. 0.05–0.07 m indicating deeper sensors (−10.06 and −10.36 m) are more sensitive to tides with the shallower halocline (lower groundwater height) during the dry period (Coutino et al.,

2017). During wet periods when groundwater height is greater, the halocline is deeper and the increases in salinity are likely responding to increased discharge and turbulent mixing with the marine WM (Fig. 3).

The shallower sensors (−9.1 m) show similar response with smaller changes in salinity (approx. 6.5 to 7.25 ppt) over wet and dry periods associated with halocline movement, but the precipitation events are proportionally more dominant in the record, with salinity changing by 1–3 ppt over short time intervals (i.e. days to weeks; i.e. 15/09/2013 to 25/09/2013; Fig. 3).

Cross-plots of daily salinity and water depth show this relationship with wet and dry periods (Fig. 8). There is a minimum salinity threshold for a given water depth and this threshold line has an inverse relationship which represents the seasonal change in halocline depth and the mixing events that occurred in upstream locations. The salinity change associated with this threshold line (trendline, denoting salinity (ppt); Fig. 8) is small at ~1 ppt and consistent between the sensors regardless of depth or location (−9.14 to −10.36 m; Fig. 8). Increases in salinity from this minima threshold (represented by directional arrow; Fig. 8) are due to events associated with rainfall and/or tidal pumping (esp. −10.36 at H2S). The salinity increases (>2–3 ppt) are proportionally higher than the seasonal fluctuations.

Data using the monthly mean and standard deviation of salinity and water depth separate this relationship and show seasonal trends minimizing the effects of tides and lags in the data (Fig. 9). The monthly mean salinity and water level shows a negative trend due to seasonal movement of the halocline as described, while the standard deviation is the degree of change in water level and salinity due to short term rainfall events which shows a positive trend. The relationship is best displayed in the −9.14 m data at both the H2S and ISOD2 stations, while the

deeper sensors (−10.36 and −10.06 m) less so, likely because the sensor is too close to the halocline and the sensor goes out of range for extended periods of time.

2.6.3.3 LARGE-SCALE RAINFALL EVENTS

Three large scale rainfall events were selected for detailed comparisons and include Hurricane Ingrid (2013), Tropical Storm Hanna (2014) and a series of unnamed events in 2015 (Fig. 10). These three events are scaled in terms of precipitation and duration and as will be discussed, there is a proportional response in salinity of the meteoric WM.

Hurricane Ingrid and its confluence with Manuel had large impact on the Yucatán in terms of the magnitude of the rainfall with flooding occurring in many areas (see Collins et al., 2015b for a full description). It was also notable in-terms of the number of high rainfalls that occurred in weeks prior to Ingrid but also the amount of rainfall received in one day (339.2 mm from PTO and SK on 18/09/2013). This combination of events caused sustained water level rise in Yax Chen over a long period of time (approx. 2.5 weeks). Drainage toward the coast caused increased flow velocity and mixing with the marine WM resulting in elevated meteoric WM salinities, (>9 ppt) as recorded in both the H2S and ISOD2 sensors. The increased salinity was sustained over approximately one week and then began to gradually decrease in weeks after the hurricane. The owners of Cenote Nohoch Nah Chich located south of Puerto Aventuras reported that the cenote water was undrinkable due to elevated salinity for days after the hurricane showing that the effect reached surface waters (Collins et al., 2015b). Vera et al. (2012) also showed increases in groundwater salinity associated with Hurricane Ike (2008) in the Northern Yucatán Peninsula (Dzilam Bravo) demonstrating the phenomena is likely widespread throughout the aquifer.

Tropical Storm Hanna was lesser in extent in terms of total rainfall (96 mm from PTO and SK between 21/10/2014 to 22/10/2014) but also there were fewer precipitation events prior to the storm, resulting in the water table being at a lower height compared to Ingrid. Unfortunately, we had only one salinity sensor operational in Yax Chen at this time (H2S −9.14 m), but it shows a similar response as that of Ingrid (>9 ppt) but decreases faster to background levels (<1 week).

For the unnamed smaller rainfall events in 2015 (45.2 mm sum from PTO and SK between 01/11/2015 to 30/12/2015), the salinity response is different than Tropical Storm Hanna. In Yax Chen, the sensors close to the halocline are responding in a predictable way and comparable to Ingrid and Hanna, but the salinity increase is smaller (approx. 1 ppt).

2.6.3.4 PERIODICITY OF THE SALINITY DATA

Wavelet analysis of the salinity record from H2S -9.14 m shows the seasonal mixing effects with periodicities at approximately 6 months (approx. 190 days) but also tidal mixing at 1-day and 0.5-day timescales (Fig. 11). The 1-day and 0.5-day periodicities are consistent with the coast having a predominant mixed, semi-diurnal tidal period (Kjerfve, 1981). During rising tide, flow inland in the marine WM would cause increased turbulent mixing with the meteoric WM which is flowing coastward. During falling tide, flow in the marine WM would be coastward and thus would cause less mixing. This change in salinity over tidal cycles would be more pronounced during wet periods with higher flows in the meteoric WM. This seasonal cycle (wet and dry) matches the 6 month periodicity in the wavelet analysis. During the September 2013 hurricane, the tidal effect was suppressed as it was likely overwhelmed by the high rainfall and flow in the meteoric WM but also perhaps by some storm surge. To speculate longer-term

periodic phenomena within a wavelet analysis such as El Niño (2 to 7 years; Cabrera et al., 2010), a much longer continuous record would be needed than the one present within this study (~2 years).

2.7 CONCLUSIONS

Aquifer salinity responds to the scale and frequency of rainfall events with larger storms causing more turbulent mixing between the meteoric and marine WMs. Based on our 4-year record of water level, salinity and precipitation, meteoric WM salinity is strongly influenced by precipitation and mixing with the marine WM. Meteoric WM salinity varies over wet and dry seasons with the movement of the halocline, but also on a short-term basis through large rainfall events. To establish spatiotemporal trends, both geographically (especially distance from the coast) and with depth, further study is needed to understand the complexity of the relationship. However, it would be expected that under wetter conditions with more frequent hurricanes, the net salinity of meteoric water would increase, and correspondingly, during drier intervals with fewer hurricanes, the meteoric water would be expected to be less saline. So although the meteoric WM may be thicker during wet periods, hurricane and large storm events could increase salinity, making the water non-potable and unsuitable for irrigation. Conversely, during dry periods, the meteoric WM would be thinner but perhaps less saline due to less turbulent flow regimes, if there were fewer large rainfall events. There are spatial precipitation patterns that are no doubt playing a role, and there may be regional differences in hydrology that remain unknown due to the lack of data, however, if predictions of increased hurricane activity hold true (Sobel et al., 2016), groundwater will become increasingly saline. More monitoring and modeling is needed to fully understand the range of effects (i.e. Coutino et al., 2017), but as demonstrated in

this study, the effect of intense rainfall on groundwater potability is important for both forecasting, but also hindcasting with paleoenvironmental records (van Hengstum et al., 2010).

2.8 ACKNOWLEDGEMENTS

The authors would like to thank the anonymous reviewers for their insightful, helpful and constructive comments that greatly improved a previous version of the manuscript. The Mexico Cave Exploration Project (MCEP) and Cindaq provided logistical support in Mexico, and we thank all dive volunteers who helped in the field. Special thanks to Zero-Gravity Mexico (F. Devos and C. Le Maillot) and staff for dive logistics/support. Hydrolab® CTD profiles from Cenote Angelita and The Pit were provided by Patricia Beddows and Simon Richards. This research was supported through a Natural Sciences and Engineering Research Council (NSERC) Discovery Grant to EGR and an NSERC Post-Graduate Scholarship award to SEK.

2.9 REFERENCES

Alcocer J., Lugo A., Marín L.E. and Escobar E., Hydrochemistry of waters from five cenotes and evaluation of their suitability for drinking-water supplies, northeastern Yucatán, Mexico, *Hydrogeol. J.* **6**, 1998, 293–301, http://dx.doi.org/10.1007/s100400050152.

Appendini, C.M., Rafael Meza, P., Pedrozo-Acuña, A., Raga, G.B., Farfán, L.M., 2014. Storm Surge Estimation Due to the Incidence of Simultaneous Tropical Cyclones in Mexico, In: Proceedings 31st Conference on Hurricane and Tropical Meteorology. American Meteorological Society, San Diego.

Back W. and Hanshaw B.B., Comparison of chemical hydrogeology of the carbonate peninsulas of Florida and Yucatán, *J. Hydrol.* **10**, 1970, 330–368, http://dx.doi.org/10.1016/0022-1694(70)90222-2.

Bauer-Gottwein P., Gondwe B.R.N., Charvet G., Marin L.E., Rebolledo-Vieyra M. and Merediz-Alonso G., Review. The Yucatán Peninsula karst aquifer, Mexico, *Hydrogeol. J.* **19**, 2011, 507–524, http://dx.doi.org/10.1007/s10040-010-0699-5.

Beddows P.A., Groundwater Hydrology of a Coastal Conduit Carbonate Aquifer : Caribbean Coast of the Yucatán Peninsula, 2004, University of Bristol; México.

Beddows P.A., Smart P.L., Whitaker F.F. and Smith S.L., Decoupled fresh-saline groundwater circulation of a coastal carbonate aquifer: spatial patterns of temperature and specific electrical conductivity, *J. Hydrol.* **346**, 2007, 18–32, http://dx.doi.org/10.1016/j.jhydrol.2007.08.013.

Beven, J.L., 2014. Hurricane Ingrid, National Hurricane Centre Tropical Cyclone Report.

Cabrera J.L.B., Romero E.A., Such V.Z., Garcia C.G. and Porrua F.E., Significance tests for the relationship between "El Nino" phenomenon and precipitation in Mexico, *Geofisica Int.* **49**, 2010, 245–261.

Cangialosi, J.P., 2014. Tropical Storm Hanna, National Hurricane Centre Tropical Cyclone Report.

Carrillo-Bastos A., Islebe G.A., Torrescano-Valle N. and González N.E., Holocene vegetation and climate history of central Quintana Roo, Yucatán Península, Mexico, *Rev. Palaeobot. Palynol.* **160**, 2010, 189–196, http://dx.doi.org/10.1016/j.revpalbo.2010.02.013

Coke J., Sea-level curve, *Nature,* **353**, 1991, 25 – 25, http://dx.doi.org/10.1038/353025a0

Collins S.V., Reinhardt E.G., Werner C.L., Le Maillot C., Devos F. and Meacham S.S., Regional response of the coastal aquifer to Hurricane Ingrid and sedimentation flux in the Yax Chen cave system (Ox Bel Ha) Yucatán, Mexico, *Palaeogeogr. Palaeoclimatol. Palaeoecol.* **438**, 2015b, 226–238, http://dx.doi.org/10.1016/j.palaeo.2015.07.030.

Collins S.V., Reinhardt E.G., Werner C.L., Le Maillot C., Devos F. and Rissolo D., Late Holocene mangrove development and onset of sedimentation in the Yax Chen cave system (Ox Bel Ha) Yucatán, Mexico: Implications for using cave sediments as a sea-level indicator, *Palaeogeogr. Palaeoclimatol. Palaeoecol.* **438**, 2015c, 124–134, http://dx.doi.org/10.1016/j.palaeo.2015.07.042

Coutino, A., Stastna, M., Kovacs, S., Reinhardt, E., Variations in salinity of the meteoric lens in cave networks on the Yucatán. *J. Hydrol*. **551**, 2017, 715 – 729.

doi:10.1016/j.jhydrol.2017.04.022

Curtis J.H., Hodelle D.A. and Brenner M., Climate Variability on the Yucatán Peninsula (Mexico) during the Past 3500 Years, and Implications for Maya Cultural Evolution, *Quat. Res.* **47**, 1996, 37–47, http://dx.doi.org/10.1006/qres.1996.0042.

Delgado C., Pacheco J., Cabrera A., Batllori E., Orellana R. and Bautista F., Quality of groundwater for irrigation in tropical karst environment: the case of Yucatán, Mexico, *Agric. Water Manage.* **97**, 2010, 1423–1433, http://dx.doi.org/10.1016/j.agwat.2010.04.006.

Escolero O.A., Marin L.E., Steinich B., Pacheco A.J., Cabrera S.A. and Alcocer J., Development of a protection strategy of karst limestone aquifers: the Merida Yucatán, Mexico case study, *Water Resour. Manage.* **16**, 2002, 351–367, http://dx.doi.org/10.1023/A:1021967909293

Ford, D., and Williams, P.D., Karst hydrogeology and geomorphology, second ed. John Wiley & Sons, Sussex, England, 2013.

Gondwe B.R.N., Lerer S., Stisen S., Marín L., Rebolledo-Vieyra M., Merediz-Alonso G. and Bauer-Gottwein P., Hydrogeology of the south-eastern Yucatán Peninsula: New insights from water level measurements, geochemistry, geophysics and remote sensing, *J. Hydrol.* **389**, 2010, 1–17, http://dx.doi.org/10.1016/j.jhydrol.2010.04.044.

Hastenrath S., Climate Dynamics of the Tropics, 8th ed, 2012, Springer Science & Business Media.

Hastenrath S. and Greischar L., Circulation mechanisms related to northeast Brazil rainfall anomalies, *J. Geophys. Res.* **98**, 1993, 5093, http://dx.doi.org/10.1029/92JD02646.

Haug G.H., Gunther D., Peterson L.C., Sigman D.M., Hughen K.A. and Aeschlimann B., Climate and the collapse of maya civilization, *Science* **299** (80-), 2003, 1731–1735, http://dx.doi.org/10.2307/482941.

Hodell D.A., Brenner M. and Curtis J.H., Climate and cultural history of the Northeastern Yucatán Peninsula, Quintana Roo, Mexico, *Clim. Change* **83**, 2007, 215–240, http://dx.doi.org/10.1007/s10584-006-9177-4.

Hughen K.A., Overpeck J.T., Peterson L.C. and Anderson R.F., The nature of varved sedimentation in the Cariaco Basin, Venezuela, and its palaeoclimatic significance, *Geol. Soc. London Spec. Publ.* **116**, 1996, 171–183, http://dx.doi.org/10.1144/GSL.SP.1996.116.01.15

Kambesis, P.N., and Coke, J.G., Overview of the controls on eogenetic cave and karst development in Quintana Roo, Mexico, Coastal Karst Landforms, Springer Netherlands, 2013, 347-373.

Kjerfve, B., 1981. Tides of the Caribbean Sea. *J. Geophys. Res. Ocean*. 86, 4243–4247. doi:10.1029/JC086iC05p04243

Kottek M., Grieser J., Beck C., Rudolf B. and Rubel F., World map of the Köppen-Geiger climate classification updated, *Meteorol. Zeitschrift* **15**, 2006, 259–263, http://dx.doi.org/10.1127/0941-2948/2006/0130

Leyden B.W., Brenner M.H. and Dahlin B., Cultural and Climatic History of Coba, a Lowland Maya City in Quintana Roo, Mexico, *Quat. Res.* **49**, 1998, 111–122, http://dx.doi.org/10.1006/qres.1997.1941.

Manuel-Navarrete D., Pelling M. and Redclift M., Critical adaptation to hurricanes in the Mexican Caribbean: development visions, governance structures, and coping strategies, *Glob. Environ. Change* **21**, 2011, 249–258,

http://dx.doi.org/10.1016/j.gloenvcha.2010.09.009.
Marin L.E. and Perry E.C., The Hydrogeology and Contamination Potential of Northwestern Yucatán, 1994, Geofis. Int; Mexico, doi:10.1016/0148-9062(95)92312-6.
Metcalfe C.D., Beddows P.A., Bouchot G.G., Metcalfe T.L., Li H. and Van Lavieren H., Contaminants in the coastal karst aquifer system along the Caribbean coast of the Yucatán Peninsula, Mexico, *Environ. Pollut.* **159**, 2011, 991–997, http://dx.doi.org/10.1016/j.envpol.2010.11.031.
Metcalfe S.E., Barron J.A. and Davies S.J., The Holocene history of the North American Monsoon: "known knowns" and "known unknowns" in understanding its spatial and temporal complexity, *Quat. Sci. Rev.* **120**, 2015, 1–27, http://dx.doi.org/10.1016/j.quascirev.2015.04.004.
Metcalfe S.E., O'Hara S.L., Caballero M. and Davies S.J., Records of late pleistocene-holocene climatic change in Mexico – a review, *Quat. Sci. Rev.* **19**, 2000, 699–721, http://dx.doi.org/10.1016/S0277-3791(99)00022-0.
Moore Y.H., Stoessell R.K. and Easley D.H., Fresh-Water/Sea-Water Relationship Within a Ground-Water Flow System, Northeastern Coast of the Yucatán Peninsula, *Ground Water* **30**, 1992, 343–350
Municipalidad de Solidaridad., 2005. Programa director de desarrollo urbano del centro de población Tulum. 2002-2026. Actualizacion Marzo de 2005. www.solidaridad.gob.mx.
Negreros-Castillo P., Snook L.K.and Mize C.W., Regenerating mahogany (Swietenia macrophylla) from seed in Quintana Roo, Mexico: the effects of sowing method and clearing treatment, *For. Ecol. Manage.* **183**, 2003, 351–362, http://dx.doi.org/10.1016/S0378-1127(03)00143-9
Pacheco J., Martin L., Cabrera A., Steinich B. and Escolero O., Nitrate temporal and spatial patterns in 12 water-supply wells, Yucatán, Mexico, *Environ. Geol.* **40**, 2001, 708–715, http://dx.doi.org/10.1007/s002540000180.
Pasch, R.J., Zelinsky, D., 2014. Hurricane Manuel, National Hurricane Centre Tropical Cyclone Report.
Perry, E., Swift, J., Gamboa, J., Reeve, A., Sanborn, R., Marin, L., Villasuso, M., Geologic and environmental aspects of surface cementation, north coast, Yucatán, Mexico, *Geology, **17**, 1989,* 818–821, http://dx.doi.org/10.1130/0091-7613(1989) 017<0818:GAEAOS> 2.3.CO;2
Perry, E., Velazquez-Oliman, G., Socki, R.A., 2003. Hydrogeology of the Yucatán Peninsula. Lowl. Maya three Millenn. Human–wild. *Interface*, 115–138.
Peterson L.C., Overpeck J.T., Kipp N.G. and Imbrie J., A high-resolution Late Quaternary upwelling record from the anoxic Cariaco Basin, Venezuela, *Paleoceanography* **6**, 1991, 99–119, http://dx.doi.org/10.1029/90PA02497.
Servicio Meteorológico Nacional, Daily Weather Data, 2016, Servicio Meteorológico Nacional; Tulum Mexico.
Smart P.L., Beddows P.A., Coke J., Doerr S. and Whitaker F.F., *Cave Development on the Caribbean coast of the 2404* 2006, 105–128, http://dx.doi.org/10.1130/2006.2404(10)
Sobel A.H., Camargo S.J., Hall T.M., Lee C.-Y., Tippett M.K. and Wing A.A., Human influence on tropical cyclone intensity, *Science* **353** (80-), 2016, 242–246, http://dx.doi.org/10.1126/science.aaf6574.
Stahle D.W., Cook E.R., Burnette D.J., Villanueva J., Cerano J., Burns J.N., Griffin D., Cook B.I., Acuna R., Torbenson M.C.A., Sjezner P. and Howard I.M., The Mexican Drought

Atlas: Tree-ring reconstructions of the soil moisture balance during the late pre-Hispanic, colonial, and modern eras, *Quat. Sci. Rev.* **149**, 2016, 34–60, http://dx.doi.org/10.1016/j.quascirev.2016.06.018.

Stoessell R.K., Dampening of Transverse Dispersion in the Halocline in Karst Limestone in the Northeastern Yucatán Peninsula, *Groundwater* 1995, http://dx.doi.org/10.1111/j.1745-6584.1995.tb00291.x.

Stoessell R.K. and Coke J.G., An Explanation for the Lack of a Dilute Freshwater Lens in Unconfined Tropical Coastal Aquifers: Yucatán Example, *Gulf Coast Assoc. Geol. Soc. Trans.* **56**, 2006, 785–792.

Torrence C. and Compo G.P., A Practical Guide to Wavelet Analysis, *Bull. Am. Meteorol. Soc.* **79**, 1998, 61–78.

van Hengstum P.J., Donnelly J.P., Fall P.L., Toomey M.R., Albury N.A. and Kakuk B., The intertropical convergence zone modulates intense hurricane strikes on the western North Atlantic margin, *Sci. Rep.* **6**, 2016, 21728, http://dx.doi.org/10.1038/srep21728.

van Hengstum P.J., Donnelly J.P., Toomey M.R., Albury N.A., Lane P. and Kakuk B., Heightened hurricane activity on the Little Bahama Bank from 1350 to 1650 AD, *Cont. Shelf Res.* **86**, 2013, 103–115, http://dx.doi.org/10.1016/j.csr.2013.04.032.

van Hengstum P.J., Reinhardt E.G., Beddows P.A. and Gabriel J.J., Linkages between Holocene paleoclimate and paleohydrogeology preserved in a Yucatán underwater cave, *Quat. Sci. Rev.* **29**, 2010, 2788–2798, http://dx.doi.org/10.1016/j.quascirev.2010.06.034

Vera, I., Mario-Tapia, I., Enriquez, C., 2012. Effects of drought and subtidal sea-level variability on salt intrusion in a coastal karst aquifer. *Mar. Freshw. Res*. **63**, 485–493. doi:10.1071/MF11270

Vesper D.J., Loop C.M. and White W.B., Contaminant transport in karst aquifers, *Theor. Appl. Karstol.* **13–14**, 2001, 101–111, http://dx.doi.org/10.1016/0148-9062(96)83847-2.

Ward W.C., Weidie A.E. and Back W., Geology and Hydrogeology of the Yucatán and Quarternary Geology of Northeastern Yucatán Peninsula, *New Orleans Geol. Soc.* 1985, 1–160.

Weber K. and Stewart M., A critical analysis of the cumulative rainfall departure concept, *Ground Water* **42**, 2004, 935–938, http://dx.doi.org/10.1111/j.1745-6584.2004.t01-11-.x.

Werner, C., 2007. Double-Diffusive Fingering in Porous Media. Florida State University.

Whitaker F.F. and Smart P.L., Active circulation of saline ground waters in carbonate platforms: Evidence from the Great Bahama Bank, *Geology* **18**, 1990, 200–203, doi:10.1130/0091-7613(1990)018<0200:ACOSGW>2.3.CO;2.

2.10 TABLES

Table 1 – Summary statistics of precipitation data. Columns are as follows: Total precipitation represents the collective sum from Cancun, Cozumel, and Sian Ka'an and Puerto Aventuras weather stations, standard deviation (St.D.) as well as max daily sum precipitation (mm) from the recording weather stations.

	Year	Total Precip. (mm)	St.D. (mm)	Max Daily Precip. (mm)
Wet Season	2012	7504.44	1819.96	443.23
Dry Season	2013	766.98	230.05	142.24
Wet Season	2013	8935.17	2502.11	370.84
Dry Season	2014	1046.52	398.88	229.87
Wet Season	2014	5007.25	2238.67	369.57
Dry Season	2015	543.68	281.03	187.96
Wet Season	2015	7484.70	3392.71	464.82
Dry Season	2016	1748.31	836.64	408.94
Wet Season*	2016	149.68	66.06	125.73

Notes:
Wet Season – May to December
Dry Season – January to April
*May only

2.11 FIGURES

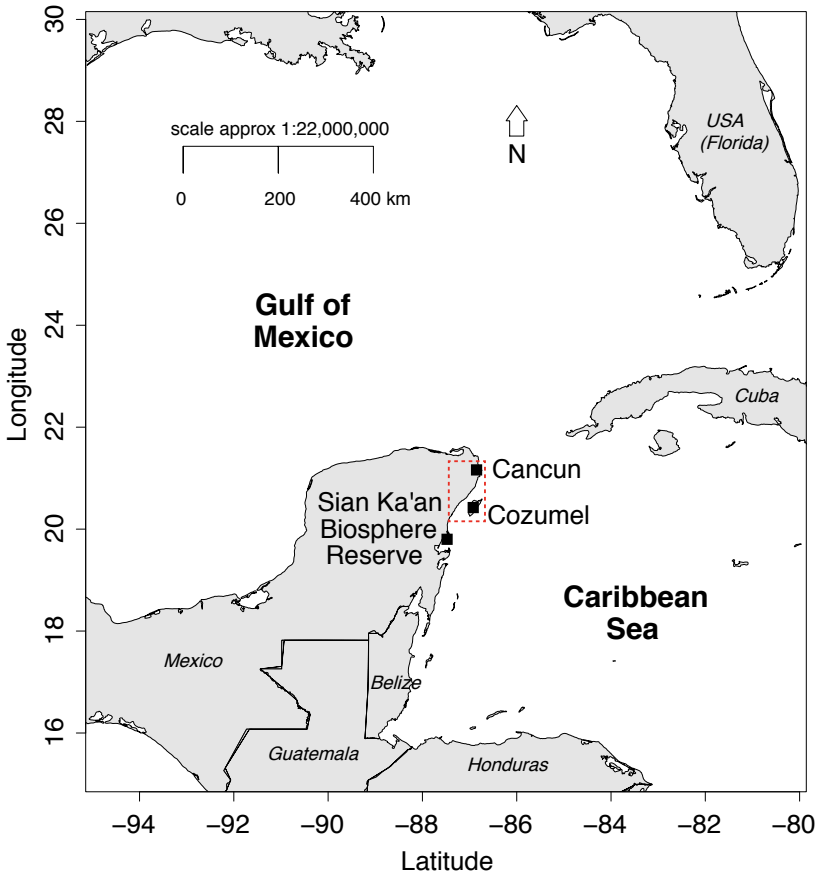

Fig. 1 – Study area along the Caribbean Coast of the Yucatán Peninsula, Mexico. Filled black squares denote the position of the weather stations and the red hatched location demarks the study area.

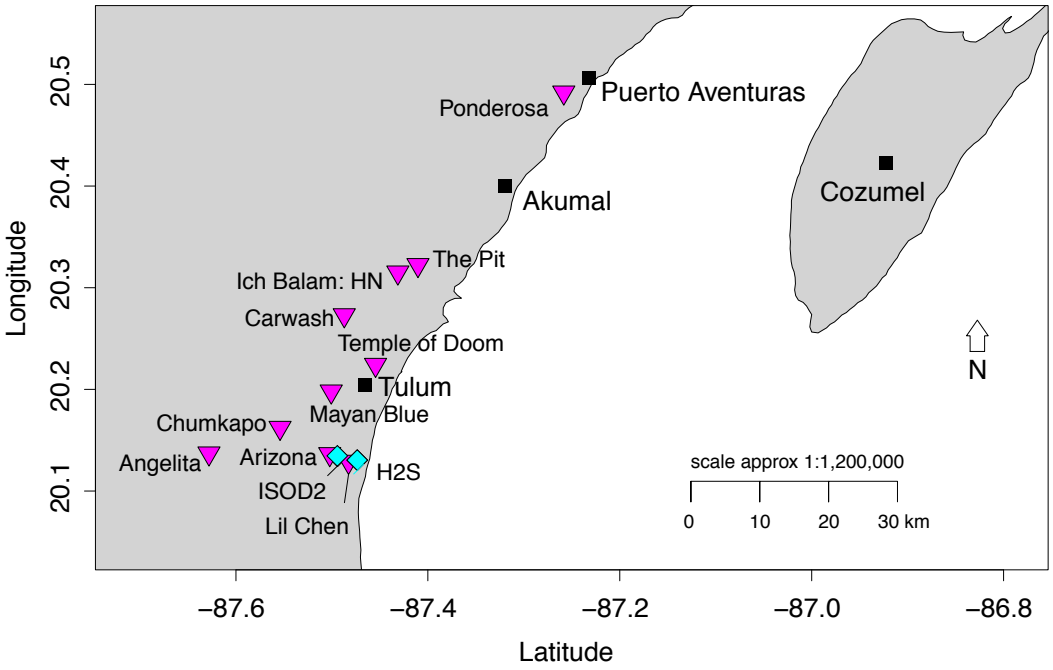

Fig. 2 – Location of monitoring sites used in this study.

Fig. 3 – Time series plots from May 2012 to 2016 (GMT) for: 1) precipitation (mm) from Cancun, Cozumel and Sian Ka'an and Puerto Aventuras weather stations; 2) Yax Chen groundwater level (m) and salinity (ppt) from the two monitoring sites (H2S, −9.14 and −10.36 m depth; ISOD 2, −9.14 and −10.06 m depth). Precipitation and water level are plotted as departure from the mean over the analysis period while salinity (ppt) is plotted as 30-min time intervals. Monthly trends are also plotted which are monthly mean departure values. Gaps in the records are due to sensor malfunction and battery depletion, and flat-lined data (salinity) is due the sensor going out of range (>9 ppt). Hurricanes (orange) and tropical storms (blue) are highlighted over the analysis period.

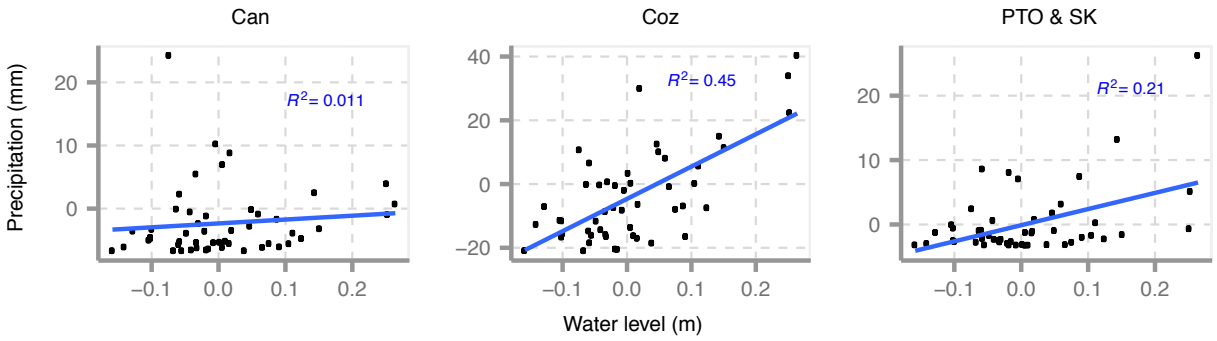

Fig. 4 – Cross-plots showing the relationship between the mean monthly precipitation (mm) and water level (m) from the weather stations and monitoring sites. Mean values best represent seasonal changes over the analysis period.

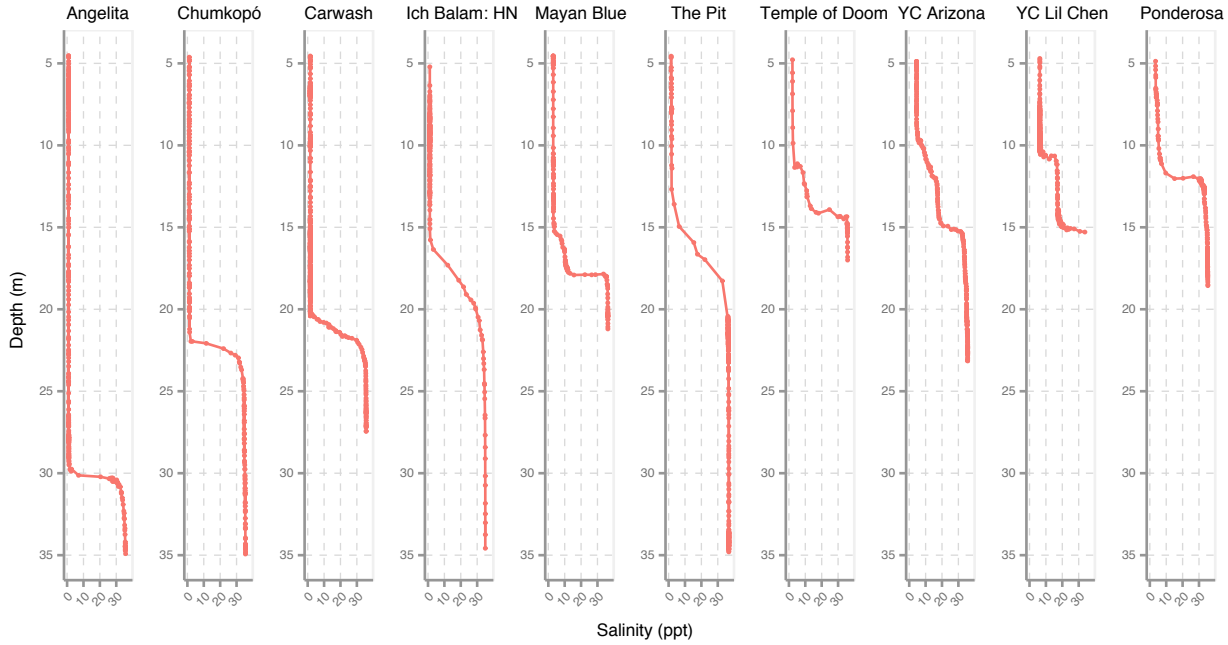

Fig. 5 – Hydrolab® CTD (MS5) profiles of salinity (ppt) from various cenotes and caves in the area. Profiles measured over the analysis period showing the depth of the halocline moving towards the coast (Angelita to Ponderosa). Arizona and Lil Chen are in the Yax Chen cave system and close to our two monitoring stations (H2S and ISOD2).

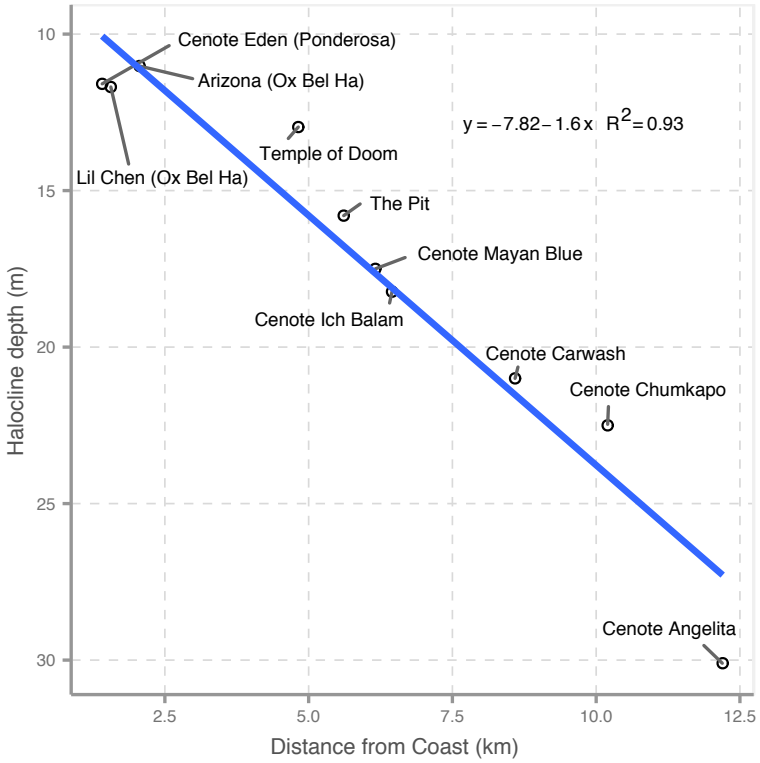

Fig. 6 – Cross-plot showing the halocline depth (m) relationship with distance from the coast (km) which increases by −1.6 m/km.

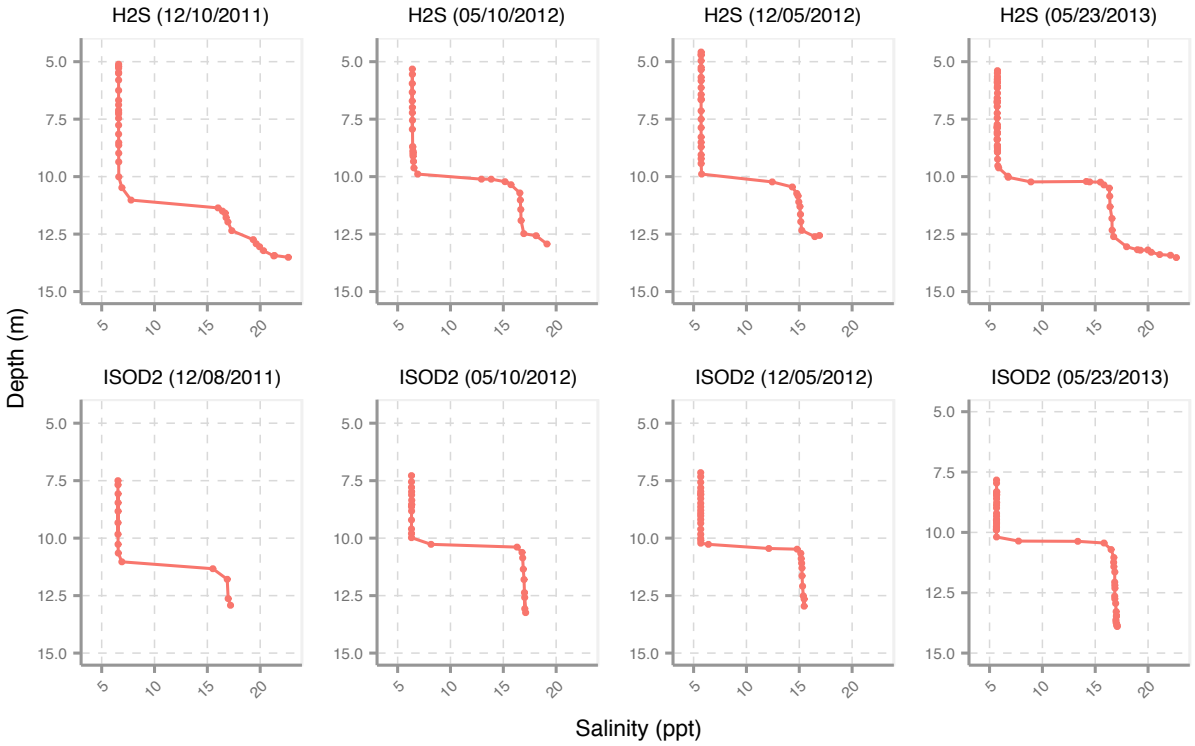

Fig. 7 – Hydrolab® CTD (MS5) profiles of salinity (ppt) with depth (m) along the sensor chain for monitoring sites (H2S and ISOD2) in Yax Chen over various time periods.

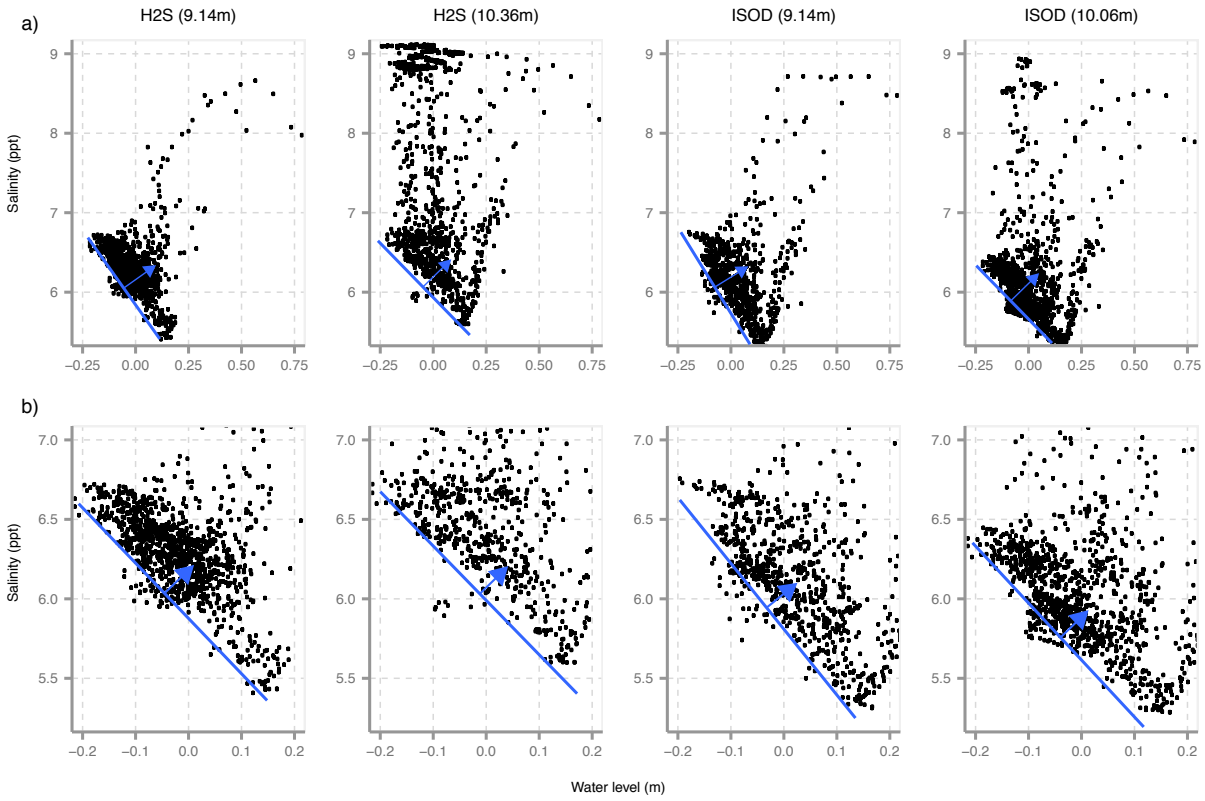

Fig. 8 – a) Cross-plots between daily meteoric WM salinity (ppt) and departure from mean water depth (m) from H2S and ISOD2. Slope of lower threshold line represents seasonal change in salinity with wet and dry periods, and higher salinity departures from this threshold (arrow) represent mixing during precipitation events. b) Data with outlying values removed.

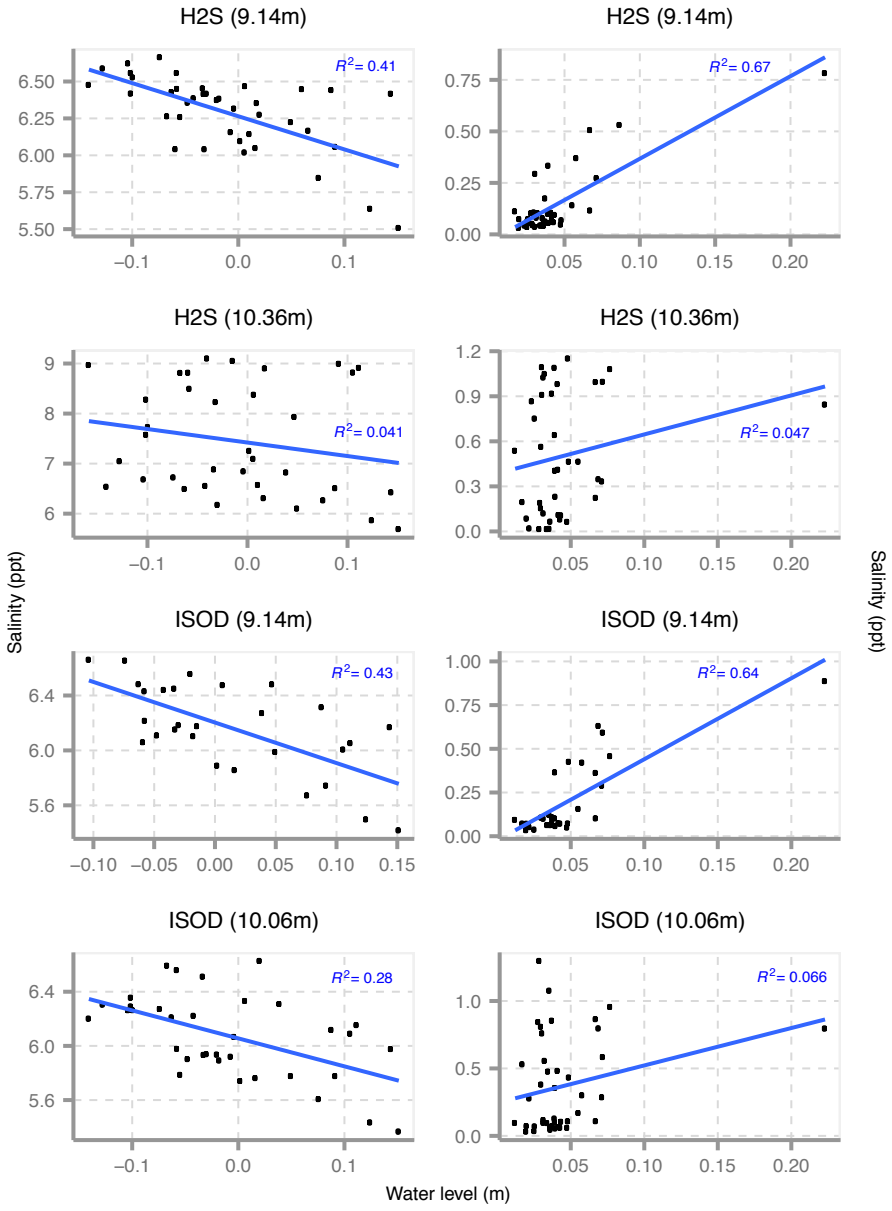

Fig. 9 – Cross-plots between monthly mean salinity (ppt) and water depth (m) as well as cross plots between monthly standard deviation of these two parameters. Negative relationships with the mean represents the seasonal mixing, while the positive relationship with standard deviation represents the effects of rapidly changing water level (precipitation events) on salinity and mixing.

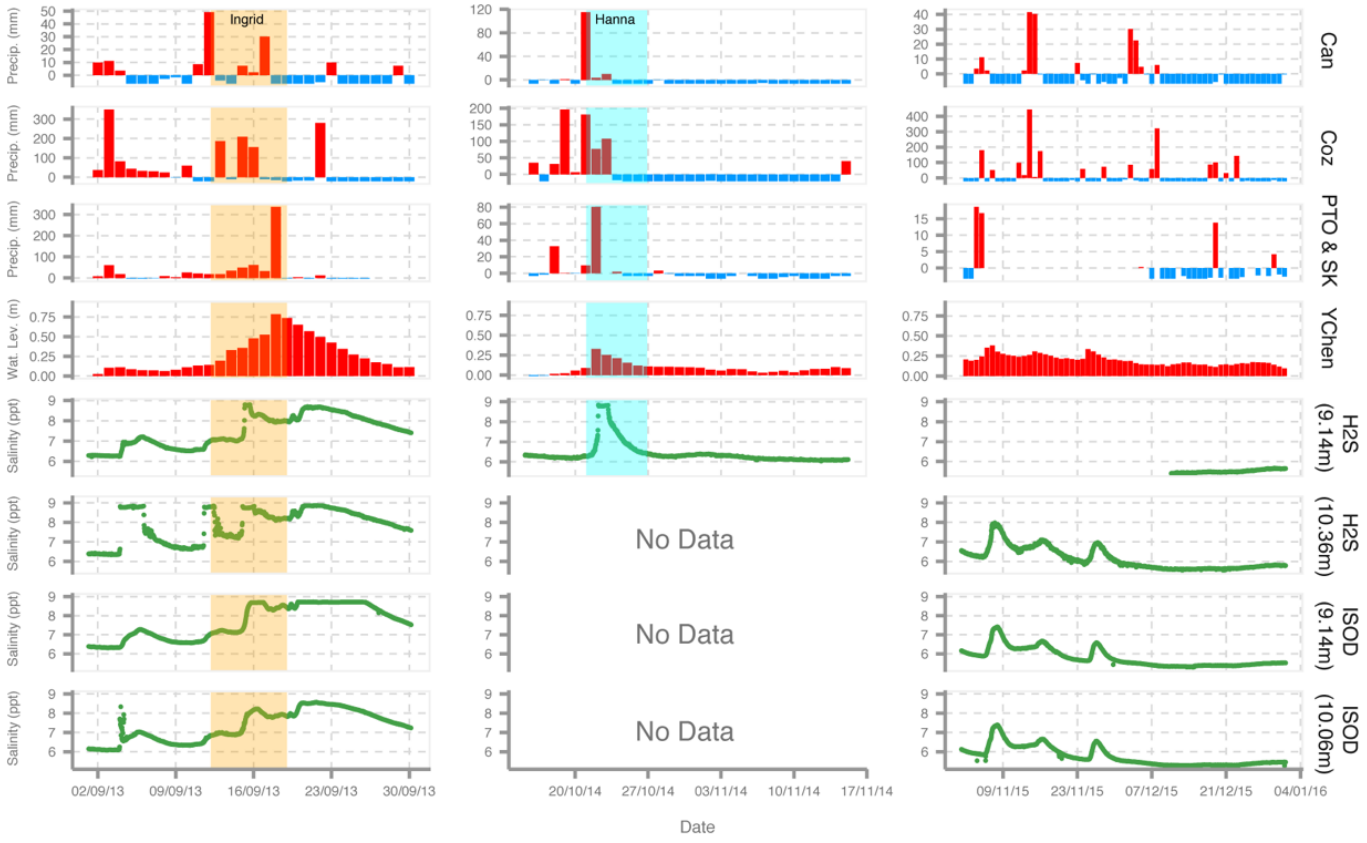

Fig. 10 – Detailed time-series plots (GMT) spanning three rainfall events: Hurricane Ingrid in 2013, Tropical Storm Hanna, 2014, and an un-named series of events in 2015. Plots use the same parameters as described in Fig. 3.

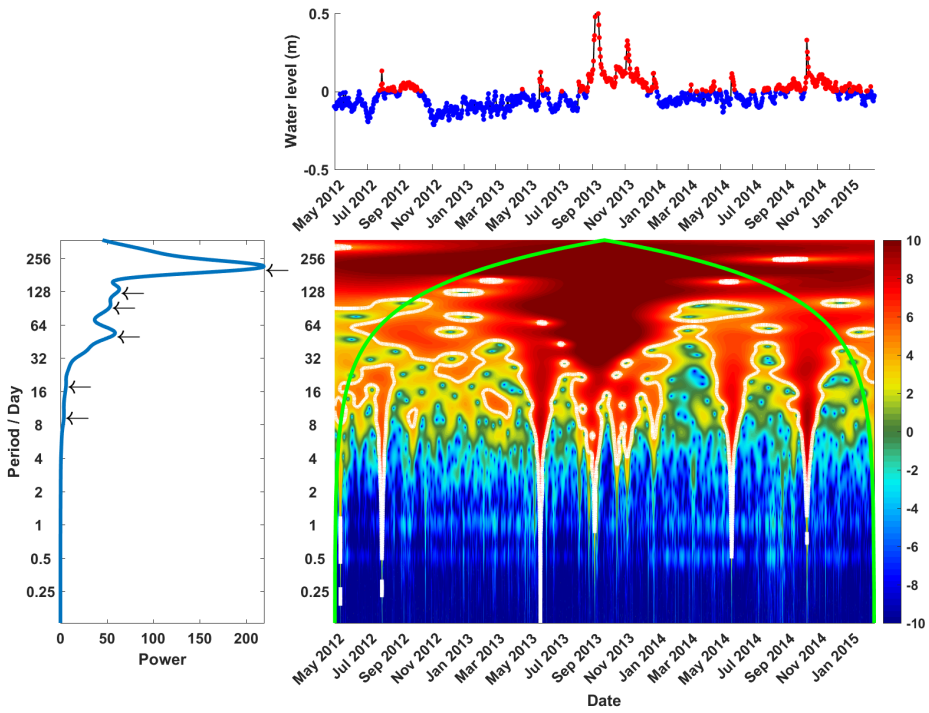

Fig. 11 – The departure from mean water depth (m) time series (top), the global wavelet spectrum (GWS) (left) and the wavelet power spectrum (right) for H2S −9.14 m salinity records. The GWS is a temporal average of the wavelet spectrum and can be considered as an approximation of their respective Fourier spectrum. Within the GWS, the hatched line represents the mean red noise spectrum, while the arrows indicate peaks in the power of the GWS. The wavelet power spectrum plot compares the period to time with a cone-of-influence indicated by the green contour (results outside this area are affected by boundaries and should not be considered as valid) and 95% confidence interval compared to the background red noise indicated by the blue contour.

CHAPTER 3 – SEASONAL TRENDS IN CALCITE RAFT FORMATION FROM CENOTES RAINBOW, FENO AND MONKEY DUST, QUINTANA ROO, MEXICO - IMPLICATIONS FOR PALEOENVIRONMENTAL STUDIES

Manuscript prepared for:

Palaeogeography, Palaeoclimatology, Palaeoecology

Shawn E. Kovacs [a]*, Eduard G. Reinhardt [a], Christopher Werner [b], Sang-Tae Kim [a], Fred Devos [c], Christophe Le Maillot [c]

[a] McMaster University, School of Geography and Earth Sciences, Hamilton, Ontario, L8S 4K1, Canada
[b] Woodville Karst Plain Project, FL, USA
[c] Mexico Cave Exploration Project (MCEP), Centro Investigador del Sistema Acuifero de Quintana Roo A.C. (CINDAQ), Global Underwater Explorers (GUE), Mexico

* Corresponding author at: McMaster University, School of Geography and Earth Sciences, Hamilton Ontario, L8S 4K1, Canada. Email address: kovacs2@mcmaster.ca

Highlights:

- First record of environmental variables influencing calcite raft formation in anchialine cave systems.
- Supersaturation of $CaCO_3$ in surface waters appears to be the primary factor influencing calcite raft precipitation.
- Intensity and duration of rainfall controls the saturation state of surface water.
- Utilizing time-lapse photography (visual observations) within a cave environment.
- First surface area (calcite raft) record regarding precipitation in a modern anchialine environment.

Keywords:
Calcite Rafts; Coastal karst aquifers; Yucatán; Salinity; Precipitation; Potable water

3.1 ABSTRACT

Calcite raft formation was monitored in three Yucatán cenotes (Rainbow, Feno and Monkey Dust) over a 2-year period. Site specific variables including water temperature, relative humidity, water level and salinity were recorded as well as rainfall (Cozumel). Calcite raft

surface area coverage was monitored through trail cameras that collected photographs every 60 minutes. Accumulation rates were recorded using sediment traps that were collected in May and December of each year. Calcite surface area was calculated using an image segmentation procedure that identified the boundary of objects (edge detection) that share certain pixel characteristics, removed non-points of interest and measured the sum of the area covered by the raft material. An algorithm developed in R was used to extract the encoded timestamp information and merged the surface area abundance data, based on common date and time, to construct a respective time-series record. Results show that large rainfall events have a regional effect on the meteoric water mass (i.e. salinity) as well as the formation of calcite rafts in the cenotes. The large rainfalls cause regional flow toward the coast diluting the supersaturated condition of the aquifer (surface water) and hindered calcite raft formation for days to weeks after the event. Raft precipitation gradually returned with limestone dissolution and reestablishment of $CaCO_3$ supersaturated conditions. The sediment trap and surface area data showed that calcite rafts precipitated relatively constantly throughout the year with only minor deviations with large rainfall events, thus indicating that calcite raft accumulations can provide a suitable paleoenvironmental archive of changing hydrological condition.

3.2 INTRODUCTION

There are few studies on the environmental controls influencing calcite raft formation and no temporal data on the patterns of precipitation or depositional/accumulation rates (Auler and Smart, 2001; Collins et al., 2015a; Jones, 1989; Taylor et al., 2004; Taylor and Chafetz, 2004, 2002; van Hengstum et al., 2015). Rafts are however, ubiquitous in Yucatán caves and also world-wide, forming large accumulations that can be meters in thickness. However, calcite rafts

do not form everywhere, and from our experience in Quintana Roo caves, one cenote or cavern may contain calcite rafts, whereas a close-by cenote in the same cave system will not. There are no environmental data to explain how, and where calcite rafts will form, but their thick accumulations could provide geochemical records of groundwater hydrology and the effects of climate change (wet and dry periods) and sea-level on the aquifer. There are few studies that have used them as a paleo-hydrological proxy but initial results indicate that they are promising paleoenvironmental archives (Collins et al., 2015a; Kovacs et al., 2017a).

This study monitored environmental variables (precipitation, water depth, air and water temperature, relative humidity and salinity) as well as calcite raft surface area and accumulation rates from three cenotes where calcite rafts are presently forming (Monkey Dust, Feno and Rainbow). The goals of the study were to determine: 1) the environmental controls on calcite raft formation that may provide insight on where and when they may form, 2) whether or not there were any temporal trends in calcite raft formation (i.e. time of year or environmental condition) which may bias the paleo-records (i.e. recording aquifer condition during the dry season) and 3) calcite raft accumulation rates to provide baseline information on interpreting sediment accumulation rates in core studies.

3.2.1 CALCITE RAFTS

Calcite ($CaCO_3$) cave formations typically form as a consequence of high pCO_2 saturated solution that off-gas, over saturating the solution and precipitating calcite (Fairchild and Baker, 2012):

$$Ca^{2+} + 2HCO_3 \rightarrow CaCO_3 + H_2O + CO_2 \quad \text{(Eq. 1)}$$

Microcrystalline calcite precipitates that form at the air-water interface are referred to as calcite rafts which in theory, precipitate following the same chemical process in Eq. 1. Rafts precipitate from $CaCO_3$ saturated cave pool water through 1) CO_2 degassing and/or 2) evaporation of H_2O (For extensive review see Taylor et al., 2004; Taylor and Chafetz, 2004; SEM photographs Kovacs et al., 2017a; van Hengstum et al., 2011). Taylor et al. (2004) suggested that nucleation of the raft is promoted by dust, organic particulates, or other particles that could potentially act as a seed (heterogeneous nucleation) on the air-water interface. Jones (1989) proposed deposits nucleated spontaneously with crystals directly precipitating from solution and exploiting prior precipitated raft material as a seed for precipitation. Raft deposits are morphologically distinct as they precipitate at the air-water interface: the upper side of the raft that is exposed to air boundary is planar, as opposed to the bottom side where radiating elongate crystals grow downwards into the water column to form a dentate surface (van Hengstum et al., 2011). Taylor and Chafez (2004) determined calcite rafts located in the Gorman Cave Pools (Texas) that the saturation state of the source water directly influenced calcite crystal habit, where lower calcite saturated waters constituted fused-fabric rafts vs. higher calcite saturated waters were related to open-structured rafts with interlaced fabric (see Fig. 21; Taylor and Chafetz, 2004). Calcite rafts float on the surface, increasing in size as the crystal precipitates coalesce until they sink through breaking the surface tension of water (i.e. surface water agitation, excessive weight; van Hengstum et al., 2011).

Despite many researchers observing calcite rafts precipitating in cave pools and deposited in piles on cave floors in Texas (Taylor and Chafetz, 2004), Bermuda (van Hengstum and Scott, 2011), Mallorca (Fornos et al., 2014) and even Mexico (Collins et al., 2015a), there remains a

lack of information on environmental factors influencing calcite raft precipitation over seasonal cycles or how these precipitates are affected temporally or spatially.

3.3 STUDY AREA

Geographically located between the Gulf of Mexico and the Caribbean Sea, the Yucatán Peninsula is a vast carbonate platform that accumulated during the Cenozoic era (Fig. 1; Ward et al., 1985). The topography of the Mexican State of Quintana Roo (adjacent to the Caribbean coast; Fig. 2) is characterized by low elevation, which has been extensively karstified by the interaction of littoral processes, mixing-zone hydrology, and glacioeustacy (Smart et al., 2006). Consequently, during precipitation events, there is rapid infiltration of meteoric recharge into a highly-fractured surface that drains to a shallow, density stratified, unconfined coastal karst aquifer (Perry et al., 2002). The hydrogeology of this region has a distinctive stratified water column where a meteoric Water Mass (WM; salinity ≈ 1-7 ppt, temperature ≈ 25 °C) is separated by a transition zone (halocline) from the intruding marine WM (~ 35 ppt, ~ 27°C) below based primarily upon density differences (Beddows, 2004; Beddows et al., 2007; Stoessell and Coke, 2006). The halocline depth is a function of distance from the coast (Smart et al., 2006; Werner, 2007). Based on previous measured profiles, the position of the halocline increases by approximately 1.6 m/km moving inland from the coast (Kovacs et al., 2017b), which is comparable to other studies (~2.0 m/km; Smart et al., 2006). Likewise, depending on the position of the halocline, salinity in the meteoric mass varies over the seasonal cycles of wet and dry periods (Kovacs et al., 2017b). Kovacs et al. (2017b) identified a relationship between the mixing of these two (meteoric and marine) WMs as a consequence of shorter timescale and intense events such as hurricanes (i.e. Hurricane Ingrid - 2013), tropical storms (i.e. Tropical

Storm Hanna - 2014), and periods of increase precipitation (a series of unnamed precipitation events in November - 2015). During wetter conditions (i.e. increase in hurricane activity), it is hypothesized that the overall salinity of the meteoric lens would increase as a result of increased mixing with the marine WM (Kovacs et al., 2017b). Whereas during the dry season (absence/less hurricane activity), less turbulent mixing would occur and the net salinity of meteoric WM would be less (Kovacs et al., 2017b). This trend appears to be spatially dependent as well, with areas closer in proximity to the coast experiencing increased mixing as a result of the meteoric lens being thinner towards the coast (Kovacs et al., 2017b). For this study, the sites are further inland where the halocline is deeper at – 22.5 m at Monkey Dust (Chum Kopó; Fig. 2, 3), -17.5 m for Feno (Ich Balam; Fig. 2) and -12 m for Rainbow (Ponderosa; Fig. 2, 3).

The transitional zone between fresh and marine WMs is thought to be predominantly responsible for the chemical dissolution and formation of phreatic anchialine caves (See Fig. 2 - Bishop et al., 2015; Smart et al., 1988; Collins et al., 2015b; van Hengstum et al., 2009). The mechanism for formation is thought to be the mixing of two saturated end-member WMs (fresh and saline) in the transition zone where they form a brackish water zone that is under-saturated due to different ionic strengths (Sanford and Konikow, 1989) with respect $CaCO_3$, resulting in limestone dissolution and conduit expansion (Wigley and Plummer, 1976). It is assumed that the meteoric WM becomes saturated with respect to calcium carbonate ($CaCO_3$) through rainfall infiltrating and dissolving the limestone bedrock allowing the water to reach chemical equilibrium (Smart et al., 2006). Through chemical reaction, supersaturation ($CaCO_3$) in the surface waters can occur during CO_2 off-gassing (Back et al., 1979). This is significant as meteoric WM responds to short-term conditions such as precipitation events, droughts, barometric pressure and tides (Neuman and Rahbek, 2007; Shields, 2007).

Most of the cave systems within Quintana Roo are flooded as a result of Holocene sea-level rise (Collins et al., 2015a; Gabriel et al., 2009; Collins et al., 2015b). Today, these systems are accessible from karst windows, locally known as cenotes, which formed from collapse of the cave and/or cavern ceilings during sea-level low-stands (Finch, 1965).

3.3.1 CLIMATE

The tropical climate of Quintana Roo (Mexico) has wet (summer) and dry (winter) seasons (Hodell et al., 1995; Metcalfe et al., 2000). During the wet season (May to November), the Yucatán Peninsula accumulates an average ~ 1250 mm of rainfall (Hodell et al., 2007; Metcalfe et al., 2015) and experiences a mean air temperature of 34°C (Bauer-Gottwein et al., 2011). In contrast, during the dry season (December to April) the Peninsula has an average air temperature of 25°C (Hodell et al., 2005) with less than 100mm (mean) per month precipitation accumulation (Negreros-Castillo et al., 2003). These seasonal variations in precipitation and temperature are governed by the position of the Intertropical Convergence Zone (For full description see Haug et al., 2003). Due to the porous nature of the karst, there is no surficial streams on the Peninsula, therefore precipitation infiltrates through the vadose zone to the underlying meteoric WM or is lost through evapotranspiration (Beddows et al., 2007; Smart et al., 2006).

3.4 MATERIALS AND METHODS

3.4.1 SITE CHARACTERISTICS

Monitoring stations were placed in cenotes and semi-enclosed caverns where calcite rafts were precipitating (Cenote Rainbow, Feno and Monkey Dust; Fig. 2, 4). Data was retrieved every May and December from 2014 through 2016.

Cenote Rainbow is situated 2.2 km inland (20°29'52.448"N, 87°15'29.651"W) from the coast, between the townships of Puerto Aventuras and Akumal (Fig. 2). This cenote is part of the Sistema X'tabay cave (1394 m in length, max depth = 13.7 m; Quintana Roo Speleological Survey, 2017) which connects to the larger Sistema Ponderosa (15,209 m, max depth = 20.4 m; Quintana Roo Speleological Survey, 2017). Rainbow is a semi-enclosed cenote with geomorphic features containing two elongated elliptical basins of water. A plastic chain was attached to the cavern ceiling and weighted at the bottom using lead weights buried into the sediment. HOBO® conductivity (model U24-001) and water level sensors (U20L-04) were attached at ~30 cm and ~50 cm water depths respectively. Absolute atmospheric pressure (water depth correction) was recorded with a HOBO® U20L-04, as well as air temperature and relative humidity using a HOBO® U23-001 sensor, situated alongside each other at the top of the chain near the cave ceiling. Sediment traps were evenly distributed around the sensor chain in an equidistant pentagonal pattern, ~30 cm water depth (below air-water interface). A camera was attached to the cave ceiling, providing a field-view of the cenote and the chain of sensors and surrounding sediment traps (Fig. 4, 5).

Cenote Feno is located north of Tulum 6.7 km inland from the coast (20°19'17.34"N, 87°25'43.91"W) and is a part of the Sistema Fenomeno cave, and greater Sistema Sac Actun (Quintana Roo Speleological Survey, 2016). Cenote Feno is an enclosed cavern with only a

small opening to the atmosphere. It has a ceiling height of ~3 m and the cavern is oval-shaped, with a small surface area of $10m^2$ (5m length, 2m width) and maximum depth of 1.5 m. Monitoring equipment and sensor placement followed that of Cenote Rainbow.

Cenote Monkey Dust (also known as Cenote Borge), is the furthest inland (Fig. 2; 11.62 km) and is located south of Tulum (20°11'19.817"N, 87°33'4.664"W). It is part of the Sistema Dos Pisos cave system. The cenote shape is elliptical (30m width, 17m length) and has a partial cavern ceiling but is open to the atmosphere. A monitoring station was placed in the north-western corner and sensor placements followed that of Cenote Rainbow.

3.4.2 SENSORS

3.4.2.1 AIR TEMPERATURE (°C) AND RELATIVE HUMIDITY (%)

The HOBO® U23-001 Pro v2 Internal Temperature / Relative Humidity Data Logger was used to measure air temperature (±0.02°C) and relative humidity (±0.03%), recording at 30-minute time intervals. By measuring the relative humidity (the amount of water vapor relative to the temperature of the air) evaporation potential can be determined.

3.4.2.2 SALINITY (ppt) AND WATER TEMPERATURE (°C)

Specific conductance and water temperature (±0.01°C) were measured at 30-minute time intervals using HOBO® Conductivity loggers U24-001 (± 0.5 µS/cm). Integrated in the HOBOware PRO v3.7.8 software, the Data Assistant function converted specific conductance and temperature measurements to salinity, while correcting for sensor drift and biofouling. Surface water samples were collected at the time of sensor download, and independently measured for salinity using a YSI (Model 30) conductivity instrument that was calibrated to

brackish salinity. To measure the WM characteristics (i.e. salinity) of the entire water column, a Hydrolab® Conductivity-Temperature-Depth (CTD) MS5 recorder was used at near proximal locations that permitted measurements (i.e. depth) in both the meteoric and marine WMs.

3.4.2.3 WATER LEVEL (m)

Water level data was recorded (30-minute intervals) in Rainbow, Feno and Monkey Dust using paired HOBO® U20L-04 water level loggers (Sensor depths: Rainbow - 1.0 m; Feno - 0.97 m; Monkey Dust - 1.15m). The Barometric Compensation Assistant (HOBOware PRO v3.7.8) provided reference water level (± 0.5 cm) by compensating for the difference in barometric pressure (one sensor positioned out of the water) and absolute pressure (one sensor fixed at a -30cm water depth). Water level measurements are reported as departures (± m) from the cumulative mean recorded over the study period.

3.4.2.4 PRECIPITATION DATA (mm)

Using a web harvesting technique, daily precipitation data from May 23rd 2014 – May 18th 2016 was extracted from the Cozumel International Airport historical weather archive (https://www.wunderground.com/history/airport/MMCZ). Cancun International Airport and a merged record from Sian Ka'an Biosphere Reserve (Servicio Meteorológico Nacional, 2017) and Puerto Aventuras (ID: IQUINTAN19) were also collected and full datasets and description of methods are available in Kovacs et al. (2017b). As found in Kovacs et al. (2017b), Cozumel was found to be the best quality data and most representative of regional rainfall. Precipitation was represented as a cumulative rainfall departure relative to the mean (Weber and Stewart, 2004).

3.4.2.5 CALCITE RAFT SURFACE AREA (%)

Weatherproof Bushnell HD Trophy CAM HD (Aggressor) and Covert Scouting (MP8) cameras (8-14 megapixel) were placed on the cave wall to provide views of the monitoring sites (Fig. 5a). The cameras were set on time-lapse mode (60-minute frequency), with each photograph timestamped with date and time.

Image processing used ImageJ software (Version 1.50g7; Abràmoff et al., 2004; Schneider et al., 2012). Images were converted to a virtual stack to allow analysis of >900 photographs, saving the options for all photos to be analyzed. To gather workable measurements from the image, a scale was set to known dimensions (I.D. tag fixed to the sensor chain). Photographs were then cropped to size, removing the border frame consisting of information such as timestamp, temperature and moon phase, allowing for strict "field of view" analysis. The contrast of the cropped images were then enhanced to increase the intensity and greyscale colours before converting the image type to 8-bit (binary image), allowing for threshold methods to be applied (Fig. 5b). Image segmentation (thresholding) allows for an image to be partitioned into multiple segments, permitting location of objects and boundaries (edge detection) as a result of classifying every pixel in an image and identifying which ones share certain characteristics (Gonzalez and Woods, 2002). Two different threshold methods were used, Triangle (Zack and Rogers, 1977) for over estimation and Huang (Huang and Wang, 1995) under estimation for identifying pixels and edge boundaries for calcite rafts (For detailed description of threshold methods, refer to Surový et al., 2014). To calculate surface area, ImageJ has an automated option to measure the area of these boundaries. Surface area measurements were corrected for by removing background (non-points of interest) limestone features such as the cave ceiling and walls on the periphery of the cave pool (which changes as a function of water level) (Fig. 5b). A

mean surface area was then calculated using the mean of the over- and under-estimation surface area measurements and transformed into a percentage for comparison (mean surface area divided by the total area of interest). Therefore, the surface area percentage represents an average of these estimations with an uncertainty associated with it, which is constrained by the difference between the upper and lower limits of the surface area measurements. Fig. 5a provides a reference for surface raft area for each of the respective monitoring sites. An R-script was used to merge the calcite raft surface area and timestamp of the image (extracted from photograph metadata) to provide a respective time-series record (R Core Team, 2016).

3.4.2.6 SEDIMENT TRAPS (g)

Sediment traps were the same dimensions (13.7cm in length and a diameter of 5.96 cm) as Collins et al (2015b; 2015c: length to width ratio of 2.3:1). Gardner (1980a) found that the length to width ratio of 2.3:1 collected normally distribution sediment sizes (not favoring large or small particles) and sediment collected in the trap would not be re-suspended with turbulent flow (Gardner, 1980b).

Five sediment traps were deployed around the sensor chains at each site. Traps were affixed to a PVC pipe which was inserted into the sediment so that the traps were at a water-depth of ~ 30cm (Fig. 4b). Traps were collected on a bi-annual basis from May 2014 – May 2016 and filtered before drying (30°C) in a convention oven for 72 hours and then weighted. The individual trap weights were summed for a total weight and standard deviation was calculated (Fig. 7; Table 1)

Since many core studies use accumulation rates (mm/yr), estimates of sediment accumulation rates were determined using our sediment traps (length = 13.7 cm, width = 5.96

cm). The weight of calcite rafts required to cover the bottom of the trap in one layer was empirically determined and the layer was estimated to be 1 mm in thickness, which equates to an approximate weight of 2.00 g of calcite rafts and a calculated deposition rate of 0.14 g/yr. The weights from the sediment traps were then converted to mm/yr (0.07 mm/yr), a unit of measurement comparable to core studies which use the same sized tubing (Kovacs et al., 2017a).

3.5 RESULTS

3.5.1 PRECIPITATION

The precipitation record from the Cozumel International Airport indicates seasonal wet and dry periods (Fig. 6; May 2014 – May 2016) which match well with groundwater level data (Corr. Coef. = 0.59; Fig. 6; 7). The wet season typically began in June and lasted till December (i.e. 7-month duration), with some precipitation events recorded as early as May (2014) and as late as January (2016). This is quite consistent with other published records defining wet/dry periods based upon periodicity and maximum duration of rainfall (Carrillo-Bastos et al., 2010; Curtis et al., 1996). The total amount of precipitation received at the weather station during the 2014 wet season was 4339.59 mm, and 6550.66 mm during 2015 (see also Kovacs et al., 2017b).

Three large precipitation events (over several days) occurred during the study period that influenced calcite raft precipitation, which includes Tropical Storm (TS) Hanna (18/10/2014 – 23/10/2014), and unnamed Precipitation Event 2 (PE2, 13/06/2015 – 16/06/2015) and Precipitation Event 3 (PE3, 26/09/2015 – 27/09/2015; Fig. 8). During each of these events or periods, a large amounts of rainfall (723.9 mm, 501.65 mm, and 374.65 mm) was received in a relatively short periods of time (6 days, 3 days, 2 days).

3.5.2 AIR TEMPERATURE (°C) AND RELATIVE HUMIDITY (%)

The air temperature across all three sites oscillates with the seasons. The warmest temperatures occurred during the rainy season and were cooler in the dryer months (Fig. 6). During the warm/rainy season (defined above), the mean air temperature in Rainbow was 25.29 °C, 24.60 °C in Feno and 25.23 °C for Monkey Dust. During the cooler/dry season the mean air temperature was ~ 1 °C cooler with temperatures at 23.84 °C, 23.58 °C, and 24.01 °C respectively. The highest temperature recorded in Rainbow was 27.73 °C during May 2016 and the coolest was 17.61 °C (January 2016). Likewise, the highest temperature recorded for Feno was 25.61 °C (May 2014), 27.38 °C for Monkey Dust (May 2016), while the coolest temperatures occurred both in January 2016 (18.81 °C - Feno, 18.51 °C - Monkey Dust). There was only a weak correlation ($r = 0.11$) between air temperature and relative humidity as there was a time lag between the period of lowest values during the dry months of the year (Fig. 6; 7).

The relative humidity (%) data from Rainbow (semi-enclosed cavern) and Monkey Dust (open cavern) rarely (< 40 days) went below 90%, indicating the environment is almost totally saturated with water vapor year-round. During the wet season, relative humidity is > 95% and during the dry season it typically was in-between 90-95 %. Unfortunately, the sensor in Cenote Feno (fully-enclosed) malfunctioned and were only able to retrieve data for several months, but the humidity was always high during that time period (Fig. 6). As expected there was a strong correlation between precipitation and relative humidity (0.45; Fig. 7)

3.5.3 WATER TEMPERATURE (°C)

Seasonal trends and patterns are not as apparent in the water temperature record (Fig. 6). Rainbow showed increases in surface water temperature during the wet season and decreases

with the cool/dry season which range between ~0.5 - 1.0 °C. In contrast, records from Feno and Monkey Dust exhibit a gradual (~1°C) increase over the study period, with irregular peaks (i.e. Feno 15-09-2015). The gradual rise in temperature is most likely attributed to instrument drift.

3.5.4 WATER LEVEL (m)

Departure from mean water level (± 0 m) follows seasonal trends in rainfall with the wet season showing higher water levels than the dry (Cor. Coef. = 0.59; Kovacs et al., 2017b; Fig. 6 and 7). The greatest water level was recorded during T.S. Hanna (18/10/2014 – 23/10/2014) at 1.19 m (Rainbow), 0.37 m (Feno) and 0.43 m (Monkey Dust). Water level during PE2 reached respective highs of 0.94 m, 0.98 m, 1.15 m, whereas during PE3 it was lower at 0.34 m (Rainbow), 0.31 m (Feno) and 0.41 m (Monkey Dust) respectively. The variation in water levels between sites was likely due to regional pattern of rainfall, but also the hydraulic conductivity of the shoreline karst and drainage rates into the coastal ocean. Rainbow was the closest site to the coast and had the largest water level fluctuations, likely responding to the collective regional flow of meteoric water from the inland areas. However, the correspondence between the three locations, separated by ~ 40 km indicates a regional aquifer response to seasonal rainfall trends (Fig. 11).

3.5.5 SALINITY (ppt)

Salinity is broadly responding to seasonal variations in mixing between the meteoric and marine WMs but there is also a pronounced short-term response with large precipitation events (Fig. 6, 10, 11). Cenote Rainbow, close to the coast, had precipitation events with a general drop-in salinity during the wet season and higher salinity during the dry (Fig. 6, 10; 0.6 to 1.2

ppt). In Feno and Monkey Dust, the salinity variation were smaller (~0.1 ppt) but still distinct (Fig. 6, 10,11). The high rainfall events (TS Hanna, PE2 and PE3) cause a short-term drop in salinity (eg. 0.4 – 0.6 ppt in Rainbow) followed by a rapid rise (0.4 – 0.8 ppt) in salinity days to weeks after the event. The pattern was consistent over the two-year measurement interval with the sharp drop in salinity a reflection of large inputs of meteoric water and the subsequent rapid rise in salinity a result of mixing between the meteoric and marine WMs, as documented in the Yax Chen cave system (Kovacs et al., 2017b; Esterson, 2002). During the dry season, the high salinity is likely a result of these prior wet-season mixing events (i.e. there is a lag in the salinity). The gradual decline in salinity during the dry season and leading up to the subsequent wet season appears due to smaller rainfalls events which caused reduced flows and less mixing with the marine WM (Fig. 6, 8). This effect was described in Kovacs et al. (2017b) where mixing events close to the halocline were scalable with the amount of rainfall and rise in groundwater level. Either very large rainfalls (TS Hanna) or consecutive medium-sized events seem to be required to invoke a change in salinity of the upper meteoric WM. This high rainfall threshold and the lag in the response caused weak and variable correlations between water level/precipitation and salinity (Fig. 7). Cenote Rainbow showed the largest variability in salinity as it was recording the collective mixing from landward areas to the coast (Fig. 11).

3.5.6 CALCITE RAFT SURFACE ABUNDANCE (%)

The coverage of calcite rafts throughout the study period had mean surface area of 35.6% - Rainbow, 44.3% - Feno and 44.3% for Monkey Dust. The exception was during and after large rainfall events where the surface area drops to 0% in all sites. During TS Hanna, rafts in Rainbow dropped to < 9% (8.5%) on 20/10/2014 and then took 31 days to reach a surface area of > 10 % (11.5%). Likewise with Monkey Dust, rafts dropped to 0% on 23/10/2014 and took 25

days to exceed a surface area of > 10 % (10.6%). During PE 2, calcite rafts in Rainbow dropped to 2.8% on 14/06/2015 and took 30 days to exceed 10 % (10.7%). Feno had a similar response with a decrease in surface area to 5.94% (15/06/2015) and eventually recovered to 10.2 % (26/06/2015) just 11 days after. For PE 3, Rainbow was the only camera recording and calcite rafts dropped to 2.5% on 26/09/2015 and remained less than 5% (4.9 %) until 06/12/2015 when it too failed. There were only weak correlations between precipitation and water level events that caused the decline in rafts while the smaller events did not seem to be have a significant effect. There was a stronger relationship between surface area and salinity as the two parameters are behaved similarly to large rainfall events (0.49; Fig. 7).

3.5.7 SEDIMENT TRAP ACCUMULATION (g)

Sediment trap accumulations through the 2-years showed a general seasonal trend with greater total accumulations during the wet season (May – December; Fig. 9). Collectively, during the wet season, weight totals were 5.16 g (May – Dec 2014) and 8.81 g (May – Dec 2015) whereas during the dry season, the summed weight was 2.11 g (Dec 2014 – May 2015) and 3.19 g (Dec 2015 – May 2016). For Cenote Rainbow, sediment accumulation was relatively constant ranging from 0.41 g to 0.29 g and showed no significant trend with wet or dry seasons (Table 1; Fig. 9). Cenote Feno and Monkey Dust showed trends with wet and dry seasons with higher accumulations during the wet season (Fig. 9; Table 1). The high accumulations recorded for May to Dec 2015 (1.75 g) in Monkey Dust and the higher than expect accumulations in Feno for Dec 2015 – May 2016 correspond to a wet season with high rainfall and which extended into Jan – Feb 2016. Spatial distribution of raft accumulation expressed as standard deviation (1 std) for

the 5 sediment traps during each collection period was relatively uniform over the two years ranging from 0.05 to 0.65.

3.6 DISCUSSION

3.6.1 CALCITE RAFT FORMATION

Camera failures prevented the study from obtaining a full 2-year record in at all the sites, but despite this setback, there is a consistent response showing a relationship between surface area and high rainfall events. Singular large events (i.e. TS Hanna) as well as closely spaced moderate rainfalls events (PE2 and PE3) both resulted in recharge to the meteoric WM and increased coastal discharge. The resulting increased flow within the meteoric WM likely results in mixing between the meteoric and marine WMs and slight increases in salinity in the meteoric WM (Kovacs et al., 2017b). The data shows that irrespective of cavern shape (i.e. openness to the atmosphere, ventilation, or size) or location (i.e. distance from the coast) large rainfall events affect the aquifer on a regional basis in terms of salinity but also hinder calcite raft formation for days to weeks following the precipitation event. Based on the available weather station data, it is hard to estimate the threshold rainfall required to inhibit calcite raft formation because it is dependent on precipitation amount and areal extent. There are only weak correlations with environmental variables but the stronger correlation with salinity indicates that flow and dilution of surface waters seems to be playing a significant role in saturation levels of the upper meteoric water mass. Taylor and Chafetz (2004) underline the importance of $CaCO_3$ saturation state for calcite raft precipitation to occur and with the results of this study indicate that saturation state of the surface water was directly influencing calcite raft formation. Return to supersaturation conditions occurs quickly in days or weeks after the rainfall events and likely through increased

limestone dissolution. As flows wane, surface waters become stagnant, promoting supersaturation through off-gassing of CO_2 and allowing for calcite raft precipitation to occur. It is still unclear why calcite rafts are precipitating in certain areas, but our results suggest that saturation maybe playing a role with micro-topographic or bathymetric conditions providing vertical or areal isolation for supersaturation but additional research is required to test this hypothesis.

3.6.2 IMPLICATIONS FOR PALEOENVIRONMENTAL STUDIES

Recent research has shown that calcite raft deposits can be useful for reconstructing flooding history in Yucatán caves and for reconstructing aquifer condition with Holocene climate change (Collins et al. 2015c; Kovacs et al., 2017b). However, in these studies there was little baseline information on the fidelity of calcite rafts as paleoenvironmental recorders or estimates on sediment accumulation rates to vet age chronologies. This study shows, albeit only for 2-years, that calcite rafts were precipitating relatively continuously, and it is only large rainfall events that introduce a bias in the depositional record. However, calcite rafts begin precipitating relatively soon after the event and would record the effect (i.e. salinity) of the rainfall on the aquifer.

The sediment trap data shows that calcite rafts formed on the surface are in fact sinking and settling to the bottom. The time resolution of this data doesn't allow good comparisons with the other environmental data, but there does seem to be a relationship with seasonality that makes predictable sense, with a tendency for higher accumulations during the wet vs. the dry seasons. The lesser rainfall during the wet period do not dilute surface waters enough to hinder raft formation, but the prevalence of drip water with rainfall are likely causing more surface

disturbance and thus sinking of the rafts. They also tend to accumulate in all the traps, with only minor variability which may relate to localized differences in surface water disturbance (i.e. dripping).

In terms of core studies, the sediment trap data will be useful data for assessing accumulation rates over the longer term (i.e. Holocene). Based on our calculations, the average accumulation rate in 5.96 cm diameter core is ~ 0.4 mm year and thus provides a basis for comparison (i.e. Kovacs et al., 2017b).

3.7 CONCLUSIONS

The 2-year records from Cenotes Rainbow, Feno and Monkey Dust show that calcite rafts precipitate relatively continuously throughout the year and accumulate on the bottom in predictable amounts. The study also shows that large rainfall events dilute the supersaturated upper meteoric WM hindering raft precipitation for days and weeks after the event. Calcite rafts begin to precipitate gradually after the event as supersaturation is achieved as a result of limestone dissolution. Our data shows that large rainfall events affect calcite raft formation regionally and are independent of site-specific variables such as openness to the atmosphere or distance from the coast. These rainfalls also cause regional response in aquifer salinity albeit in different amounts relative to distance from the coast. In terms of calcite rafts as a paleohydrological proxy, the accumulation records are expected to be relatively continuous with only minor biases with large rainfall events.

3.8 ACKNOWLEDGEMENTS

The Calcite Raft Monitoring Project (CRMP) sincerely thanks all students and volunteers who assisted/participated in the field (monitoring setup, maintenance, data downloads and disassemble), Mexico Cave Exploration Project (MCEP) for providing all logistics and Zero-Gravity Mexico (F. Devos, C. Le Maillot and staff) for hospitality as well as managerial assistance. Special thanks to photographer, Ali Perkins, and underwater model Cameron Russo. A Natural Sciences and Engineering Research Council (NSERC) Discovery Grant awarded to EGR and an NSERC CGSD Scholarship to SEK provided financial aid and support for the project.

3.9 REFERENCES

Abràmoff, M.D., Magalhães, P.J., Ram, S.J., 2004. Image processing with ImageJ. Biophotonics Int. 11, 36–42.

Alley, W.M., 2001. Ground Water and Climate. Ground Water 39, 161. doi:10.1111/j.1745-6584.2001.tb02295.x

Auler, A.S., Smart, P.L., 2001. Late Quaternary Paleoclimate in Semiarid Northeastern Brazil from U-Series Dating of Travertine and Water-Table Speleothems. Quat. Res. 55, 159–167. doi:10.1006/qres.2000.2213

Back, W., 1995. Water management by early people in the Yucatán, Mexico. Environ. Geol. 25, 239–242. doi:10.1007/BF00766752

Back, W., Hanshaw, B.B., Pyle, T.E., Plummer, L.N., Weidie, A.E., 1979. Geochemical significance of groundwater discharge and carbonate solution to the formation of Caleta Xel Ha, Quintana Roo, Mexico. Water Resour. Res. 15, 1521–1535. doi:10.1029/WR015i006p01521

Bauer-Gottwein, P., Gondwe, B.R.N., Charvet, G., Marin, L.E., Rebolledo-Vieyra, M., Merediz-Alonso, G., 2011. Review; The Yucatán Peninsula karst aquifer, Mexico. Hydrogeol. J. 19, 507–524. doi:http://dx.doi.org/10.1007/s10040-010-0699-5

Beddows, P.A., 2004. Groundwater Hydrology of a Coastal Conduit Carbonate Aquifer : Caribbean Coast of the Yucatán Peninsula , México. University of Bristol.

Beddows, P.A., Smart, P.L., Whitaker, F.F., Smith, S.L., 2007. Decoupled fresh-saline groundwater circulation of a coastal carbonate aquifer: Spatial patterns of temperature and specific electrical conductivity. J. Hydrol. 346, 18–32. doi:10.1016/j.jhydrol.2007.08.013

Bishop, R.E., Humphreys, W.F., Cukrov, N., Žic, V., Boxshall, G. a., Cukrov, M., Iliffe, T.M., Kršinić, F., Moore, W.S., Pohlman, J.W., Sket, B., 2015. "Anchialine" redefined as a subterranean estuary in a crevicular or cavernous geological setting. J. Crustac. Biol. 35, 511–514. doi:10.1163/1937240X-00002335

Carrillo-Bastos, A., Islebe, G.A., Torrescano-Valle, N., González, N.E., 2010. Holocene vegetation and climate history of central Quintana Roo, Yucatán Península, Mexico. Rev. Palaeobot. Palynol. 160, 189–196. doi:10.1016/j.revpalbo.2010.02.013

Chatters, J.C., Kennett, D.J., Asmerom, Y., Kemp, B.M., Polyak, V., Blank, A.N., Beddows, P.A., Reinhardt, E., Arroyo-Cabrales, J., Bolnick, D.A., Malhi, R.S., Culleton, B.J., Erreguerena, P.L., Rissolo, D., Morell-Hart, S., Stafford, T.W., 2014. Late Pleistocene human skeleton and mtDNA link Paleoamericans and modern Native Americans. Science (80). 344, 750–4. doi:10.1126/science.1252619

Collins, S.V., Reinhardt, E.G., Rissolo, D., Chatters, J.C., Nava Blank, A., Luna Erreguerena, P., 2015a. Reconstructing water level in Hoyo Negro, Quintana Roo, Mexico, implications for early Paleoamerican and faunal access. Quat. Sci. Rev. 124, 68–83. doi:10.1016/j.quascirev.2015.06.024

Collins, S.V., Reinhardt, E.G., Werner, C.L., Le Maillot, C., Devos, F., Meacham, S.S., 2015b. Regional response of the coastal aquifer to Hurricane Ingrid and sedimentation flux in the Yax Chen cave system (Ox Bel Ha) Yucatán, Mexico. Palaeogeogr. Palaeoclimatol. Palaeoecol. 438, 226–238. doi:10.1016/j.palaeo.2015.07.030

Collins, S.V., Reinhardt, E.G., Werner, C.L., Le Maillot, C., Devos, F., Rissolo, D., 2015c. Late

Holocene mangrove development and onset of sedimentation in the Yax Chen cave system (Ox Bel Ha) Yucatán, Mexico: Implications for using cave sediments as a sea-level indicator. Palaeogeogr. Palaeoclimatol. Palaeoecol. 438, 124–134. doi:10.1016/j.palaeo.2015.07.042

Coutino, A., Stastna, M., Kovacs, S., Reinhardt, E., 2017. Variations in salinity of the meteoric lens in cave networks on the Yucatán. J. Hydrol. 551, 715 – 729. doi:10.1016/j.jhydrol.2017.04.022

Curtis, J.H., Hodelle, D.A., Brenner, M., 1996. Climate Variability on the Yucatán Peninsula (Mexico) during the Past 3500 Years , and Implications for Maya Cultural Evolution. Quat. Res. 47, 37–47. doi:10.1006/qres.1996.0042

Finch, W.A., 1965. The karst landscape of Yucatán, RELATÓRIO.

Gabriel, J.J., Reinhardt, E.G., van Hengstum, P.J., Beddows, P.A., Peros, M.C., Davidson, D.E., 2009. Palaeoenvironmental evolution of cenote aktun ha (Carwash) on the Yucatán Peninsula, Mexico and its response to holocene sea-level rise. J. Paleolimnol. 42, 199–213. doi:10.1007/s10933-008-9271-x

Gonzalez, R., Woods, R., 2002. Digital image processing, Prentice Hall. doi:10.1016/0734-189X(90)90171-Q

Gonzalez, S., Hedges, R., Huddart, D., Ohman, J.C., Turner, A., Pompa, A., 2003. Earliest humans in the Americas: new evidence from México. J. Hum. Evol. 44, 379–387. doi:10.1016/S0047-2484(03)00004-6

Haug, G.H., Gunther, D., Peterson, L.C., Sigman, D.M., Hughen, K.A., Aeschlimann, B., 2003. Climate and the Collapse of Maya Civilization. Science (80). 299, 1731–1735. doi:10.2307/482941

Hodell, D.A., Brenner, M., Curtis, J.H., 2007. Climate and cultural history of the Northeastern Yucatán Peninsula, Quintana Roo, Mexico. Clim. Change 83, 215–240. doi:10.1007/s10584-006-9177-4

Hodell, D.A., Brenner, M., Curtis, J.H., 2005. Terminal Classic drought in the northern Maya lowlands inferred from multiple sediment cores in Lake Chichancanab (Mexico). Quat. Sci. Rev. 24, 1413–1427. doi:10.1016/j.quascirev.2004.10.013

Hodell, D. a., Curtis, J., Brenner, M., 1995. Possible role of climate in the collapse of Classic Mayan civilization. Nature. doi:10.1038/375391a0

Huang, L.K., Wang, M.J.J., 1995. Image thresholding by minimizing the measures of fuzziness. Pattern Recognit. 28, 41–51. doi:10.1016/0031-3203(94)E0043-K

Jones, B., 1989. Calcite Rafts, Peloids, And Micrite In Cave Deposits From Cayman Brac, British-West-Indies. Can. J. Earth Sci. 26, 654–664.

Kovacs, S.E., Reinhardt, E.G., Chatters, J.C., Rissolo, D., Schwarcz, H.P., Collins, S.V., Kim, S.T., Nava Blank, A., Luna Erreguerena, P., 2017. Calcite raft geochemistry as a hydrological proxy for Holocene aquifer condition in Hoyo Negro, Quintana Roo, Mexico. *Quaternary Sciences Reviews (Submitted:* JQSR_2017_248)

Kovacs, S.E., Reinhardt, E.G., Stastna, M., Coutino, A., Werner, C., Collins, S. V., Devos, F., Le Maillot, C., 2017. Hurricane Ingrid and Tropical Storm Hanna's effects on the salinity of the coastal aquifer, Quintana Roo, Mexico. J. Hydrol. 551, 703 – 714. doi:10.1016/j.jhydrol.2017.02.024

Metcalfe, S.E., Barron, J.A., Davies, S.J., 2015. The Holocene history of the North American Monsoon: "known knowns" and "known unknowns" in understanding its spatial and temporal complexity. Quat. Sci. Rev. 120, 1–27. doi:10.1016/j.quascirev.2015.04.004

Metcalfe, S.E., O'Hara, S.L., Caballero, M., Davies, S.J., 2000. Records of Late Pleistocene-Holocene climatic change in Mexico - A review. Quat. Sci. Rev. 19, 699–721. doi:10.1016/S0277-3791(99)00022-0

Negreros-Castillo, P., Snook, L.K., Mize, C.W., 2003. Regenerating mahogany (Swietenia macrophylla) from seed in Quintana Roo, Mexico: The effects of sowing method and clearing treatment. For. Ecol. Manage. 183, 351–362. doi:10.1016/S0378-1127(03)00143-9

Neuman, B.R., Rahbek, M.L., 2007. Modeling the groundwater catchment of the Sian Ka'an Reserve, Quintana Roo. Assoc. Mex. Cave Stud. Bulletin 1, 1–209.

Quintana Roo Speleological Survey, 2017. List of Long Underwater Caves in Quintana Roo, Mexico: Tulum, Quintana Roo Speleological Survey.

R Core Team, 2016. R: A language and environment for statistical computing. R Foundation for Statistical Computing.

Servicio Meteorológico Nacional, 2017. Daily Weather Data: Tulum Mexico, Servicio Meteorológico Nacional.

Sanford, W.E., Konikow, L.F., 1989. Porosity development in coastal carbonate aquifers. Geology 17, 249–252. doi:10.1130/0091-7613(1989)017<0249:PDICCA>2.3.CO

Schneider, C.A., Rasband, W.S., Eliceiri, K.W., 2012. NIH Image to ImageJ: 25 years of image analysis. Nat. Methods 9, 671.

Shields, G.A., 2007. A normalised seawater strontium isotope curve : possible implications for Neoproterozoic-Cambrian weathering rates and the further oxygenation of the Earth 35–42.

Smart, P.L., Beddows, P.A., Coke, J., Doerr, S., Whitaker, F.F., 2006. Cave Development on the Caribbean coast of the Yucatán Peninsula, Quintana Roo, Mexico. Geol. Soc. Am. 2404, 105–128. doi:10.1130/2006.2404(10).

Stoessell, R.K., Coke, J.G., 2006. An Explanation for the Lack of a Dilute Freshwater Lens in Unconfined Tropical Coastal Aquifers : Yucatán Example. Gulf Coast Assoc. Geol. Soc. Trans. 56, 785–792.

Surový, P., Dinis, C., Marušák, R., Ribeiro, N.D.A., 2014. Importance of automatic threshold for image segmentation for accurate measurement of fine roots of woody plants. For. J. 60, 244–249. doi:10.1515/forj-2015-0007

Taylor, M.P., Drysdale, R.N., Carthew, K.D., 2004. The formation and environmental significance of calcite rafts in tropical tufa-depositing rivers of northern Australia. Sedimentology 51, 1089–1101. doi:10.1111/j.1365-3091.2004.00661.x

Taylor, P., Chafetz, H.S., 2004. Floating rafts of calcite crystals in cave pools, central Texas, USA: crystal habit vs. saturation state. J. Sediment. Res. 74, 328–341. doi:10.1306/111603740328

Taylor, P.M., Chafetz, H.S., 2002. Petrology and Geochemistry of Calcite Precipitates and Water from Surface and Spelean Environments, Central Texas : Analogs for Non-Marine Carbonate Cements. Gulf Coast Assoc. Geol. Soc. Trans. 52, 935–939.

Toscano, M.A., Macintyre, I.G., 2003. Corrected western Atlantic sea-level curve for the last 11,000 years based on calibrated 14C dates from Acropora palmata framework and intertidal mangrove peat. Coral Reefs 22, 257–270. doi:10.1007/s00338-003-0315-4

van Hengstum, P.J., Reinhardt, E.G., Beddows, P.A., Gabriel, J.J., 2010. Linkages between Holocene paleoclimate and paleohydrogeology preserved in a Yucatán underwater cave. Quat. Sci. Rev. 29, 2788–2798. doi:10.1016/j.quascirev.2010.06.034

van Hengstum, P.J., Reinhardt, E.G., Beddows, P. a., Schwarcz, H.P., Gabriel, J.J., 2009. Foraminifera and testate amoebae (thecamoebians) in an anchialine cave: Surface distributions from Aktun Ha (Carwash) cave system, Mexico. Limnol. Oceanogr. 54, 391–396. doi:10.4319/lo.2009.54.1.0391

van Hengstum, P.J., Richards, D.A., Onac, B.P., Dorale, J.A., 2015. Coastal caves and sinkholes, in: Handbook of Sea-Level Research. pp. 83–103. doi:10.1002/9781118452547.ch6

van Hengstum, P.J., Scott, D.B., Gröcke, D.R., Charette, M.A., Bay, G., 2011. Sea level controls sedimentation and environments in coastal caves and sinkholes 286, 35–50. doi:10.1016/j.margeo.2011.05.004

Veni, G., 1990. Maya utilization of karst groundwater resources. Environ. Geol. Water Sci. 16, 63–66. doi:10.1007/BF01702224

Ward, W.C., Weidie, A.E., Back, W., 1985. Geology and Hydrogeology of the Yucatán and Quarternary Geology of Northeastern Yucatán Peninsula. New Orleans Geol.Soc. 1–160.

Weber, K., Stewart, M., 2004. A critical analysis of the cumulative rainfall departure concept. Ground Water 42, 935–938. doi:10.1111/j.1745-6584.2004.t01-11-.x

Werner, C., 2007. Double-Diffusive Fingering in Porous Media. Florida State University.

Zack, G.W., Rogers, E., 1977. Automatic Measurement of Sister Chromatid Exchange Frequency. J. Histochem. Cytochem. 25, 11–14.

3.10 TABLES

Table 1 - Total sediment trap (n = 5) weights (g ± 1 std) for each site over the collection period.

Date	Cenote	Sum (g)	Std
May – Dec 2014	RainB	0.39	0.10
	Feno	1.75	0.31
	MonkD	3.02	0.26
Dec 2014 - May 2015	RainB	0.41	0.05
	Feno	0.68	0.07
	MonkD	1.02	0.13
May – Dec 2015	RainB	0.29	0.07
	Feno	1.32	0.26
	MonkD	7.20	0.65
Dec 2016 - May 2016	RainB	0.35	0.06
	Feno	1.62	0.45
	MonkD	1.22	0.12

Table 2 - Sediment accumulation rates estimates for a 5.96 cm diameter core tube.

Cenote	Accumulation Rate (mm / yr)	
	2014 - 2015	2015 - 2016
RainB	0.11	0.08
Feno	0.32	0.39
MonkD	0.53	1.11

3.11 FIGURES

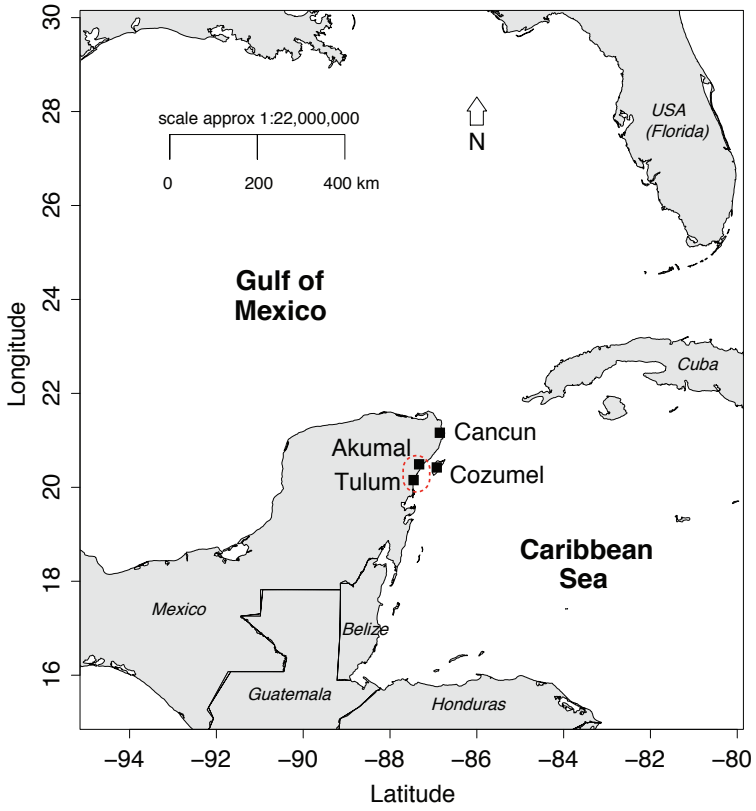

Fig. 1 – Regional map of the Yucatán Peninsula (Mexico) showing the study area.

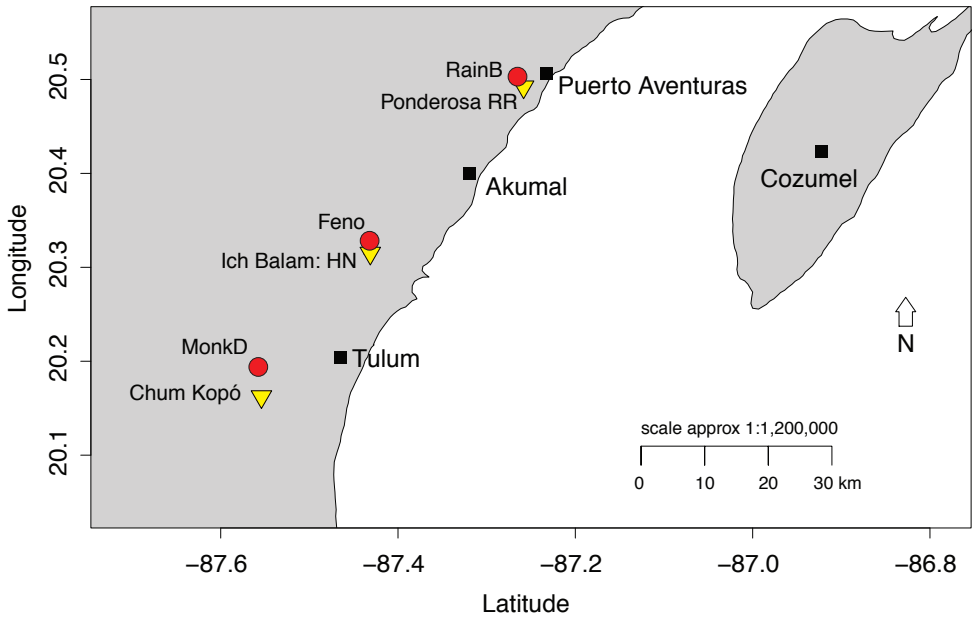

Fig. 2 – Location of monitoring stations (red circles; Rainbow = RainB, Feno, Monkey Dust = MonkD) and Hydrolab® CTD (MS5) profiles (yellow triangles).

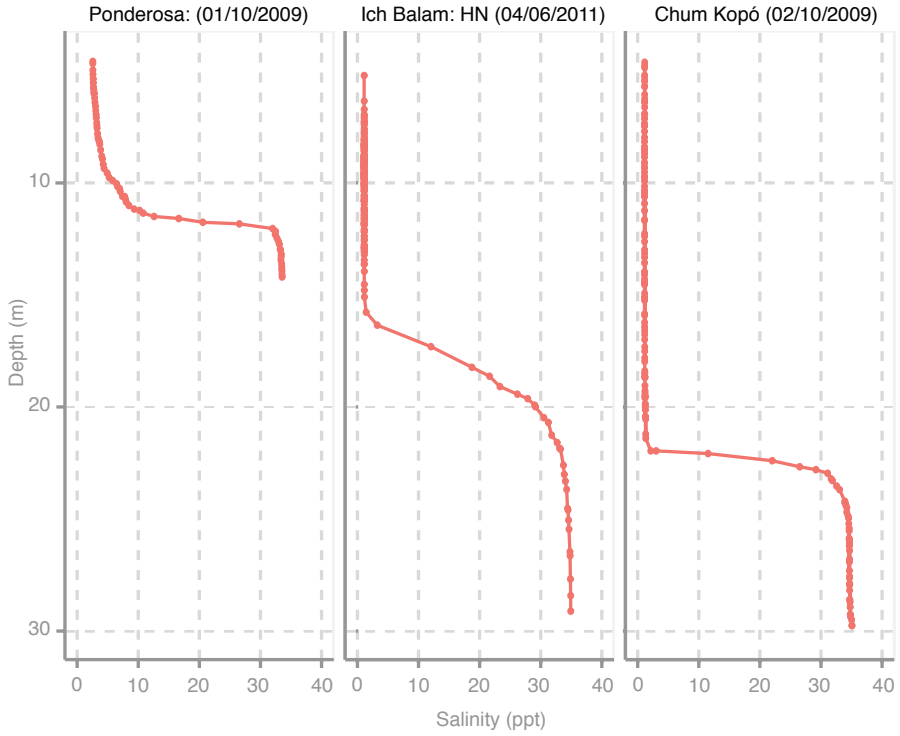

Fig. 3 – Hydrolab® CTD (MS5) profiles showing WM characteristics for respective locations. Dates represented as day, month and year.

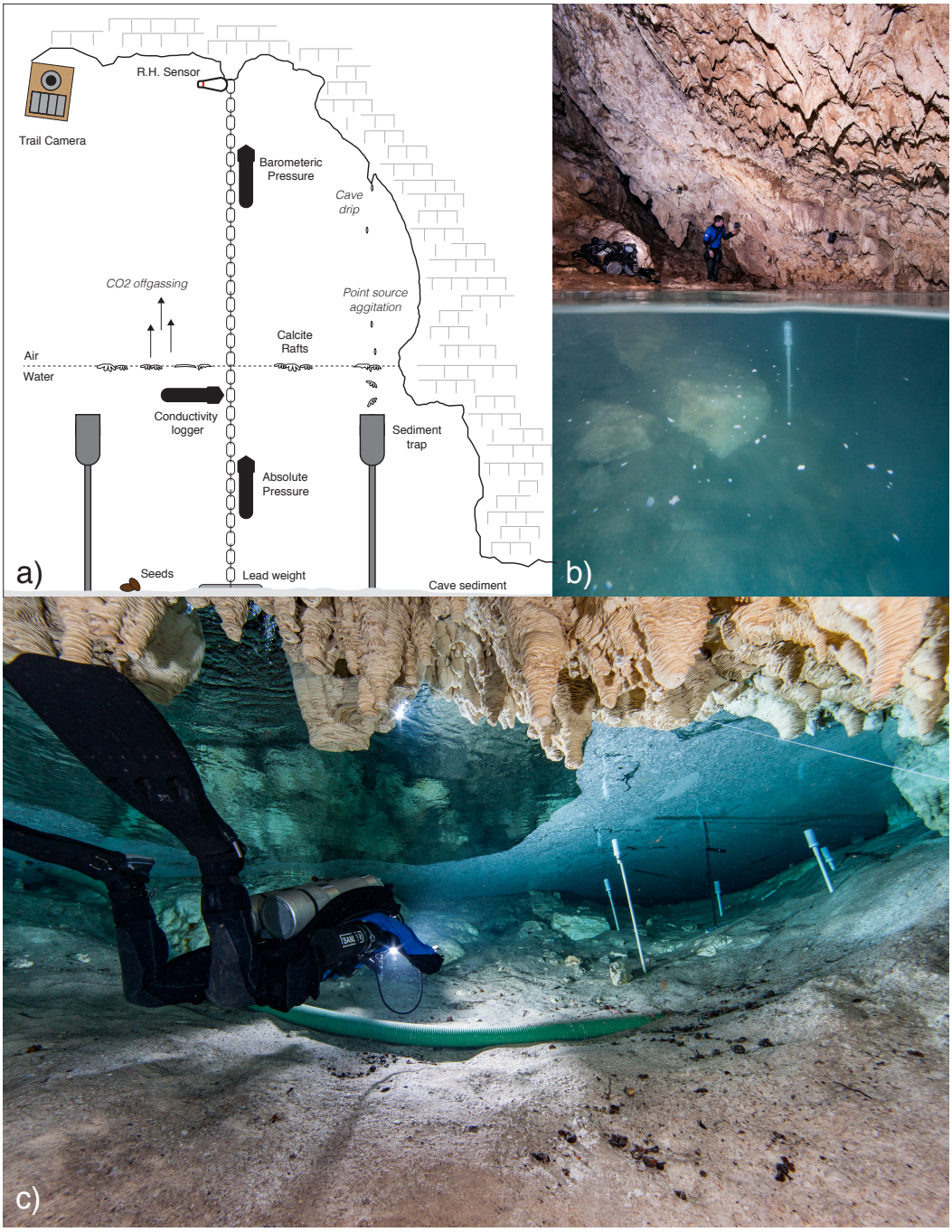

Fig. 4 – a) Monitoring station sensor placement (Cenote Feno). b) Cenote Feno showing sediment trap placements. c) Underwater perspective of sensor and sediment trap position.

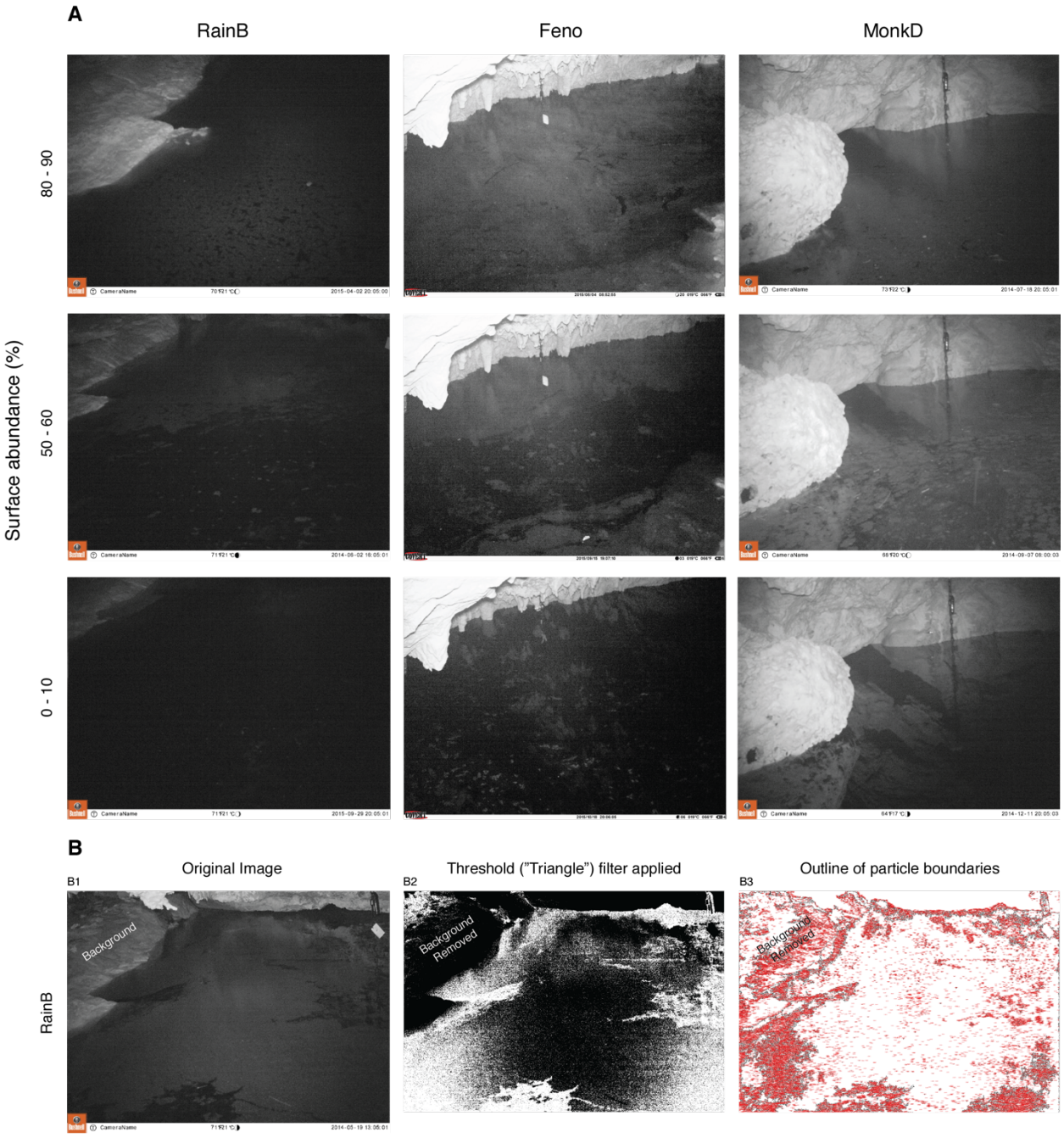

Fig. 5 – a) Time lapse photographs of monitoring sites showing range of calcite raft surface areas. b) Example of outlining process for surface area estimates (1 – 3).

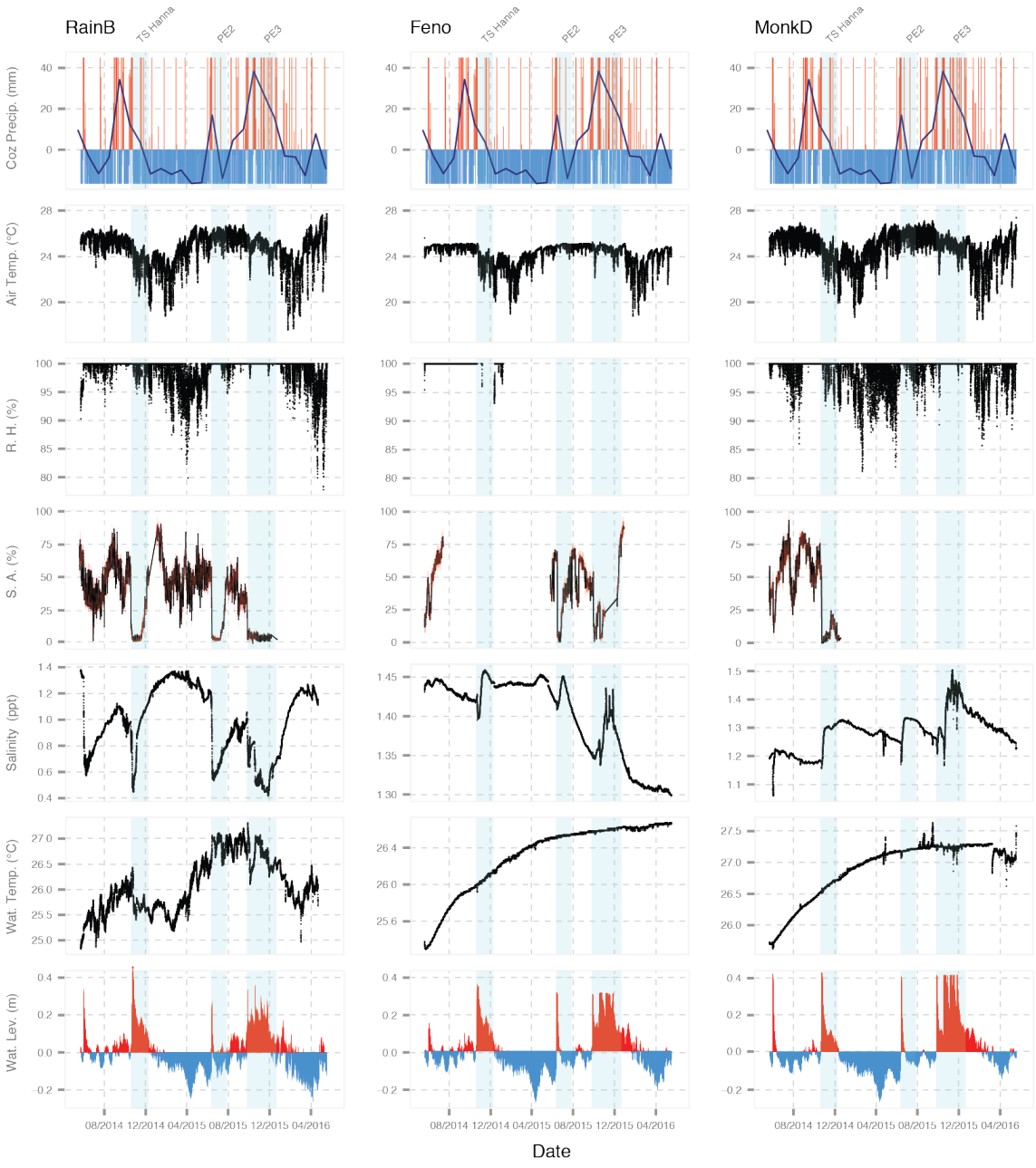

Fig. 6 – Time series plots from May 2014 to 2016 (GMT) for: Cozumel precipitation (mm), air temperature (°C), relative humidity (%), calcite raft surface area (%, plotted as the mean value of the over/under estimates of surface area), meteoric WM salinity (ppt; ~ 30 cm depth), water temperature (°C), water level (m, ± from mean over study period).

Fig. 7 – Correlation matrix of time-series data which has been aggregated to monthly values to emphasize seasonal trends. Upper right portion represents correlation coefficients of each monitoring site as well as collectively together (Cor.). Each relationship is also colour coordinated based on the strength of the collective Cor. Coefficient. Strong positive correlations are represented by the darker shades of green, strong negative correlations are represented by the darker shades of orange, with weaker associations in between represented by the yellowish shade. Diagonally, when each variable is cross-referenced with itself, the data represents a density plot. The bottom portion represents calculated coefficients of determination represented by r^2, explaining the portion of variance in the dependent variable is predictable from the independent variable.

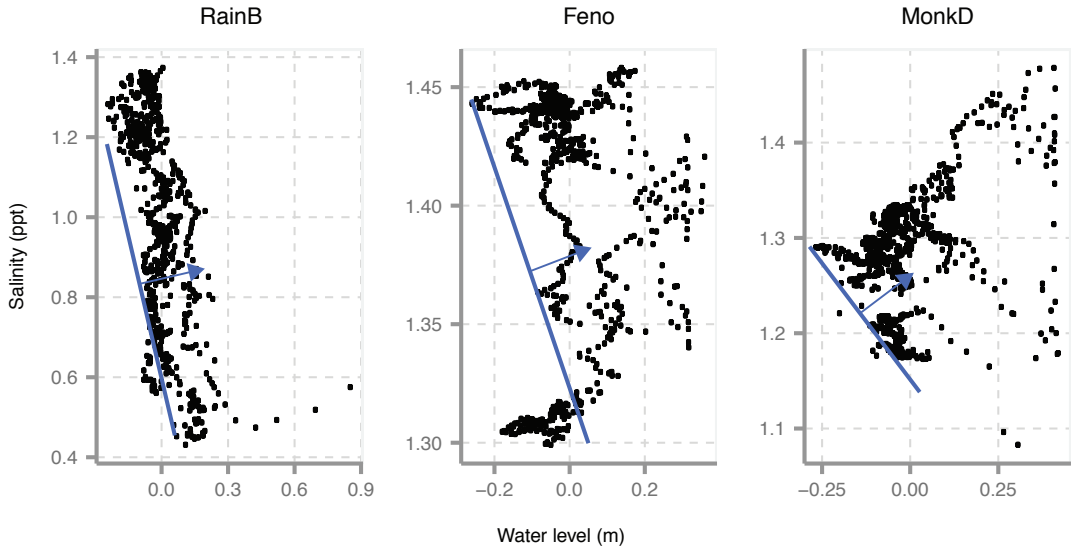

Fig. 8 – Cross-plots between daily meteoric WM salinity (ppt) and departure from mean water depth (m) from Rainbow, Feno and Monkey Dust. Slope of lower threshold line represents seasonal change in salinity with wet and dry periods, and higher salinity departures from this threshold (arrow) represent mixing during precipitation events. Relationship is well defined in Cenote Rainbow, but less so in Feno and Monkey Dust.

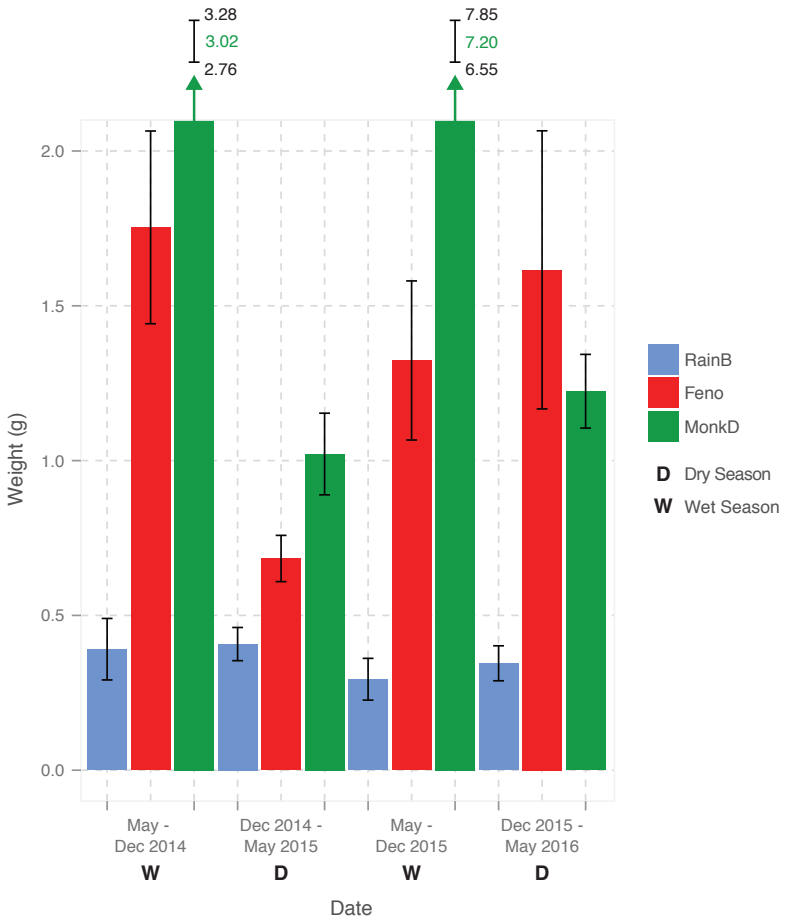

Fig. 9 – Total sediment (g ± 1 std) accumulated in the 5 traps over six month periods.

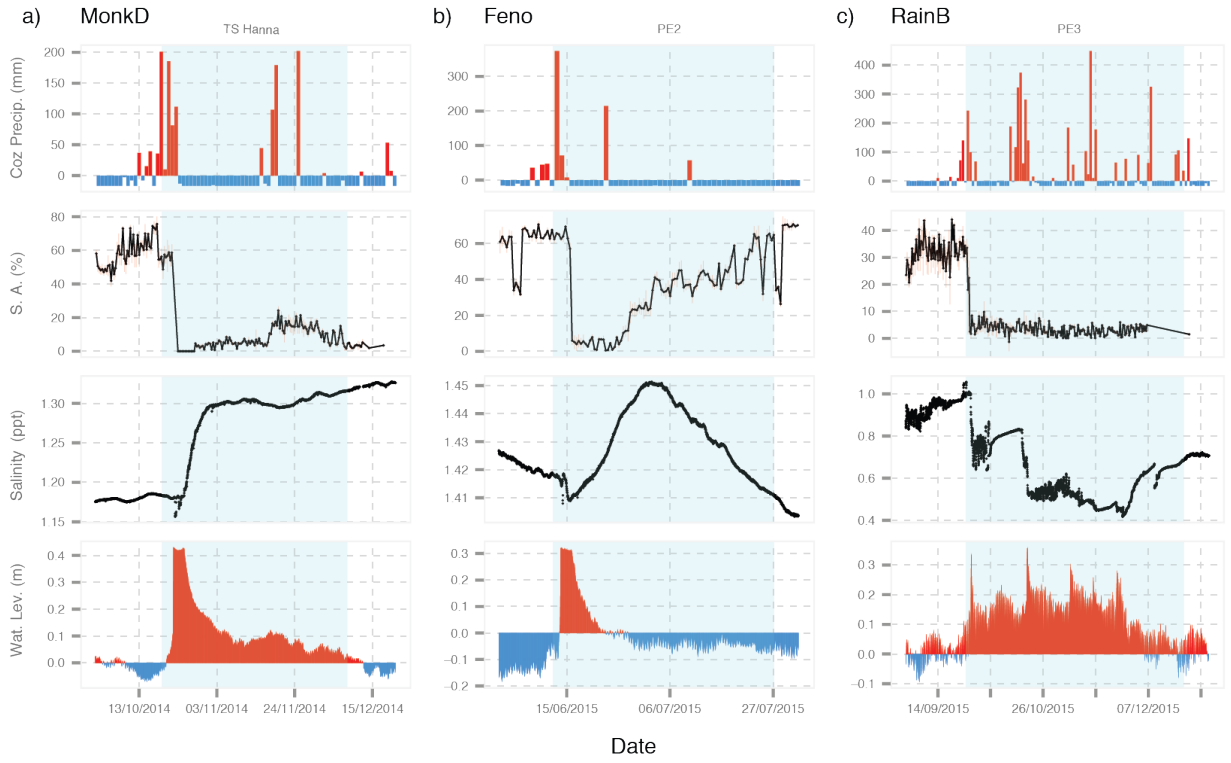

Fig. 10 – Detailed time-series plots (GMT) spanning three precipitation events: a) T.S. Hanna (2014), b) Precipitation Event #2 (PE2) and c) Precipitation Event #3 (PE3). Plots use the same parameters as described in Fig. 6.

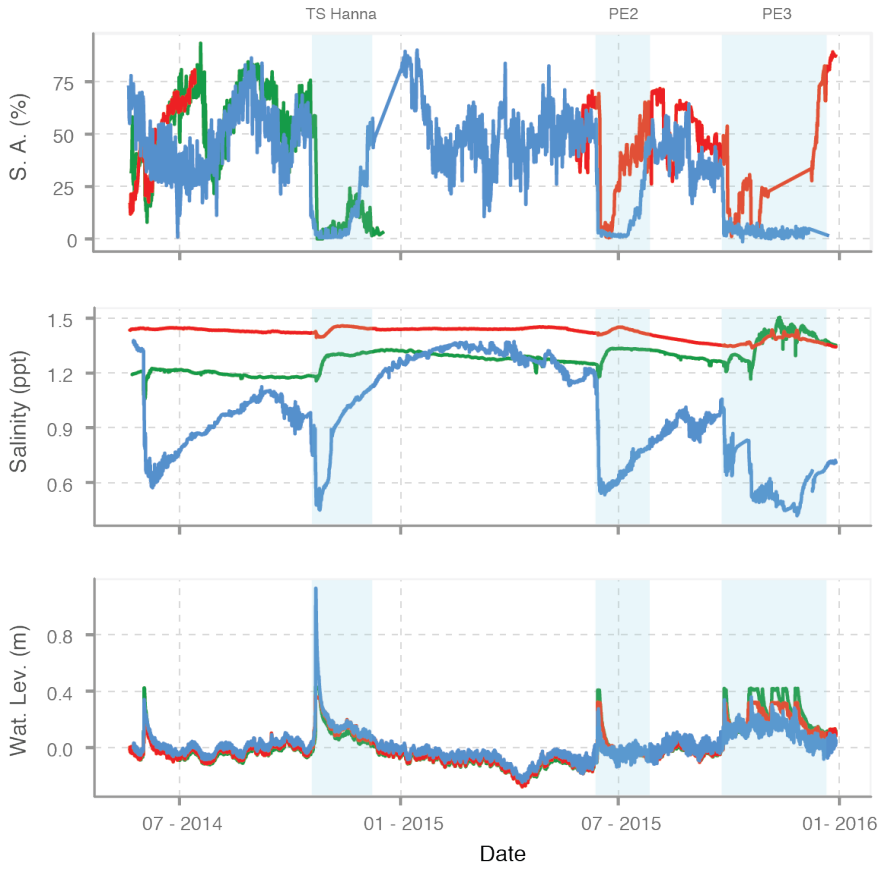

Fig. 11 – Time-series records (GMT) showing interrelationship between the three monitoring sites (Blue = Rainbow, Red = Feno and Green = Monkey Dust).

CHAPTER 4 – CALCITE RAFT GEOCHEMISTRY AS A HYDROLOGICAL PROXY FOR HOLOCENE AQUIFER CONDITION IN HOYO NEGRO, QUINTANA ROO, MEXICO

Manuscript prepared and submitted (reference: JQSR_2017_248)*:*

Quaternary Sciences Reviews (QSR)

Shawn E. Kovacs[1], Eduard G. Reinhardt[1], James C. Chatters[2], Dominique Rissolo[3], Henry P. Schwarcz[1], Shawn V. Collins[4], Sang-Tae Kim[1], Alberto Nava Blank[5], Pilar Luna Erreguerena[6]

[1]*School of Geography and Earth Sciences, McMaster University, Hamilton, Ontario, L8S 4K1, Canada*

[2]*Applied Paleoscience, 10322 NE 190th Street, Bothell, WA 98011, USA*

[3]*Centre of Interdisciplinary Science for Art, Architecture, and Archaeology (CISA3), University of California, San Diego, CA 92093-0436, USA*

[4]*Clarion University, Department of Biology and Geosciences, Clarion, Pennsylvania, 16214, USA*

[5]*Bay Area Underwater Explorers, CISA3/UCSD, Berkeley, CA, USA*

[6]*Subdirectora de Arqueología Subacuática, Instituto Nacional de Antropología e Historia Calle Moneda No. 16, Col. Centro Histórico México, D.F. 06060*

*To whom correspondence should be addressed. Email: kovacs2@mcmaster.ca

4.1 ABSTRACT

Cores (n = 2) of calcite rafts deposits were geochemically analyzed from Cenote Ich Balam and the subterranean cavern Hoyo Negro in the Sac Aktun Cave system located in Quintana Roo, Yucatán Peninsula. Geochemical data obtained, including $^{87}Sr/^{86}Sr$, $\delta^{18}O$, $\delta^{13}C$,

Sr/Ca and Cl/Ca, show local climate-controlled trends spanning the last ~ 8.5 Ka which relate to changing aquifer salinity (meteoric Water Mass - WM) which match other Holocene paleoclimate records. During the wet mid-Holocene (7.8 - 8.5 Ka), aquifer salinity was relatively high at 1.5 - 2.7 ppt and then became gradually less saline (1.0 - 1.5 ppt) during the last 7000 yrs as climate became progressively drier. High salinity during the mid-Holocene is attributed to increased turbulent mixing between the meteoric and underlying marine WM with higher flow during wet periods, a phenomenon that has been recorded with recent instrumental monitoring of the aquifer. Conversely, during dry periods, the meteoric WM may be thinner, but because of reduced marine MW flow contribution, lower salinity is expected. Further research is needed to be conclusive, but during the early Holocene when Naia was living on the landscape (12-13 Ka), the climate was arid and therefore groundwater may have been a potable source of water for early Paleoamericans in the Yucatán. However, due to low sea-level and thus low groundwater level, only deep caverns and pits could have provided aquifer access perhaps focusing habitation and restricting movement on the landscape.

4.2 INTRODUCTION

Human skeletal fossils from phreatic coastal karst systems on the eastern margin of the Yucatán Peninsula show early Pre-ceramic migration and settlement in the Yucatán at the end of the Pleistocene (González et al., 2013; González González et al., 2016, 2008). Recently, a well-preserved, age-constrained Late Pleistocene (13-12ka) female skeleton was found in a deep subterranean pit called Hoyo Negro (HN; *Naia;* HN-5/48; Chatters et al., 2014). Her cranial and dental features share morphometric similarities with other early Paleoamericans, but she has (mt)DNA of Native Americans (Chatters et al., 2014; in press). HN represents the first and only

example of a human skeleton found in direct association with now-extinct Pleistocene megafauna in the Americas (Chatters et al., 2014; Collins et al., 2015). The study of the fossil record in HN is still ongoing, but there are many questions on how early Paleoamerican migrants adapted and subsisted on the Yucatán landscape. The prevailing view is that *Naia* and the animals entering the cave were in search of groundwater, although there is no geological information on the condition of the aquifer during the Holocene to substantiate this claim. Here we present geochemical evidence from calcite raft deposits from HN and Cenote Ich Balam (IB) showing relationships between climate, sea-level and aquifer salinity that provides a basis for understanding subsistence strategies and groundwater potability during the Late Pleistocene/ Early Holocene.

4.2.1 HOYO NEGRO (HN)

HN is a large, submerged, bell-shaped dissolution chamber in the Sac Actun cave system, which has 257 km of mapped passage on the eastern coast of the Yucatán Peninsula in the Mexican state of Quintana Roo (Quintana Roo Speleological Survey, 2017). Due to high porosity and permeability of the karst terrain, groundwater levels in HN and the surrounding region closely track Holocene sea-level (Collins et al., 2015; Gabriel et al., 2009; Smart et al., 2006). As a result, when sea level was low, the region's maze of subterranean passageways would have been accessible to terrestrial animals and humans. Most of the cave passages in Quintana Roo are relatively shallow at ~ 15 m water depth (Quintana Roo Speleological Survey, 2017) which is also the case for HN. However, unlike the other cave systems in the area, the cave passage in HN drops to 48 m in a large circumference pit that contains skeletal remains of many extinct animals as well as *Naia*. Animals may have willingly entered the cave (e.g.,

Cenote Oasis) in search of water and carrion, but may have also fallen into the cave through Ich Balam (IB; a natural trap). Animals navigating the upper cave passages would have fallen into HN as they navigated in the lightless passageways. Humans may have entered the cave with torches for water or ceremonial purposes (burial; González González et al., 2008). In *Naia's* case, she may have slipped and fallen into the pit while accessing groundwater, although it is unknown whether the groundwater was potable at that time.

In anchialine settings, which characterize many karst coastlines, a meteoric Water Mass (WM) rests on a marine WM intruding from the nearby coast. The salinity and thus the potability of the meteoric WM varies spatially with areas closer to the coast having higher salinity than inland areas (Kovacs et al., 2017a). The interaction between the meteoric and marine WM is poorly understood in space and time, with few paleo-environmental records of the potability of meteoric water or how it may have been affected by changes in climate and sea-level (Kovacs et al., 2017a). Consequently, we do not know whether the groundwater was potable at the end of the Pleistocene or the early Holocene, when the climate was dry and when early Paleoamericans arrived to the Yucatán (Chatters et al., 2014; Haug et al., 2001). Groundwater may have been quite important to early migrants who did not construct cisterns to store fresh-water as was done later by the Maya. Also, there are few lakes or rivers in the Yucatán (Metcalfe et al., 2000). Therefore, groundwater from deep caves and pits may have provided a year-round water supply for early Paleoamericans, but with low sea-level and thus groundwater during the early Holocene, only deep caves and pits would have provided limited access. Their spatial extent may have influenced settlement and restricted movement on the landscape.

4.2.2 HYDROLOGICAL SETTING

The Yucatán Peninsula is the aerially emergent portion of the greater Yucatán Platform, a vast limestone platform with a surface area of 300 000 km^2 (Bauer-Gottwein et al., 2011). The Peninsula itself encompasses over 165 000 km^2 of the total surface area, separating the Caribbean Sea from the Gulf of Mexico (Fig. 1), and consists of biogenic limestone that accumulated during the Cenozoic era (Ward et al., 1985). The landscape has low-lying topography and has been extensively karstified by the interaction of glacioeustacy, littoral processes and mixing-zone hydrology (Smart et al., 2006). Consequently, precipitation rapidly infiltrates through the limestone to a shallow, density stratified, unconfined coastal aquifer (Perry et al., 2003). Hydrogeology of the aquifer is influenced by the porous nature of the limestone, which features structural heterogeneities (fissures and fractures), high matrix porosity, and karstic conduits (Kambesis and Coke, 2013). The unconfined aquifer is characterized by a meteoric WM water lens that is separated from the intruding marine WM by the halocline transition zone.

The climate is tropical with distinct wet and dry seasons (Kottek et al., 2006), with monthly average temperatures ranging between 23-29°C, with an average annual temperature of 26°C. The hot/wet season is from May to November, whereas the relatively cooler dry season is from December to April (Hodell et al., 2007). Seasonal precipitation is determined by the movement of the ITCZ, which is controlled by the strength and movement of the Bermuda High and the easterly trade winds (Hastenrath, 2012). Neuman and Rahbek (2007) outline that there is a significant east-west precipitation gradient across the Peninsula, with the most precipitation received on the Caribbean coast side with excess of 1500 mm of precipitation per year, 80% of which falls in the summer wet season (González-Herrera et al., 2002). Quintana Roo surface soil

coverage is sparse and thin, with contemporary vegetation being a tropical arid forest comprised of palms (i.e., rain trees), broad-leafed trees and succulents (Bautista et al., 2011). The outcome of the low-lying topography, lack of deep surface soil and vegetation is that no surface drainage occurs; freshwater rivers are absent in Quintana Roo and only a few lakes are present as a result of karstic drainage (Perry et al., 2003).

Cenote IB and HN are located within the Outland Cave System, a distributary branch of the larger Sac Actun Cave complex (Fig. 2; Quintana Roo Speleological Survey, 2017). IB is a phreatic inland sinkhole (6.74 km from the modern coast), with a small karst window of 3.5 m^2. The water table is approximately 10 m below the upper karst surface. The collapse pile in the cenote is large, with the top of the pile located at 2.5 m water depth, gradually sloping to a depth of approximately 11 m. The composition of the breakdown is massive limestone boulders, covered with seeds, twigs, fine organic matter (OM) and calcite rafts.

HN is 37 m in diameter at -12 m depth and expands to 62 m in diameter at - 48 mbsl, with the current position of the halocline at -18.5m (Fig. 3). The meteoric WM has a lower salinity (1.1 ppt), temperature (25.2°C) and pH (6.8) than the marine WM which is 35.1 ppt, 25.5°C and 7.1 respectively. The pit floor consists of large fragments of limestone breakdown from the overlying ceiling with patchy accumulations of bat guano, calcite rafts and large OM deposits (twigs, charcoal etc.; Chatters et al., 2014; Collins et al., 2015). Seeds are also present within these calcite raft and OM deposits, which would have been transported by fruit bats.

4.2.3 CARIBBEAN SEA LEVEL AND GROUNDWATER LEVEL

Numerous studies have documented the de-glacial sea-level history of the Caribbean region (i.e., Blanchon et al., 2002; Blanchon and Shaw, 1995; Fairbanks, 1989; Lighty et al.,

1982). Toscano and Macintyre (2003) created a western Atlantic sea-level curve that encompasses both coral and intertidal peat sea-level proxies. Their curve constrains the lower and upper boundaries of sea level, respectively but does not account for glacio-isostatic adjustment of the crust (Blanchon, 2005; Gischler et al., 2006). Far-field locations that are both tectonically stable, and experience a sea-level history independent of glacial isostatic adjustment (GIA), are a good approximation of eustacy (Milne and Mitrovica, 2008; Milne and Peros, 2013; Peltier and Fairbanks, 2006). The Yucatán has been tectonically stable since the Late Pleistocene (Ward et al., 1985), and therefore the glacioeustatics sea-level history from the Circum- Caribbean region can be used to infer sea-level position on the Yucatán coast (Bard et al., 2010, 1996; Milne and Mitrovica, 2008; Milne and Peros, 2013). However, based on the water level indicators from HN, the Medina-Elizalde (2013) GIA corrected sea-level curve fits better with the cave depositional record (Fig.4; Collins et al., 2015). The timing for the flooding of the bottom of HN (> 12-13 Ka) is based on skeletal taphonomy, the animal skeletons including *Naia* are largely disarticulated and scattered on the pit bottom, indicating floating decomposition (Chatters et al., 2014).

4.2.4 CALCITE RAFTS

Floating "rafts" of microcrystalline calcite (Fig. 5), commonly referred to as calcite rafts, are autochthonous $CaCO_3$ deposits that precipitate at the air-water interface of quiescent water in cave environments (Taylor and Chafetz, 2004). Rafts form from $CaCO_3$ saturated water through: 1) degassing of CO_2 or 2) evaporation of H_2O (Jones, 1989; Taylor et al., 2004; Taylor and Chafetz, 2004; van Hengstum et al., 2011). The polycrystalline aggregates eventually sink, as a result of surface tension of the raft being exceeded by gravitational forces and/or agitation of the

surface water through hanging roots or drip water, forming conical raft piles on the cave bottom (Fornós et al., 2009; Taylor and Chafetz, 2004; van Hengstum et al., 2011). Kovacs et al. (2017b) documented seasonal trends in calcite raft precipitation using environmental monitoring and sediment traps that showed rafts precipitating relatively constantly throughout the year, but dilution of surface waters during large precipitation events hindered the formation of calcite rafts over short time periods (days). There are advantages to using calcite rafts as a paleohydrological proxy as they: 1) form at the air-water interface providing records of the upper meteoric WM, 2) precipitate abiotically, implying no vital effects on the trace element and/or isotopic systems, 3) in the absence of secondary alterations (i.e., recrystallization, dissolution), the mineral material preserve readily in the stratigraphic record. Collins et al. (2015) was the first study to core these deposits and noted particle-size changes that may reflect rising water levels in IB.

4.2.5 GEOCHEMICAL PROXIES OF PALEOSALINITY

Previous research used $^{87}Sr/^{86}Sr$ in biotic and abiotic carbonates as a paleosalinity proxy in marginal marine environments (Bryant et al., 1995; Holmden and Hudson, 2003; Peros et al., 2007; Reinhardt et al., 1998). Using a two-component mixing equation ($^{87}Sr/^{86}Sr$, [Sr]), deviations from the worldwide marine value ($^{87}Sr/^{86}Sr = 0.709175$) can be attributed to fresh-water dilution. Thus, salinity can be calculated if the fresh and marine water end-members are known or can be estimated (Reinhardt et al., 1998). Sr isotopes are also often paired with O and C isotopes, as well as trace elements. These analyses are relatively lower-cost and thus can provide higher resolution records (Sr/Ca; eg. Holmden et al., 1997; Peros et al., 2007). However, $\delta^{18}O$ and $\delta^{13}C$ values can be affected by processes other than mixing of fresh and marine water, including vital effects during biotic $CaCO_3$ precipitation, evaporation or changes in the isotopic

composition of the fresh and marine water end-members (e.g. vegetation or precipitation; McDermott, 2004; Reinhardt et al., 2001). Most research on C and O isotopes has been conducted on biotic precipitates in marginal marine coastal environments, but it is equally applicable to the abiotic calcite rafts.

4.3 METHODOLOGY

Multiple cores (n= 12; diam. 6 cm) were collected in IB and HN with locations and stratigraphy described in Collins et al. (2015). Calcite rafts cover the limestone breakdown pile in the center of IB, while the calcite raft pile in HN had a distinct cone geometry (~ 2.5 m in diam. and 1 m high) with several coalescing lobes (Fig. 6). Calcite raft piles are not abundant on the bottom of HN and are mostly thin, low-profile coverings on the breakdown limestone. Two calcite raft abundant cores were selected for geochemical analysis, Core 4 (~ 65 cm) was from 12.3 m depth in IB and Core 9 (~ 45 cm) was collected at 42 m depth in HN and was taken in the largest calcite raft pile found on the bottom of the pit. One additional Core (Core 10) was collected adjacent to Core 9 (approx. 5 cm away) in the same raft pile.

All these cores except Core 10 (left intact) were previously sampled at 1 cm intervals by Collins et al. (2015). Subsamples for the geochemical analyses were rinsed in deionized water before being pulverized into a homogenous powder using a mortar and pestle. Aliquots of ~100 µg were then weighed for analyses. Oxygen and carbon isotope analyses (n = 53) were conducted at McMaster University, Hamilton Ontario (Research Group for Stable Isotopologues - MSRI) using a VG Autocarb system attached to an Optima mass spectrometer. δ values are expressed in permil (‰) relative to Vienna PeeDee Belemnite (VPDB). The precision of the analyses is ± 0.05 ‰ for both $\delta^{13}C$ and $\delta^{18}O$. Accuracy was checked by analysis of a laboratory

standard calibrated against NBS 19 calcite. Samples (n = 19) for strontium isotopic analysis were obtained by first dissolving calcite raft material in 0.4 mL 1M HCl, then separated using cation exchange columns and a Sr selective crown ether resin (Pin and Bassin, 1992). Analyses used a VG 354 multi-collector mass-spectrometer in the Radiogenic Isotope Laboratory at McMaster University. National Bureau of Standards (NBS) 987 yielded a $^{87}Sr/^{86}Sr$ ratio of $0.71025 \pm 2x10^{5}$ on replicate analyses.

Salinity can be determined using a two-component mixing equation using the fresh and marine water end-member Sr concentrations ([Sr]; ppm) and $^{87}Sr/^{86}Sr$ values (e.g. Peros et al., 2007; Reinhardt et al., 2001). However, paleosalinity can also be determined from $^{87}Sr/^{86}Sr$ measurements alone. We calibrated a mixing curve using data from three cenotes that are precipitating calcite rafts: Box Ek, La Concha, and Peno, which are in a landward transect from the coast (located at 2.43 km, 6.46 km and 6.70 km). Salinities in the three locations were 2.6 ppt, 1.1 ppt and 1.3 ppt respectively, and had $^{87}Sr/^{86}Sr$ values (0.70845, 0.70825, 0.70834) that reflect salinity relative to mixing with modern seawater (0.709175 @ 35 ppt) (Fig. 7). Extrapolating the curve to 0.5 ppt salinity, the $^{87}Sr/^{86}Sr$ value would be ~ 0.7080, which is close to Miocene seawater (Fig. 2; McArthur et al., 2001; Perry et al., 2009) corresponding to the age of the limestones that underlie the Yucatán (Perry et al., 2009). Hodell et al. (2004) recorded an $^{87}Sr/^{86}Sr$ value of 0.70831 for the surface waters of Aktun Ha and salinity was measured in 2007 at 1.5 ppt in van Hengstum et al. (2009) (Fig. 7).

Elemental composition was measured using X-ray fluorescence (XRF) and an ITRAX-XRF core scanner (Cox Analytical Systems) at the McMaster University Core Scanning Facility. Prior to analysis, the samples were washed in deionized water to remove pore-water that could potentially contain major ions (i.e., Cl^-; Lazar et al., 2014). As the cores had been previously

sampled, a sequential sample holder was used to analyze the sediment at 1 cm intervals (Gregory et al., 2017). Each ~ 1 cm^3 sample reservoir is evenly packed with sediment and aligned in sequential order. Samples were analyzed using the Cr heavy element (Cr-HE) X-ray source (30kv, 10 mA, exp. time =15 secs., step-size= 200 μm). Ten measurements from the central portion of each sample reservoir were averaged and their standard deviations calculated. Core 10, which was taken adjacent to Core 9, was analyzed as a complete core for comparative purposes and shows similar trends as the samples from C9. The core was repeatedly flushed using deionized water and then split for analysis with the same XRF parameters as the previously taken samples.

Conductivity and strontium concentrations of cenote water were measured by Actlabs (Activation Laboratories located in Ancaster, Ontario, Canada). Salinity was calculated using the free software from Five Creeks™ (http://www.fivecreeks.org/monitor/sal.html). A Perkin Elmer Sciex ELAN 9000 Inductively Coupled Plasma Mass Spectrometry (ICP-MS) was used to determine strontium concentration values.

Temperature, pH and salinity of the water column in HN was measured using a calibrated MS5 Hydrolab MiniSonde®. The sonde was gradually lowered through the water column using SCUBA (Kovacs et al., 2017a).

The electron microscopy work was completed at the Canadian Centre for Electron Microscopy (CCEM) using a JEOL 6610LV Scanning Electron Microscope.

4.3.1 RADIOCARBON AGE DATING

Calcite rafts and seeds were ^{14}C dated by DirectAMS™ in Seattle, Washington, U.S.A. Six paired seed/calcite rafts ^{14}C ages were used to estimate the hard-water effect. Seeds and

calcite rafts were selected from the same intervals using the cores in this study (C4 and C9) but also cores (C3, C5, C6; 2015; Table 1) from Collins et al. (2015). Seeds were pretreated using an acid/alkali/acid wash prior to analysis and calcite rafts were cleaned with deionized water. A hard-water offset of ~ 1300 ^{14}C years BP was obtained for all samples (Fig. 8). The Dissolved Inorganic Carbon (DIC) of the water column in HN was also analyzed at the WM Keck Carbon Cycle AMS Laboratory at UC Irvine (Table 2). The DIC in the shallowest sample at -12 m had an age offset of ~ 1600 ^{14}C years BP, which is consistent with our values. We would expect the calcite rafts to have a smaller age offset as they precipitate at the air/water interface because that environment includes more atmospheric carbon than the DIC deeper in the water column.

Age models of the cores are based on a comparison of radiocarbon dates on calcite and seeds, including five calcite raft samples (1-2, 17-18, 33-34, 49-50 and 63-64 cm) with one seed (63-64 cm) for C4, and six calcite raft samples (0-1, 10-11, 21-22, 30-31, 43-44, and 45-46 cm) and one organic seed (45-46 cm) for C9. Conventional radiocarbon ages were calibrated to years before present (cal yrs BP) using IntCal09 and a hard-water effect of 1300 yrs based on our estimate.

4.4 RESULTS

4.4.1 AGE MODELS

Core 9 in HN shows accumulation (~ 45 cm) over approximately 400 yrs from 7900 - 8300 cal yrs BP (~ 0.11 cm/yr) (Fig. 9). There are no age reversals in the core, and accumulation is relatively slow (~ 10 cm) between 8000 - 8300 cal yrs BP and then becomes more rapid from 7900 to 8000 cal yrs BP, with the accumulation of ~ 30 cm of sediment. The rapid accumulation over a relatively short time may represent a period when conditions were ideal for raft formation

and/or there was a vigorous point source of water agitation causing the rafts to sink (e.g. drip water from the cave ceiling). The accumulation rate of calcite rafts is, however, fairly-high relative to the modern sediment trap studies in Kovacs et al. (2017b), but that rate (0.007 cm/yr) was from only three sites and represents only 2 years, so we don't have extensive data for comparison.

In contrast, the accumulation rate for Core 4 from IB is lower, but appears to be more constant. The accumulation rate over approximately 7000 cal yrs BP in C4 is considerably less at ~ 0.010 cm/yr and is very similar to the accumulation rate that was calculated in Kovacs et al., (2017b). Raft accumulation in C4 may have been episodic over the short-term, but this cannot be resolved with the ^{14}C ages. The breakdown pile in the center of IB is covered with a mixed pile of calcite rafts and organic matter (OM); raft deposition likely varied in terms of time and place as water level increased in the cenote (e.g. location of roots and drip-water; Collins et al., 2015). However, based on the available ^{14}C dates that we have and at least over the long-term, the accumulation rate appears constant in C4, but may include short-term hiatuses.

4.4.2 ISOTOPIC PROXIES: ^{87}Sr / ^{86}Sr, $\delta^{18}O$ AND $\delta^{13}C$

The $^{87}Sr/^{86}Sr$ and $\delta^{13}C$ values from C4 (0-7000 cal yrs BP) and C9 (7900-8300 cal yrs BP) show a shift in aquifer hydrology sometime between 7000 - 8000 cal yrs BP (Tables 3 and 4; Fig. 11). The $^{87}Sr/^{86}Sr$ values from C9 in HN vary between 0.70840 - 0.70860 and the $\delta^{13}C$ values are between -5.0 to -8.0 ‰. C4 from IB has lower $^{87}Sr/^{86}Sr$ values at 0.70820 - 0.70840 and $\delta^{13}C$ values of -11.3 to -11.6 ‰, respectively, with the $\delta^{13}C$ values also showing an increase through time. Based on the Sr mixing relationship between fresh and marine water, this corresponds to a salinity shift of ~ 1.5 - 2.7 ppt in C9 and 1 - 1.5 ppt in C4. $\delta^{18}O$ values show

little difference between C4 and C9, varying between -6.6 to -7.2 ‰ but are in the typical range for calcite in equilibrium with the local freshwater (e.g. van Hengstum et al., 2009). As found in previous studies from coastal lagoons and estuaries, there is often a strong positive correlation between $^{87}Sr/^{86}Sr$ and $\delta^{13}C$, which is related to mixing of fresh and marine waters. $\delta^{18}O$ values, however, do not always show a good relationship to the other geochemical proxies for a variety of reasons (e.g. evaporation) but especially if the isotopic difference between fresh and marine water is not large (e.g. Peros et al., 2007; Reinhardt et al., 2003; van Hengstum et al., 2009).

4.4.3 ELEMENTAL PROXIES Cl/Ca AND Sr/Ca

Similarly, Cl/Ca and Sr/Ca values show a large difference between C9 and C4. Cl/Ca values in C9 ranged from 0.010 - 0.040, and Sr/Ca from 0.010 - 0.075 while in C4 they ranged from 0.001 - 0.002 and 0.003 - 0.008, respectively. As with the $\delta^{13}C$ values, there is a decrease in both values through time, but for different reasons. Sr/Ca ratios in abiotic calcite can be a reflection of temperature partitioning of Sr into the calcite crystal lattice, but in this instance, it is more likely a reflection of mixing between low [Sr] in meteoric water (i.e., < 3 ppm; Reeve and Perry, 1994) vs high [Sr] in marine water (~ 8 ppm, Levinson, 1968). Our cenote measurements show that the freshwater contains < 1.6 ppm [Sr] (Fig. 7).

The Cl/Ca ratios reflect salinity as well as, if not better than, the other proxies. Chlorine (Cl^-) behaves conservatively with the mixing of fresh and marine waters and its concentration relates directly to salinity (e.g. Perry et al., 2009). However, Cl^- is not partitioned into the calcite crystal lattice like other ions (e.g. Sr^{2+}, Mg^{2+}, Ba^{2+}) so we would not expect to see trends in Cl/Ca ratios (Fairchild et al., 2006, 2001). The calcite rafts were washed with deionized water to remove any remnants of saline surface water, and thus [Cl^-] is associated with the calcite raft

material itself with a likely source being fluid inclusions. Scanning Electron Microscope (SEM) analysis of the calcite shows crystal rhombs extending down from the flat top of the raft. These intersecting rhombs of calcite appear to be trapping water inclusions as the crystals coalesce and grow in size, so the Cl/Ca is a reflection of pore water salinity at time of precipitation. The Cl/Ca records match the Sr/Ca values (Figure 10), both showing decreasing trends in core C9, but also consistent with higher $^{87}Sr/^{86}Sr$ and $\delta^{13}C$ values and the salinity (Figure 11; Table 4). $^{87}Sr/^{86}Sr$ does not show a decreasing trend in C4 but it is not as sensitive as Cl/Ca for discerning small changes in salinity.

4.4.4 DIAGENESIS

Core C9 is presently in the marine WM due to Holocene sea-level rise, but during the time of deposition, the calcite rafts formed on the surface of the meteoric WM. We find no evidence for diagenetic effects associated with immersion of C9 in the marine WM following Holocene sea-level rise. For example, SEM analysis of the calcite rafts shows no overgrowths or pitting (i.e., secondary alteration effects) on the upper surface of the rafts and they retain their original crystal fabric. Calcite rafts form through the addition of down- and out-ward precipitating crystal rhombs which form a flat top at the air water interface. Diagenetic calcite overgrowths would form on all surfaces, but we observed no rhombs on the flat, upper portion of the rafts (Fig. 5). As discussed previously, there was close agreement between the isotopic ($\delta^{13}C$, $^{87}Sr/^{86}Sr$) and elemental (Cl/Ca, Sr/Ca) proxies, although the $\delta^{18}O$ values did not show a significant change. In terms of diagenesis, the similarity in $\delta^{18}O$ values from C4 and C9 is worth noting, as we would expect C9 to exhibit $\delta^{18}O$ values reflecting isotopic re-equilibrium with sea water (i.e., ~ 0‰) if altered by the marine WM. As the $\delta^{18}O$ values show no variation between

C4 and C9, and C4 has always been in the meteoric WM unlike C9, there do not appear to be any significant diagenetic effects.

4.5 DISCUSSION

4.5.1 WATER LEVEL AND CALCITE RAFT DISTRIBUTION IN HN and IB

The sedimentary and micropaleontological evidence indicates that there was water at the bottom of HN by at least 10 Ka, but skeletal taphonomy (i.e., the nature of skeletal articulation) is consistent with the presence of water at the bottom of the pit prior to that date (Collins et al. 2015; Chatters et al., 2014). As discussed in Collins et al. (2015), the early Holocene position of the sea level is uncertain, which affects the reliability of using sea level as an accurate predictor of groundwater level in HN. Collins et al. (2015) also speculated that there may have been an underlying aquitard, allowing "ponding" to occur in HN. Large rainfalls likely caused increased water levels in the pit at least over the short-term, as evidenced by a "bathtub ring" of reddish brown staining, the depth distribution of skeletal elements, and distribution of dates on wood from ledges on the pit walls.

Calcite raft formation would not begin until there was a permanent water body in HN after ~ 10 Ka. The calcite rafts in C9 accumulated between 7900 - 8300 Ka and when water levels in HN were considerably higher. There is no direct data for water level between 8 ~ 10 Ka, but groundwater reaches the floor of the upper cave passages by ~ 8000 yrs BP (~ -12 msl) based on the IB core stratigraphy (Collins et al. 2015). There is considerable uncertainty on sea-level position from 8 - 10 Ka (Fig. 4), but using the sea level curve as a guide, the water level in HN was anywhere from ~ -12 to -30 msl when the raft pile formed (C9). This would be equivalent to a water depth inside HN of from 15 to 30 m. Calcite raft formations have not been

studied extensively and our local observations are based upon shallow cave systems (< 10 m depth) with no deep-water examples. However, a 30 m water depth seems deep for the formation of such a distinctive, cone-shaped raft pile (i.e. vs. a more sheet like distribution). It could be that this location had a vigorous/preferred point-source water agitation (e.g. drip water) that was active over a short time-period which would explain the high sediment accumulation rate in C9 (~ 0.11 cm/yr). More research is required with better examples, but regardless of the water depth in HN, the calcite rafts formed at the air/water interface as water level was rising in the pit.

Calcite rafts formed more extensive accumulations in IB as groundwater level rise decelerated in the mid-Holocene. In IB, they are covering the breakdown pile to the extent that many of the limestone boulders associated with the collapse of the cavern ceiling are buried under raft material. There are no recognizable raft pile cones, and the breakdown pile is one large accumulation of calcite rafts and OM (see Collins et. al., 2015 for details on stratigraphy). IB opens directly to the land surface, which is not the case in HN, and the water surface is much closer to the land surface, making it more subject to extensive and frequent organic input (i.e., surface run off) as well as extensive raft coverage as compared to the enclosed cavern at HN. However, the more extensive calcite raft coverage might also be due to the deceleration of sea-level rise over the past 7 Ka coupled with a drier climate, which would allow for prolonged periods of supersaturation of $CaCO_3$ in the surface water column. Kovacs et al. (2017b) found seasonal trends (wet vs. dry) in the formation of calcite rafts in modern-day localities, with high levels of rainfall diluting calcite saturated surface water and thus hindering raft formation.

4.5.2 AQUIFER SALINITY AND RELATIONSHIP WITH WET AND DRY PERIODS

The IB core spans the last 7500 yrs and the HN core covers from 7800-8400 yrs BP. Therefore, further research is required to extend the records to the late Pleistocene/early Holocene. Nevertheless, there are relationships between the records collected thus far, and those from published climate proxy records that allow inferences to be made on the potability of groundwater during 12-13 Ka when *Naia* lived on the landscape (Fig. 11).

4.5.2.1 CONSISTENCY BETWEEN GEOCHEMICAL PROXIES

Raft geochemistry shows a marked shift as groundwater floods the upper cave passages at ~ 8000 yrs BP. C9 from HN is a short record of the meteoric WM (7800-8300 cal yrs BP), but the data differs in terms of magnitude and variability relative to that obtained from C4 in IB, which spans a longer period (~ last 7000 yrs) after the upper cave passages were flooded. The values of $^{87}Sr/^{86}Sr$, Cl/Ca, Sr/Ca and $\delta^{13}C$ show the larger changes, whereas $\delta^{18}O$ shows little change between the cores.

The Sr mixing relationship between fresh and marine water indicates a 1-3 ppt shift in meteoric WM salinity between C9 and C4. However, this maybe an under estimate of salinity, as the mixing equation assumes that the $^{87}Sr/^{86}Sr$ value of the freshwater end-member is similar to that of present day. When groundwater level was lower and dissolving older limestone, $^{87}Sr/^{86}Sr$ of the freshwater end-member may have been lower and closer to Miocene seawater values (i.e., $^{87}Sr/^{86}Sr = 0.7082$) (McArthur et al., 2001). The $\delta^{13}C$ record covaries with that of $^{87}Sr/^{86}Sr$, which is often the case in estuarine systems. But the large (~ -5‰) shift in $\delta^{13}C$ between C4 and C9 is also likely due to other factors affecting DIC composition (i.e.

composition of surficial vegetation), and not just mixing as the DIC in groundwater is typically high in karst terrains (Peros et al 2007; Pohlman et al., 1997; Reinhardt et al., 2003).

Similarly, Cl/Ca and Sr/Ca show a large decrease from C9 to C4, which is consistent with a drop in salinity, as concentrations of Cl^- and Sr^{2+} are lower in fresh water than in marine water (Perry et al., 2009). Seawater (~35 ppt) has an approximate Cl^- concentration of 19,400 mg/L while freshwater (0.001 to 0.5 ppt) typically ranges from 1 - 250 mg/L. Therefore, the decrease in Cl/Ca between C9 and C4 is consistent with at least a 3 ppt salinity change (~ 1500 mg/L Cl), assuming the freshwater end-member is <100 mg/L. The Cl/Ca ratio is ~ 20 times higher in C9 relative to C4 in IB where the modern salinity is 1.1 ppt (Figs. 3 and 11). Assuming a linear response between Cl/Ca and salinity, this would be equivalent to a much higher salinity than estimated by the Sr isotopes but would corroborate better with the $\delta^{13}C$ records. Further research is required to calibrate the relationship between Cl/Ca and salinity to be definitive, but the evidence does indicate a significant shift in salinity between C4 and C9.

The $\delta^{18}O$ values, however, show only a minor difference between C4 and C9, with values ranging from -7.2 to -6.6 ‰ in both cores. $\delta^{18}O$ values, alone, are not always useful for salinity reconstructions in coastal environments (i.e., open systems) because the $\delta^{18}O$ signature will be influenced by precipitation, groundwater and/or marine water (Peros et al., 2007). As will be discussed, aquifer hydrology over wet/dry periods is likely obscuring the salinity shift in the $\delta^{18}O$ values.

4.5.2.2 HYDROLOGICAL IMPLICATIONS

Previous studies have shown Holocene changes in annual precipitation linked with the migration of the ITCZ (e.g. Hodell et al., 2005; Metcalfe et al., 2000). Haug et al. (2001) used Ti

records from laminated sediments from the Cariaco basin near Venezuela to show dry conditions during the Younger Dryas (~11 - 13 Ka) and then a rapid rise in moisture between 11 and 10 Ka. Levels then peak at 9 Ka, followed by a gradual drying trend to present. Further to the north, the $\delta^{18}O$ record in ostracod shells (*Candona sp.*) from Lake Miragoane in Haiti shows dry conditions at ~ 12 Ka and then increasing moisture to ~7 Ka and then a gradual drying to present. Based on the calcite raft geochemistry in IB and HN, the aquifer was more saline (2-3 ppt) during wetter conditions at 8 - 8.5 Ka than it was after 7 Ka, when climate conditions were becoming more arid (1-2 ppt). Assuming that the hydrological regime was similar to that of present, this shift in salinity may reflect, in part, a change in hydrology associated with decreasing flow in the meteoric WM. Recent monitoring (~ 4 yrs) using salinity sensors in the meteoric WM shows that intense rainfalls (i.e., hurricanes and tropical depressions) cause turbulent mixing with the underlying marine WM increasing the salinity of the meteoric WM (a change from 6 ppt to > 9 ppt) as it flows towards the coast (Coutino et al., 2017; Kovacs et al., 2017a). Kovacs et al. (2017b) found a similar relationship between salinity and rainfall in cenote surface waters. During drier periods, the meteoric WM might be thinner, but less saline, due to less frequent and intense precipitation events. The salinity records from IB show a gradual decrease associated with the increase in aridity since the mid-Holocene documented in Lake Miragoane and the Cariaco Basin. A gradual decrease in meteoric WM salinity over the past 7 Ka was also recorded in a nearby but separate cave system (Aktun Ha) using microfossils (thecamoebians and foraminifera), which supports the similar salinity trend. It also demonstrates that the aquifer is responding at least on a regional basis (as shown in Cores 2 and 4 of van Hengstum et al., 2010: Fig 4).

As discussed, $\delta^{18}O$ values show little change over the past 8.5 Ka, unlike other geochemical data. However, it does corroborate when the $\delta^{18}O$ of precipitation is considered. Based on data from the stalagmite specimen ("Chaac"), collected from the Tzabnah (Tecoh) Cave in the northern Yucatán (20° 45′N, 89° 28′W; 20 m above sea level), $\delta^{18}O$ is ~ 3 ‰ higher during dry periods (-3.4 ‰) than during wet ones (-6.4 ‰) (Medina-Elizalde et al., 2010). $\delta^{18}O$ record being isotopically enriched during dry periods while isotopically depleted during wet periods would be consistent with our records. Increased mixing between the meteoric and marine WMs during wet periods would cause an increase in the salinity of the meteoric WM, resulting in contradictory salinity and $\delta^{18}O$ records. During wet periods, the $\delta^{18}O$ value of the meteoric WM (i.e., typically lower than 0 ‰) would increase due to mixing with underlying marine water (~ 0 ‰). Dry periods would experience less mixing and thus maintain $\delta^{18}O$ nearer the precipitation value that is isotopically enriched. As a result, the overall long-term pattern of $\delta^{18}O$ in the WM would be small.

The large drop in salinity of at least 1 - 2 ppt (i.e., fresher) with the flooding of the upper cave passages (i.e. C9 in HN vs C4 in IB), which is the approximate depth for most of the cave passages in the area is also significant and worth noting. There is little information on the early hydrological regime (eg. stratification) when groundwater levels were lower, but the lack of cave passages in the older, deeper limestone (eg. porosity) suggests that it may have been quite different than present. As discussed, the presence of large detrital OM scattered at the bottom of HN and on ledges suggests precipitation induced flows in the upper cave passages, which may have caused increased turbulent mixing with the underlying marine WM prior to the flooding of the upper passages. Because of the ~ 1 Ka gap in the depositional sequence, we have no record of the transition, but it does appear to have occurred quickly, suggesting a change in state of the

hydrologic system at least in HN. Further research is needed, but the predominance of shallow cave passages in the Quintana Roo suggests that their flooding, in addition to climatic change, may have influenced aquifer hydrology.

4.5.2.3 THE LATE PLEISTOCENE – EARLY HOLOCENE AQUIFER

Inferring, based on Ti records, that regional climates were arid during the Younger Dryas (c. 12 900 to c. 11 700), Quintana Roo would have been relatively dry (Fig. 11). With lower sea levels eliminating most surficial lakes and rivers, groundwater would have been the only year-round potable water source, if accessible. At this time, during infrequent precipitation events, there may have been small pools of water in shallower cave passages as a result of cave deposits or formations (such as rimstone dams) allowing water to pond, but these sources would not be large, abundant or available throughout the year. When sea-level was low, the only way to access groundwater would have been through deep cave passages or karst pits like HN. Most of the explored cave passages in Quintana Roo are shallow (~ -10 to -12 msl; Quintana Roo Speleological Survey, 2017) with few known locations in the immediate vicinity of HN that have deeper passages or caverns (e.g. Fig. 2; The Pit, Cenote Angelita; Quintana Roo Speleological Survey, 2017). Groundwater from these subterranean bodies of water could only be accessed through these deep locations. Given that our assessment of the aquifer salinity during dry periods is correct, during the early Holocene, these would be the only year-round reliable sources of potable water for early Paleoamericans. Smaller pools located in the upper passages, as discussed before, may have provided some, but not a sustainable source of potable water for extended periods of time.

More paleo-hydrological data from the early Holocene is required to be definitive, but our results raise important implications for how early populations may have existed on the landscape. If our arguments hold true, early Paleoamericans would not be able to range extensively, and would need to plan movements with the availability of ponded cave water and the few lakes in the area. It is unclear whether the existing lakes would have contained water at this time, and whether that water was potable, but it does appear that early migrants to the area likely planned their dry-season movements around deep aquifer access points which provided a year-round source of freshwater at least in this part of the Yucatán.

4.6 CONCLUSIONS

This study from HN shows for the first time that calcite rafts can be used as a paleohydrological proxy. They are diagenetically stable abiotic $CaCO_3$ precipitates that record groundwater chemistry, and form large accumulations in Yucatán caves with large spatial extent. They also provide records of the upper meteoric WM which what would be accessed by early Paleoamericans. The several geochemical records ($^{87}Sr/^{86}Sr$, Cl/Ca, Sr/Ca and $\delta\,^{13}C$) from IB and HN show similar and predictable trends in aquifer salinity with the Cl/Ca records showing the most promise in terms of understanding groundwater hydrology. Analyzing intact cores with the efficiencies of XRF core scanners (e.g. ITRAX) will provide increased resolution and spatial extent.

The hydrology of the aquifer responded to regional climate with wet periods having higher meteoric WM salinity vs. drier intervals where it was less saline. In addition, it is likely that flooding of the upper cave passages with Holocene sea-level rise is also having an effect on hydrology of the aquifer. Further research will extend the spatial and temporal data to determine

whether there is variability in the aquifer response, but the replication of similar salinity trends using microfossils in Actun Ha (< 7Ka) indicates at least a regional response.

4.7 ACKNOWLEDGMENTS

The authors would like to acknowledge and thank the anonymous reviewers for their feedback and recommendations to improve the quality of the manuscript. We are grateful to the numerous volunteers, especially Alex Alvarez, Ali Perkins and Cameron Russo, who have contributed immeasurably to the project (i.e., surveying, sample retrieval) as well as Roberto Chavez for photography. We also appreciate the expert assistance of Zero Gravity Dive Center and ProTec Dive Center Tulum, as well as the generosity of Marcia Kirby. Financial support for the project was provided through NSERC Discovery Grants (EGR and STK), CFI-JELF (EGR), NSERC CGSD (SEK), and National Geographic Expeditions Council (EGR and ANB). Research in Hoyo Negro is conducted under the auspices of the Subdirección de Arqueología Subacuática of the Instituto Nacional de Antropología e Historia (INAH), and with the permission of the Consejo de Arqueología del INAH. We would especially like to thank Adriana Velázquez Morlet and María de los Ángeles Olay Barrientos.

4.8 REFERENCES

Bard, E., Hamelin, B., Arnold, M., Montaggioni, L., Cabioch, G., Faure, G., Rougerie, F., 1996. Deglacial sea-level record from Tahiti corals and the timing of global meltwater discharge. Nature 382, 241–244. doi:10.1038/382241a0

Bard, E., Hamelin, B., Delanghe-Sabatier, D., 2010. Deglacial meltwater pulse 1B and Younger Dryas sea levels revisited with boreholes at Tahiti. Science (80). 327, 1235–1237. doi:10.1126/science.1180557

Bauer-Gottwein, P., Gondwe, B.R.N., Charvet, G., Marin, L.E., Rebolledo-Vieyra, M., Merediz-Alonso, G., 2011. Review; The Yucatán Peninsula karst aquifer, Mexico. Hydrogeol. J. 19, 507–524. doi:http://dx.doi.org/10.1007/s10040-010-0699-5

Bautista, F., Palacio-Aponte, G., Quintana, P., Zinck, J.A., 2011. Spatial distribution and development of soils in tropical karst areas from the Peninsula of Yucatán, Mexico. Geomorphology 135, 308–321. doi:10.1016/j.geomorph.2011.02.014

Blaauw, M., 2010. Methods and code for "classical" age-modelling of radiocarbon sequences. Quat. Geochronol. 5, 512–518. doi:10.1016/j.quageo.2010.01.002

Blanchon, P., 2005. Comments on "Corrected western Atlantic sea-level curve for the last 11,000 years based on calibrated 14C dates from Acropora palmata framework and intertidal mangrove peat" by Toscano and Macintyre [Coral Reefs (2003) 22:257-270]. Coral Reefs 24, 183–186. doi:10.1007/s00338-004-0472-0

Blanchon, P., Jones, B., Ford, D.C., 2002. Discovery of a submerged relic reef and shoreline off Grand Cayman: Further support for an early Holocene jump in sea level. Sediment. Geol. 147, 253–270. doi:10.1016/S0037-0738(01)00143-9

Blanchon, P., Shaw, J., 1995. Reef drowning during the last deglaciation: evidence for catastrophic sea-level rise and ice-sheet collapse. Geology. doi:10.1130/0091-7613(1995)023<0004:RDDTLD>2.3.CO

Bryant, J.D., Jones, D.S., Mueller, P.A., 1995. Influence of Freshwater Flux on $^{87}Sr/^{86}Sr$ Chronostratigraphy in Marginal Marine Environments and Dating of Vertebrate and Invertebrate Faunas. J. Paleontol. 69, 1–6.

Chatters, J.C., Kennett, D.J., Asmerom, Y., Kemp, B.M., Polyak, V., Blank, A.N., Beddows, P.A., Reinhardt, E., Arroyo-Cabrales, J., Bolnick, D.A., Malhi, R.S., Culleton, B.J., Erreguerena, P.L., Rissolo, D., Morell-Hart, S., Stafford, T.W., 2014. Late Pleistocene human skeleton and mtDNA link Paleoamericans and modern Native Americans. Science (80). 344, 750–4. doi:10.1126/science.1252619

Chatters, J. C., D. Rissolo, J. Arroyo-Cabrales, T. W. Stafford, Jr., B. M. Kemp, A. Alvarez, A. Nava-Blank, F. Attolini, P. A. Beddows, E. Reinhardt, S. Kovacs, S. Collins, S. Morell-Hart, R. Chávez-Arce, S. Bird, and P. Luna Erreguerena, *In Press* Hoyo Negro: Tapping the Paleoanthropological and Paleoecological Potential of a Deeply Submerged, Underground Chamber on the Yucatán Peninsula, Mexico. In *The Archaeology of Underwater Caves*. Oxbow Books

Collins, S. V., Reinhardt, E.G., Rissolo, D., Chatters, J.C., Nava Blank, A., Luna Erreguerena, P., 2015. Reconstructing water level in Hoyo Negro, Quintana Roo, Mexico, implications for early Paleoamerican and faunal access. Quat. Sci. Rev. 124, 68–83. doi:10.1016/j.quascirev.2015.06.024

Coutino, A., Stastna, M., Kovacs, S., Reinhardt, E., 2017. Variations in salinity of the meteoric lens in cave networks on the Yucatán. J. Hydrol. 551, 715 – 729.

doi:10.1016/j.jhydrol.2017.04.022
Fairbanks, R.G., 1989. A 17,000-year glacio-eustatic sea level record: influence of glacial melting rates on the Younger Dryas event and deep-ocean circulation. Nature 342, 637–642.
Fairchild, I.J., Baker, A., Borsato, A., Frisia, S., Hinton, R.W., McDERMOTT, F., Tooth, A.F., 2001. Annual to sub-annual resolution of multiple trace-element trends in speleothems. J. Geol. Soc. London. 158, 831–841.
Fairchild, I.J., Smith, C.L., Baker, A., Fuller, L., Spötl, C., Mattey, D., McDermott, F., 2006. Modification and preservation of environmental signals in speleothems. Earth-Science Rev. 75, 105–153.
Fornós, J.J., Ginés, J., Grácia, F., 2009. Present-day sedimentary facies in the coastal karst caves of Mallorca Island (western mediterranean). J. Cave Karst Stud. 71, 86–99.
Gabriel, J.J., Reinhardt, E.G., van Hengstum, P.J., Beddows, P.A., Peros, M.C., Davidson, D.E., 2009. Palaeoenvironmental evolution of cenote aktun ha (Carwash) on the Yucatán Peninsula, Mexico and its response to holocene sea-level rise. J. Paleolimnol. 42, 199–213. doi:10.1007/s10933-008-9271-x
Gischler, E., Toscano, M.A., Macintyre, I.G., 2006. Comment on "Corrected western Atlantic sea-level curve for the last 11,000 years based on calibrated 14C dates from Acropora palmata framework and intertidal mangrove peat" by Toscano and Macintyre. Coral Reefs 22:257-270 (2003), and their response in Cor. Coral Reefs 25, 273–286. doi:10.1007/s00338-006-0101-1
González-Herrera, R., Sánchez-y-Pinto, I., Gamboa-Vargas, J., 2002. Groundwater-flow modeling in the Yucatán karstic aquifer, Mexico. Hydrogeol. J. 10, 539–552. doi:10.1007/s10040-002-0216-6
González, A.H., Terrazas, A., Stinnesbeck, W., Benavente, M.E., Avilés, J., Rojas, C., Padilla, J.M., Velásquez, A., Acevez, E., Frey, E., 2013. The First Human Settlers on the Yucatán Peninsula: Evidence from Drowned Caves in the State of Quintana Roo, Mexico. Paleoamerican Odyssey 323–337.
González González, A.H., Sandoval, C.R., Acevez Nunez, E., Olguin, J., Ramirez, S.A., del Rio Lara, O., Erreguerena, P.L., Velazquez Morlet, A., Stinnesbeck, W., Terrazas Mata, A., Benavente Sanvicente, M., 2016. Underwater and Maritime Archaeology in Latin America and the Caribbean, 2nd ed, Evidence of early inhabitants in submerged caves in Yucatán, Mexico. Routledge, New York.
González González, A.H., Sandoval, C.R., Mata, A.T., Sanvicente, M.B., Stinnesbeck, W., O, J.A., De, M., 2008. The Arrival of Humans on the Yucatán Peninsula: Evidence from Submerged Caves in the State of Quintana Roo, Mexico. Curr. Res. Pleistocene 25, 1–24.
Gregory, B.R.B., Reinhardt, E.G., Macumber, A.L., Nasser, N.A., Patterson, R.T., Kovacs, S.E., Galloway, J.M., 2017. Sequential sample reservoirs for Itrax-XRF analysis of discrete samples. J. Paleolimnol. 57, 287–293. doi:10.1007/s10933-017-9944-4
Hastenrath, S., 2012. Climate dynamics of the tropics, 8th ed. Springer Science & Business Media.
Haug, G.H., Hughen, K.A., Sigman, D.M., Peterson, L.C., Röhl, U., Peterson, L.C., Overpeck, J.T., Kipp, N.G., Imbrie, J., Hughen, K.A., Overpeck, J.T., Peterson, L.C., Trumbore, S.E., Peterson, L.C., Haug, G.H., Hughen, K.A., Röhl, U., Hastenrath, S., Greishar, L., Röhl, U., Abrams, L.J., Yarincik, K.M., Murray, R.W., Peterson, L.C., Members, C.,

Hammen, T. van der, Hooghiemstra, H., deMenocal, P., Ortiz, J., Guilderson, T., Sarnthein, M., Fairbanks, R.G., Mayle, F.E., Burbridge, R., Killeen, T.J., Berger, A., Loutre, M.F., Maslin, M.A., Burns, S.J., Fedorov, A. V., Philander, S.G., Clement, A.C., Seager, R., Cane, M.A., Peterson, M.J., Chang, P., Ji, L., Li, H., Hodell, D.A., Brenner, M., Curtis, J.H., Guilderson, T., Cane, M., Clement, A.C., 2001. Southward migration of the intertropical convergence zone through the Holocene. Science 293, 1304–8. doi:10.1126/science.1059725

Hodell, D.A., Brenner, M., Curtis, J.H., 2007. Climate and cultural history of the Northeastern Yucatán Peninsula, Quintana Roo, Mexico. Clim. Change 83, 215–240. doi:10.1007/s10584-006-9177-4

Hodell, D.A., Brenner, M., Curtis, J.H., 2005. Terminal Classic drought in the northern Maya lowlands inferred from multiple sediment cores in Lake Chichancanab (Mexico). Quat. Sci. Rev. 24, 1413–1427. doi:10.1016/j.quascirev.2004.10.013

Hodell, D.A., Quinn, R.L., Brenner, M., Kamenov, G., 2004. Spatial variation of strontium isotopes (87Sr/86Sr) in the Maya region: A tool for tracking ancient human migration. J. Archaeol. Sci. 31, 585–601. doi:10.1016/j.jas.2003.10.009

Holmden, C., Creaser, R.A., Muehlenbachs, K., 1997. Paleosalinities in ancient brackish water systems determined by 87Sr/86Sr ratios in carbonate fossils: A case study from the Western Canada sedimentary basin. Geochim. Cosmochim. Acta 61, 2105–2118. doi:http://dx.doi.org/10.1016/S0016-7037(97)00073-2

Holmden, C., Hudson, J.D., 2003. 87Sr / 86Sr and Sr / Ca Investigation of Jurassic molluscs from Scotland : Implications for Paleosalinities and the Sr / Ca Ratio of Seawater 1249–1264. doi:10.1130/B25204.1

Jones, B., 1989. Calcite Rafts, Peloids, And Micrite In Cave Deposits From Cayman Brac, British-West-Indies. Can. J. Earth Sci. 26, 654–664.

Kambesis, P.N., Coke, J.G., 2013. Overview of the Controls on Eogenetic Cave and Karst Development in Quintana Roo, Mexico 5, 347–373. doi:10.1007/978-94-007-5016-6_16

Kottek, M., Grieser, J., Beck, C., Rudolf, B., Rubel, F., 2006. World map of the Köppen-Geiger climate classification updated. Meteorol. Zeitschrift 15, 259–263. doi:10.1127/0941-2948/2006/0130

Kovacs, S.E., Reinhardt, E.G., Stastna, M., Coutino, A., Werner, C., Collins, S. V., Devos, F., Le Maillot, C., 2017. Hurricane Ingrid and Tropical Storm Hanna's effects on the salinity of the coastal aquifer, Quintana Roo, Mexico. J. Hydrol. 551, 703 – 714. doi:10.1016/j.jhydrol.2017.02.024

Kovacs, S.E., Reinhardt, E.G., Werner, C., Kim, S.T., Devos, F., Le Maillot, C., 2017. Seasonal trends in calcite raft formation from Cenotes Rainbow, Feno and Monkey Dust, Quintana Roo, Mexico – Implications for paleoenvironmental studies. *Paleogeo. Paleoclim. Paleoecol. (Submitted:* PALAEO_2017-354)

Lamb, A.L., Wilson G.P., Leng M.J.2006 A review of coastal palaeoclimate and relative sea-level reconstructions using d13C and C/N ratios in organic material, Earth-Science Reviews 75: 29–57

Lazar, B., Sivan, O., Yechieli, Y., Levy, E.J., Antler, G., Gavrieli, I., Stein, M., 2014. Long-term freshening of the Dead Sea brine revealed by porewater Cl− d18O and in ICDP Dead Sea deep-drill. Earth Planet. Sci. Lett. 400, 94–101.

Levinson, A.A., 1968. Oceans (Foundations of Earth Science Series). Elsevier Science. doi:10.1016/0016-7037(68)90037-9

Lighty, R.G., Macintyre, I.G., Stuckenrath, R., 1982. Acropora palmata reef framework: A reliable indicator of sea level in the western atlantic for the past 10,000 years. Coral Reefs 1, 125–130. doi:10.1007/BF00301694

McArthur, J.M., Howarth, R.J., Bailey, T.R., 2001. Strontium isotope stratigraphy: LOWESS Version 3: best fit to the marine Sr-isotope curve for 0–509 Ma and accompanying look-up table for deriving numerical age. J. Geol. 109, 155–170.

McDermott, F., 2004. Palaeo-climate reconstruction from stable isotope variations in speleothems: A review. Quat. Sci. Rev. 23, 901–918. doi:10.1016/j.quascirev.2003.06.021

Medina-Elizalde, M., 2013. A global compilation of coral sea-level benchmarks: Implications and new challenges. Earth Planet. Sci. Lett. 362, 310–318. doi:10.1016/j.epsl.2012.12.001

Medina-Elizalde, M., Burns, S.J., Lea, D.W., Asmerom, Y., von Gunten, L., Polyak, V., Vuille, M., Karmalkar, A., 2010. High resolution stalagmite climate record from the Yucatán Peninsula spanning the Maya terminal classic period. Earth Planet. Sci. Lett. 298, 255–262. doi:10.1016/j.epsl.2010.08.016

Metcalfe, S.E., O'Hara, S.L., Caballero, M., Davies, S.J., 2000. Records of Late Pleistocene-Holocene climatic change in Mexico - A review. Quat. Sci. Rev. 19, 699–721. doi:10.1016/S0277-3791(99)00022-0

Milne, G.A., Mitrovica, J.X., 2008. Searching for eustasy in deglacial sea-level histories. Quat. Sci. Rev. 27, 2292–2302. doi:10.1016/j.quascirev.2008.08.018

Milne, G.A., Peros, M., 2013. Data-model comparison of Holocene sea-level change in the circum-Caribbean region. Glob. Planet. Change 107, 119–131. doi:10.1016/j.gloplacha.2013.04.014

Neuman, B.R., Rahbek, M.L., 2007. Modeling the groundwater catchment of the Sian Ka'an Reserve, Quintana Roo. Assoc. Mex. Cave Stud. Bulletin 1, 1–209.

Peltier, W.R., Fairbanks, R.G., 2006. Global glacial ice volume and Last Glacial Maximum duration from an extended Barbados sea level record. Quat. Sci. Rev. 25, 3322–3337. doi:10.1016/j.quascirev.2006.04.010

Peros, M.C., Reinhardt, E.G., Schwarcz, H.P., Davis, A.M., 2007. High-resolution paleosalinity reconstruction from Laguna de la Leche, north coastal Cuba, using Sr, O, and C isotopes. Palaeogeogr. Palaeoclimatol. Palaeoecol. 245, 535–550. doi:10.1016/j.palaeo.2006.09.006

Perry, E., Paytan, A., Pedersen, B., Velazquez-Oliman, G., 2009. Groundwater geochemistry of the Yucatán Peninsula, Mexico: Constraints on stratigraphy and hydrogeology. J. Hydrol. 367, 27–40. doi:10.1016/j.jhydrol.2008.12.026

Perry, E., Velazquez-Oliman, G., Socki, R. a, 2003. Hydrogeology of the Yucatán Peninsula. Lowl. Maya three Millenn. Human–wildl. interface 115–138.

Pin, C., Bassin, C., 1992. Evaluation of a strontium-specific extraction chromatographic method for isotopic analysis in geological materials. Anal. Chim. Acta 269, 249–255. doi:10.1016/0003-2670(92)85409-Y

Pohlman, J.W., Iliffe, T.M., Cifuentes, L.A., 1997. A stable isotope study of organic cycling and the ecology of an anchialine cave ecosystem. Mar. Ecol. Prog. Ser. 155, 17–27. doi:10.3354/meps155017

Quintana Roo Speleological Survey, 2017. List of Long Underwater Caves in Quintana Roo, Mexico: Tulum, Quintana Roo Speleological Survey.

Reeve, A.S., Perry, E.C., 1994. Carbonate geochemistry and the concentrations of aqueous Mg^2^+, Sr^2^+ and Ca^2^+: Western north coast of the Yucatán, Mexico. Chem. Geol. 112, 105–117. doi:10.1016/0009-2541(94)90107-4

Reimer, P.J., Bard, E., Bayliss, A., Beck, J.W., Blackwell, P.G., Bronk Ramsey, C., Buck, C.E., Cheng, H., Edwards, R.L., Friedrich, M., Grootes, P.M., Guilderson, T.P., Haflidason, H., Hajdas, I., Hatté, C., Heaton, T.J., Hoffmann, D.L., Hogg, A.G., Hughen, K.A., Kaiser, K.F., Kromer, B., Manning, S.W., Niu, M., Reimer, R.W., Richards, D.A., Scott, E.M., Southon, J.R., Staff, R.A., Turney, C.S.M., van der Plicht, J., 2013. IntCal13 and Marine13 Radiocarbon Age Calibration Curves 0–50,000 Years cal BP. Radiocarbon 55, 1869–1887. doi:10.2458/azu_js_rc.55.16947

Reinhardt, E.G., Fitton, R.J., Schwarcz, H.P., 2003. Isotopic (Sr, O, C) indicators of salinity and taphonomy in marginal marine systems. J. Foraminifer. Res. 33, 262–272. doi:10.2113/33.3.262

Reinhardt, E.G., Stanley, D.J., Patterson, R.T., 1998. Strontium isotopic-paleontological method as a high-resolution paleosalinity tool for lagoonal environments. Geology 26, 1003–1006. doi:10.1130/0091-7613(1998)026<1003:SIPMAA>2.3.CO;2

Reinhardt, E.S. 1007%252Fs1093.-017-9944-4. bib. G., Stanley, D.J., Schwarcz, H.P., 2001. Human-Induced Desalinization of Manzala Lagoon, Nile Delta, Egypt: Evidence from Isotopic Analysis of Benthic Invertebrates. J. Coast. Res. 17, 431–442.

Smart, P.L., Beddows, P.A., Coke, J., Doerr, S., Whitaker, F.F., 2006. Cave Development on the Caribbean coast of the Yucatán Peninsula, Quintana Roo, Mexico. Geol. Soc. Am. 2404, 105–128. doi:10.1130/2006.2404(10).

Taylor, M.P., Drysdale, R.N., Carthew, K.D., 2004. The formation and environmental significance of calcite rafts in tropical tufa-depositing rivers of northern Australia. Sedimentology 51, 1089–1101. doi:10.1111/j.1365-3091.2004.00661.x

Taylor, P., Chafetz, H.S., 2004. Floating rafts of calcite crystals in cave pools, central Texas, USA: crystal habit vs. saturation state. J. Sediment. Res. 74, 328–341. doi:10.1306/111603740328

Toscano, M.A., Macintyre, I.G., 2003. Corrected western Atlantic sea-level curve for the last 11,000 years based on calibrated 14C dates from Acropora palmata framework and intertidal mangrove peat. Coral Reefs 22, 257–270. doi:10.1007/s00338-003-0315-4

van Hengstum, P.J., Reinhardt, E.G., Beddows, P.A., Gabriel, J.J., 2010. Linkages between Holocene paleoclimate and paleohydrogeology preserved in a Yucatán underwater cave. Quat. Sci. Rev. 29, 2788–2798. doi:10.1016/j.quascirev.2010.06.034

van Hengstum, P.J., Reinhardt, E.G., Beddows, P. a., Schwarcz, H.P., Gabriel, J.J., 2009. Foraminifera and testate amoebae (thecamoebians) in an anchialine cave: Surface distributions from Aktun Ha (Carwash) cave system, Mexico. Limnol. Oceanogr. 54, 391–396. doi:10.4319/lo.2009.54.1.0391

van Hengstum, P.J., Scott, D.B., Gröcke, D.R., Charette, M.A., Bay, G., 2011. Sea level controls sedimentation and environments in coastal caves and sinkholes 286, 35–50. doi:10.1016/j.margeo.2011.05.004

Ward, W.C., Weidie, A.E., Back, W., 1985. Geology and Hydrogeology of the Yucatán and Quarternary Geology of Northeastern Yucatán Peninsula. New Orleans Geol.Soc. 1–160.

4.9 TABLES

Table 1 - Radiocarbon results from Ich Balam and HN.

Submitter ID		$\delta^{13}C$	Fraction of modern		Radiocarbon age	
		per mil	pMC	1σ error	BP	1σ error
D-AMS 005586	IB-C4 - 1-2cm CR	-5.1	79.45	0.26	1848	26
D-AMS 005587	IB-C4 - 17-18cm CR	-5.7	59.69	0.2	4145	27
D-AMS 005588	IB-C4 - 33-34cm CR	-9.4	55.4	0.2	4744	29
D-AMS 005589	IB-C4 - 49-50cm CR	-8.1	47.54	0.19	5973	32
D-AMS 005590	IB-C4 - 63-64cm CR	-5.4	40.16	0.16	7328	32
D-AMS 005592	HN-C9 - 0-1cm CR	-3.7	35.77	0.16	8258	36
D-AMS 005593	HN-C9 - 10-11cm CR	-4.2	35.35	0.15	8353	34
D-AMS 005594	HN-C9 - 21-22cm CR	-1.6	34.89	0.15	8459	35
D-AMS 005595	HN-C9 - 30-31cm CR	-3.5	34.85	0.14	8468	32
D-AMS 005596	HN-C9 - 43-44cm CR	-6.1	33.66	0.14	8747	33
D-AMS 005597	HN-C9 - 45-46cm CR	-6.3	29.86	0.14	9709	38
D-AMS 006412	IB-C3 - 7-8cm CR	-8.8	40.14	0.16	7332	32
D-AMS 006413	IB-C3 - 21-22cm CR	-10.7	39.09	0.16	7545	33
D-AMS 006414	IB-C5 - 106-107cm CR	-8.7	41.75	0.17	7017	33
D-AMS 006415	IB-C6 - 25-26cm CR	-6.9	50.67	0.2	5461	32
D-AMS 002371	C3 - 8cm SD	-28.9	47.44	0.19	5990	32
D-AMS 002369	C3 - 22cm SD	-33.5	45.08	0.22	6400	39
D-AMS 002373	C5 - 107cm SD	-26.9	47.92	0.21	5909	35
D-AMS 002372	C6 - 26cm SD	-26.4	64.6	0.25	3510	31
D-AMS 005591	C4 - 63-64cm SD	-38.9	46.47	0.19	6156	33
D-AMS 9843	C9 - 46cm SD				8826	31

Table 2 – Measured DIC in the water column of HN.

UCIAMS #	Sample name	Fraction Modern	±	$\Delta^{14}C$ (‰)	±	^{14}C age (BP)	±
136749	14017 sample 04 12m	0.8200	0.0017	-186.3	1.7	1595	20
136750	14017 sample 05 18m	0.8180	0.0019	-188.3	1.9	1615	20
136751	14017 sample 07 28m	0.2186	0.0022	-783.1	2.2	12210	90
136752	14017 sample 09 40m	0.1964	0.0023	-805.1	2.3	13070	100
136753	14017 sample 11 45m	0.1681	0.0024	-833.2	2.4	14330	120

Table 3 – IB-C4 Geochemical data.

Core Position (cm)	Trace Element (counts per second)						$\delta^{13}C$	$\delta^{18}O$	$^{87}Sr / ^{86}Sr$
	Ca		Cl		Sr				
	Mean	Std	Mean	Std	Mean	Std			
0.50	396438.18	39236.01	810.09	388.96	1409.55	120.94			
1.50	454104.45	10843.18	450.00	132.28	1523.55	83.66	-11.7	-6.4	0.70839
2.50	429081.27	13186.21	488.55	34.62	1467.64	92.08			
3.50	423827.18	24657.24	443.00	50.30	1436.55	57.21	-11.4	-6.4	
4.50	428482.09	27259.82	456.18	35.65	1485.09	100.97			
5.50	456779.18	45877.13	425.36	41.63	1385.91	100.96	-11.5	-6.5	0.70828
6.50	548612.91	28010.30	500.27	49.12	1381.27	95.74			
7.50	518168.73	27520.83	455.36	41.70	1455.73	106.61	-11.5	-6.6	
8.50	469019.91	19016.79	406.45	16.51	1515.73	119.27			
9.50	522972.36	22321.08	378.73	28.34	1519.00	59.98	-11.4	-6.5	0.70836
10.50	502111.36	9304.30	460.82	30.96	1627.91	71.28			
11.50	507237.27	23610.05	435.18	24.24	1523.00	93.22	-11.4	-6.4	
12.50	477277.55	28905.42	469.45	31.66	1565.55	74.31			
13.50	452460.73	18280.47	418.82	40.56	1585.09	103.71	-11.3	-6.3	
14.50	461519.91	34182.21	415.36	37.35	1617.64	87.97			
15.50	423234.27	21756.97	474.00	56.10	1608.91	53.16	-11.3	-6.3	
16.50	424503.91	16747.86	499.18	35.89	1573.64	91.13			

17.50	413761.36	19127.94	479.64	20.32	1583.36	86.05	-11.3	-6.3	0.70832
18.50	412379.00	28061.12	342.27	24.00	1632.82	79.87			
19.50	465449.45	18319.96	389.27	29.56	1562.18	76.85	-11.4	-6.5	
20.50	439992.00	26653.94	488.36	31.32	1564.00	78.00			
21.50	459400.18	49033.84	489.45	28.14	1582.09	120.80	-11.3	-6.4	
22.50	437553.27	38450.16	462.18	20.52	1611.73	87.49			
23.50	446653.00	89668.13	407.27	25.94	1551.73	122.64	-11.2	-6.3	
24.50	378336.00	20763.81	508.91	25.04	1617.27	76.39			
25.50	428072.55	15874.46	480.91	48.59	1622.45	48.85	-11.4	-6.4	0.7083
26.50	573464.82	21800.33	425.82	33.24	1517.09	96.79			
27.50	594828.27	14115.60	394.64	20.79	1476.00	91.26	-11.4	-6.5	
28.50	595422.73	15600.79	360.18	31.74	1550.73	109.37			
29.50	609200.18	26265.98	456.00	90.97	1556.18	84.98	-11.4	-6.5	
30.50	591888.73	12336.41	293.00	33.44	1456.36	80.25			
31.50	582061.64	14495.67	426.45	24.39	1528.64	85.16	-11.4	-6.3	
32.50	433615.64	55597.75	423.55	52.77	1555.45	82.02			
33.50	407767.18	84528.46	416.91	26.49	1630.91	88.24	-11.3	-6.4	
34.50	460746.45	24534.33	487.64	50.38	1590.82	73.53			
35.50	526031.18	49683.04	444.64	46.02	1542.82	111.86	-11.4	-6.4	
36.50	522685.73	21538.12	474.18	37.93	1554.45	77.02			
37.50	573386.82	20587.61	433.00	48.62	1551.45	113.47	-11.4	-6.6	

38.50	439706.45	40862.46	432.45	42.54	1696.91	135.37			
39.50	419249.91	37273.67	456.55	35.01	1805.64	75.54	-11.4	-6.7	
40.50	492679.36	20891.29	470.73	21.62	1682.36	111.39			
41.50	501993.36	60249.67	437.64	37.81	1757.09	128.64	-11.5	-6.6	0.7083
42.50	400284.91	22291.62	515.36	33.55	1820.82	87.44			
43.50	513015.73	23959.37	433.73	32.30	1738.45	113.40	-11.5	-6.7	
44.50	460768.45	39188.91	414.45	30.97	1780.09	92.95			
45.50	421820.82	46323.58	416.27	31.62	1902.36	137.30	-11.4	-6.6	0.70828
46.50	503432.18	65794.17	469.73	42.64	1763.73	101.08			
47.50	485300.73	37734.63	424.09	48.50	1767.73	141.18	-11.4	-6.8	
48.50	456720.82	52113.73	438.36	32.74	1739.73	156.14			
49.50	422350.82	73056.33	454.36	42.69	1774.55	106.51	-11.3	-6.4	0.70832
50.50	317478.91	40893.02	410.55	48.41	1946.00	96.30			
51.50	414945.45	83786.39	438.00	46.75	1917.09	171.82	-11.1	-6.3	
52.50	329227.18	44327.62	439.82	50.01	1905.55	166.29			
53.50	319528.55	91117.26	462.18	41.58	1857.27	137.10	-11.2	-6.5	0.70827
54.50	392701.09	20703.27	521.55	28.84	1975.82	105.41			
55.50	308538.00	47011.65	463.36	23.22	2013.73	251.64	-11.5	-6.5	
56.50	316408.09	35105.90	533.64	59.25	1973.27	297.43			
57.50	305667.91	40154.67	512.82	44.14	2146.73	108.81	-11.4	-6.8	0.7082
58.50	360698.82	55548.90	581.18	48.69	2196.18	174.23			

59.50	278588.73	48718.54	604.73	33.59	2090.55	396.38	-11.3	-6.5
60.50	334551.91	47323.32	521.64	21.45	2258.91	361.59		
61.50	354887.36	35401.81	453.64	27.44	2535.64	143.25	-11.1	-6.7
62.50	372437.82	31859.82	542.18	46.88	2743.82	185.28	-11.2	-6.7
63.50	366562.45	20182.71	588.45	27.36	2726.36	72.55	-11.3	-7.0
64.50	337895.00	26896.91	432.18	31.59	2611.00	124.41		

Table 4 – HN-C9 Geochemical data

Core Position (cm)	Trace Element (counts per second)						$\delta^{13}C$	$\delta^{18}O$	$^{87}Sr / ^{86}Sr$
	Ca		Cl		Sr				
	Mean	Std	Mean	Std	Mean	Std			
0.5	522294.45	52370.41	7281.18	2288.75	15086.18	680.32	-8.0	-6.9	0.70847
1.5	579523.09	24547.35	4668.18	210.41	17342.91	889.49			
2.5	573232.82	17757.16	5272.82	245.06	17038.09	1159.20	-7.1	-6.4	
3.5	464477.55	15286.83	10470.45	655.83	20423.55	746.99			
4.5	451912.91	25613.85	9503.36	1121.18	19240.55	1109.32			
5.5	472549.00	28469.95	7191.64	2189.33	18114.45	595.23	-6.2	-6.2	0.70847
6.5	464994.42	34110.66	4919.00	643.58	17699.17	773.41			
7.5	357468.73	24096.30	6783.45	437.38	18994.18	1493.55	-6.1	-6.4	
8.5	390138.09	32079.00	5537.18	724.38	18653.27	1616.34			
9.5	307352.18	45078.37	7621.73	798.41	20468.00	787.66			
10.5	343059.73	33262.44	8001.91	873.85	20971.91	889.06	-6.2	-6.6	0.70851
11.5	304944.82	29755.44	10221.55	979.83	21520.00	425.18			
12.5	244719.27	42325.84	12186.45	1108.01	21741.09	847.87	-7.0	-6.3	
13.5	297301.09	43623.20	11006.82	991.20	21525.55	1227.37			
14.5	281481.45	26092.12	11450.73	1229.47	20421.73	1029.49			
15.5	340181.45	47644.21	8375.55	1673.68	19885.00	690.46	-6.3	-6.5	0.70852
16.5	276564.64	54741.80	5391.82	825.08	20934.82	1138.58			
17.5	338635.55	62683.55	6700.64	787.94	20183.45	901.07	-7.3	-6.6	

18.5	344995.91	11961.37	6865.27	434.90	20332.91	791.88			
19.5	353165.18	33084.77	6914.09	519.08	20175.55	1073.48	-6.8	-6.3	
20.5	357255.18	47769.07	8011.18	1039.89	19257.18	1217.19			
21.5	333738.00	32746.20	6838.36	947.43	20154.18	775.85	-6.5	-6.4	0.70843
22.5	241181.00	24353.09	9330.36	587.32	20590.27	638.48	-5.8	-6.3	
23.5	240850.18	28582.24	10509.45	1164.81	21725.64	1619.98			
24.5	249400.09	21207.92	8397.36	873.86	20016.09	1522.59			
25.5	380582.91	54011.57	5376.36	593.57	17124.82	1180.00	-6.3	-6.5	0.70842
26.5	349817.27	58205.42	5557.91	855.40	17438.27	1888.99			
27.5	404748.00	32448.00	6236.36	1008.55	15202.73	1385.62	-5.4	-6.4	
28.5	445660.09	39311.37	4821.91	833.68	13893.73	947.29			
29.5	378720.55	42259.48	9465.00	771.61	16666.64	498.78			
30.5	383379.91	25587.03	9833.82	868.90	17328.91	699.21	-6.3	-6.7	0.70842
31.5	349184.55	17487.73	9327.09	492.80	17819.91	525.35			
32.5	359712.09	22073.12	11575.91	2000.48	18557.91	1260.05	-6.5	-6.8	
33.5	424401.73	27818.71	9500.09	1713.98	18541.55	1456.99			
34.5	446793.82	32411.16	7608.45	770.06	17135.36	676.79			
35.5	370856.36	39792.14	14872.09	2614.15	18184.00	1118.84	-5.6	-6.5	0.70847
36.5	374656.82	25926.07	7413.18	1134.97	16061.36	2319.52			
37.5	366686.55	26247.01	7534.55	1000.53	12027.91	784.69	-6.4	-6.7	
38.5	484926.18	32361.67	5699.27	682.56	13871.00	1199.34			

39.5	454891.36	8804.78	8524.64	1909.23	15176.27	3072.42			
40.5	553377.64	28375.64	3392.27	374.26	7829.91	992.25	-5.5	-6.7	
41.5	577755.27	27144.65	4370.09	918.52	5248.45	423.08			
42.5	644579.18	11927.66	2082.82	119.10	4593.00	125.64			
43.5	557257.82	26711.35	5313.91	754.44	4685.18	151.18	-7.0	-6.5	0.70847
44.5	422160.73	53605.87	6007.91	682.28	4495.91	208.65			

4.10 FIGURES

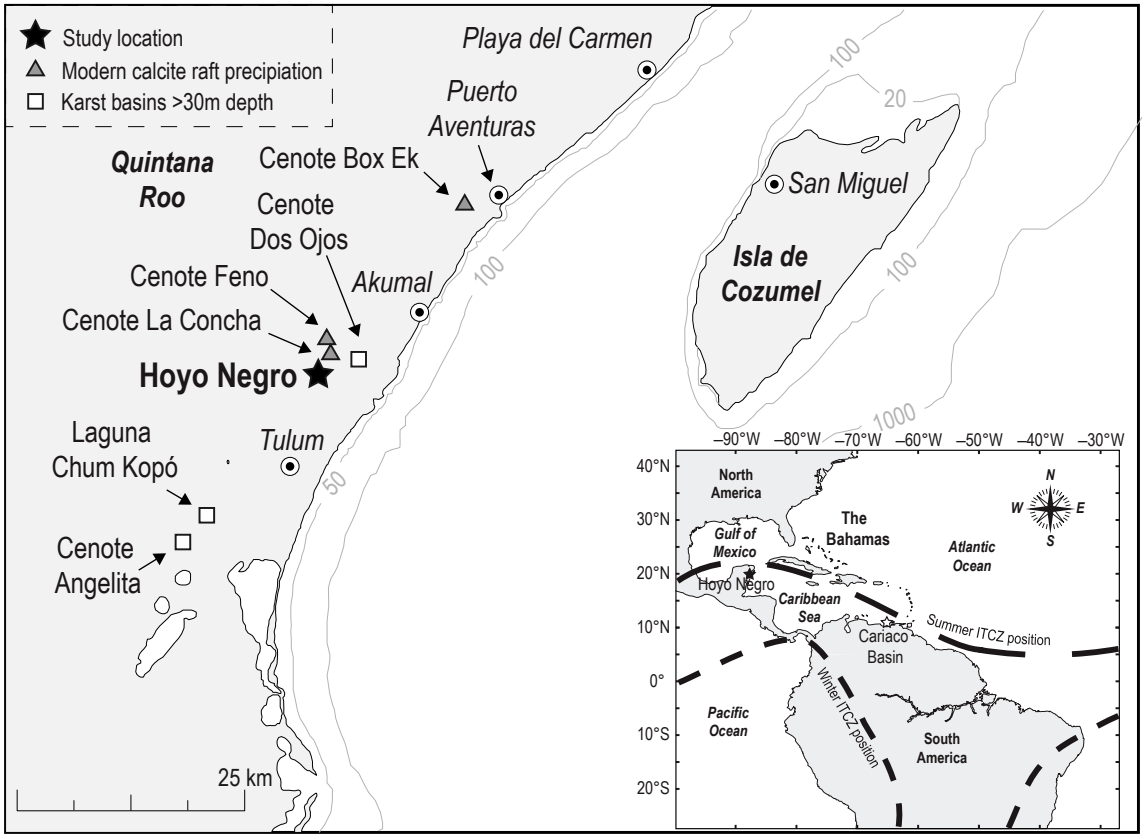

Fig. 1 – Map showing the geographical position of HN, other known deep karst basins (> 30 m water depth), and additional cenotes used in this study. Bathymetric contours are represented in meters. Inset shows location of Cariaco Basin (Venezuela) and the summer/winter position of the Atlantic Intertropical Convergence Zone (ITCZ).

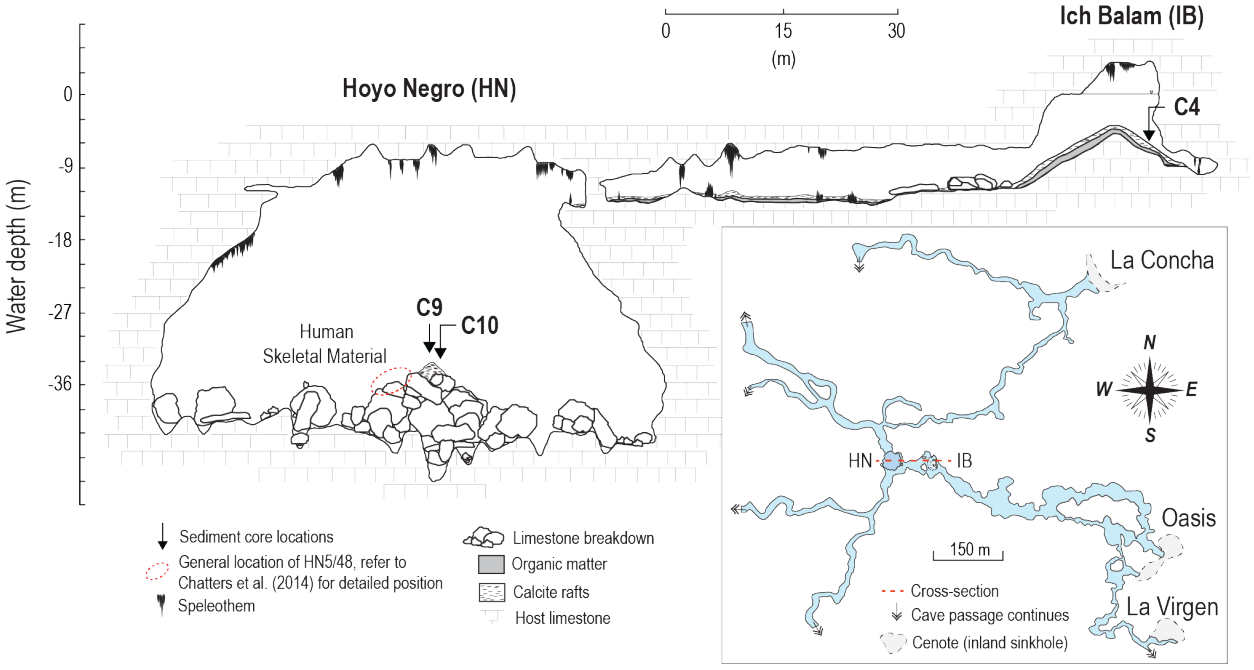

Fig. 2 – Cross-section of the cave system showing core locations. Depths are relative to local water level which is ~ 1 - 2 m above msl (see text for details). Inset shows a plan view of cave passages connecting to HN and cenotes in the immediate area.

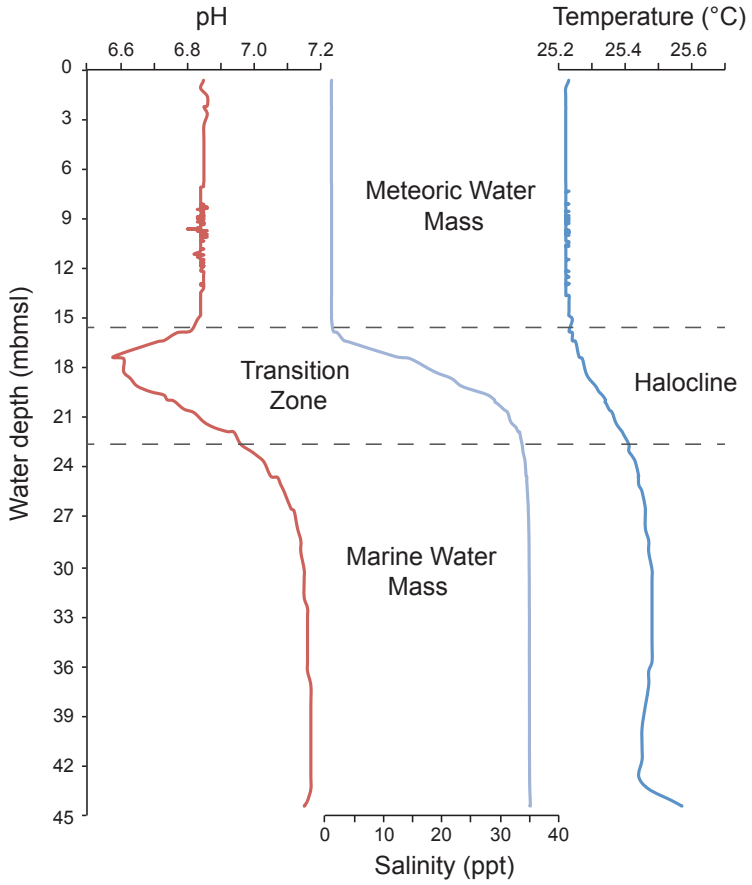

Fig. 3 – HydroLab™ physico-chemical water mass profiles recorded in HN. The halocline transition zone is shown as a hatched line. Depths are relative to local water level.

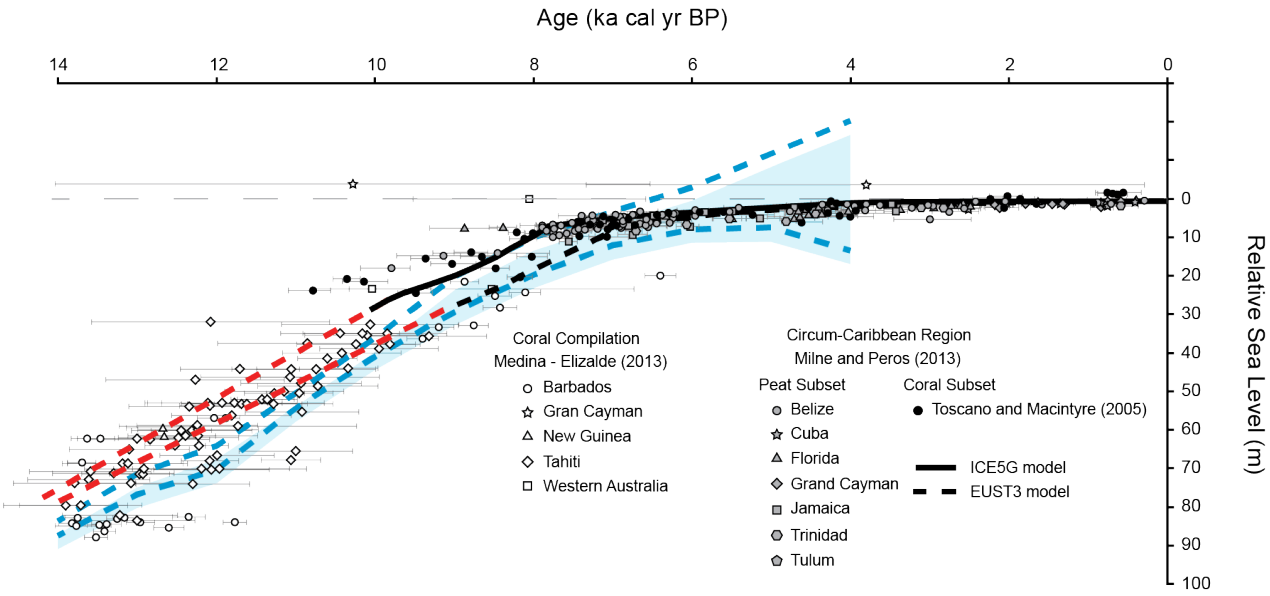

Fig. 4 – Compilation of relative sea-level data used to infer flooding history of HN. Depths are in meters relative to mean sea-level (msl). Data includes peat and coral records (Medina-Elizalde, 2013; Milne and Peros, 2013). The red hatch line represents a linear extrapolation for determining initial flooding (inundation) of the HN. The blue hatch line represents the global relative sea level model (Medina-Elizalde, 2013) while light blue fill represents the glacial isostasy adjustment-corrected model for relative sea level rise (Bard et al., 2010).

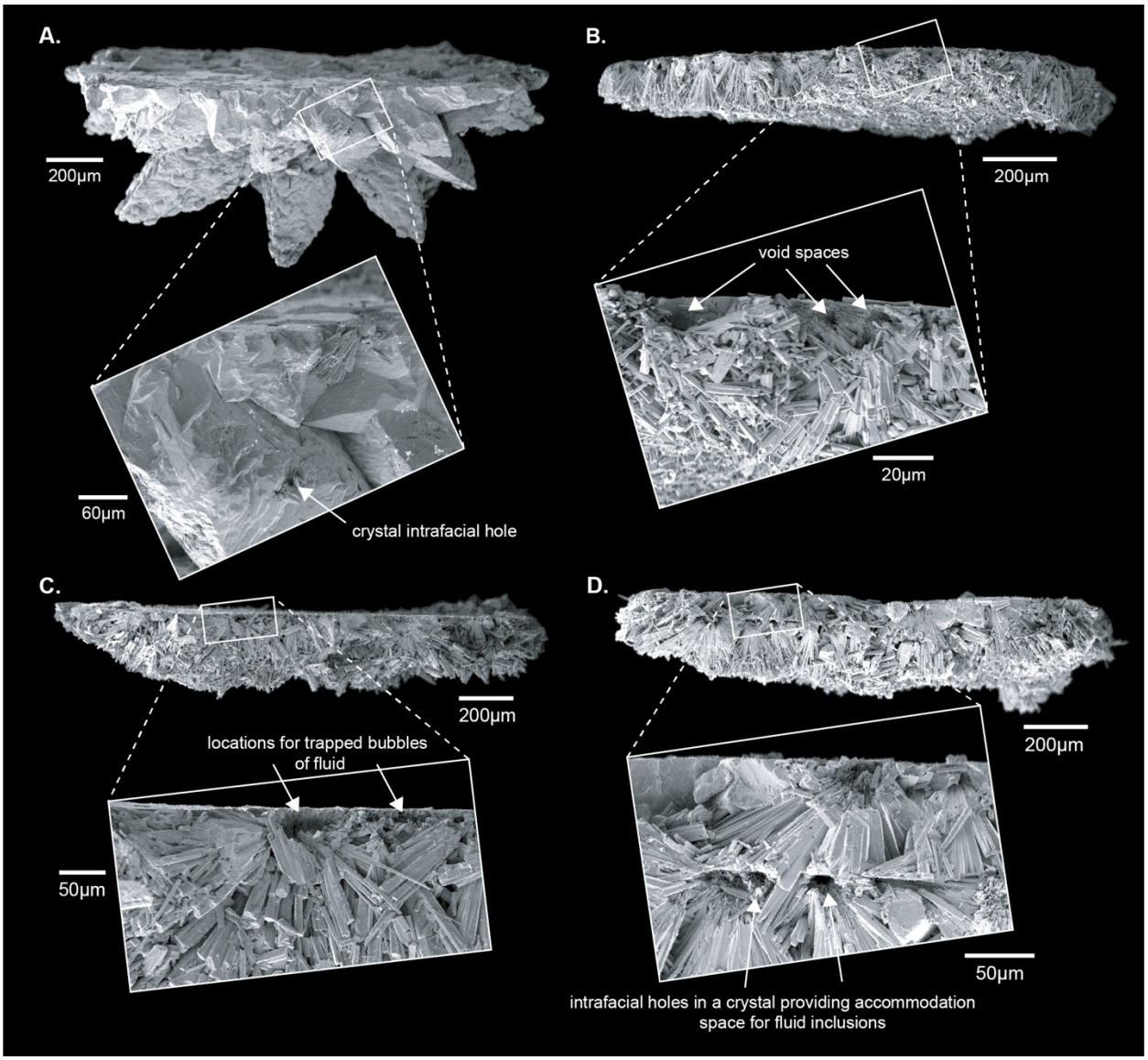

Fig. 5 – Scanning electron microscope (SEM) images showing cross-sectional profiles through calcite rafts from varying depths in C9. Depths were selected at random A) 1-2 cm interval, B) 11-12cm interval, C) 24-25cm interval and D) 33-34cm interval.

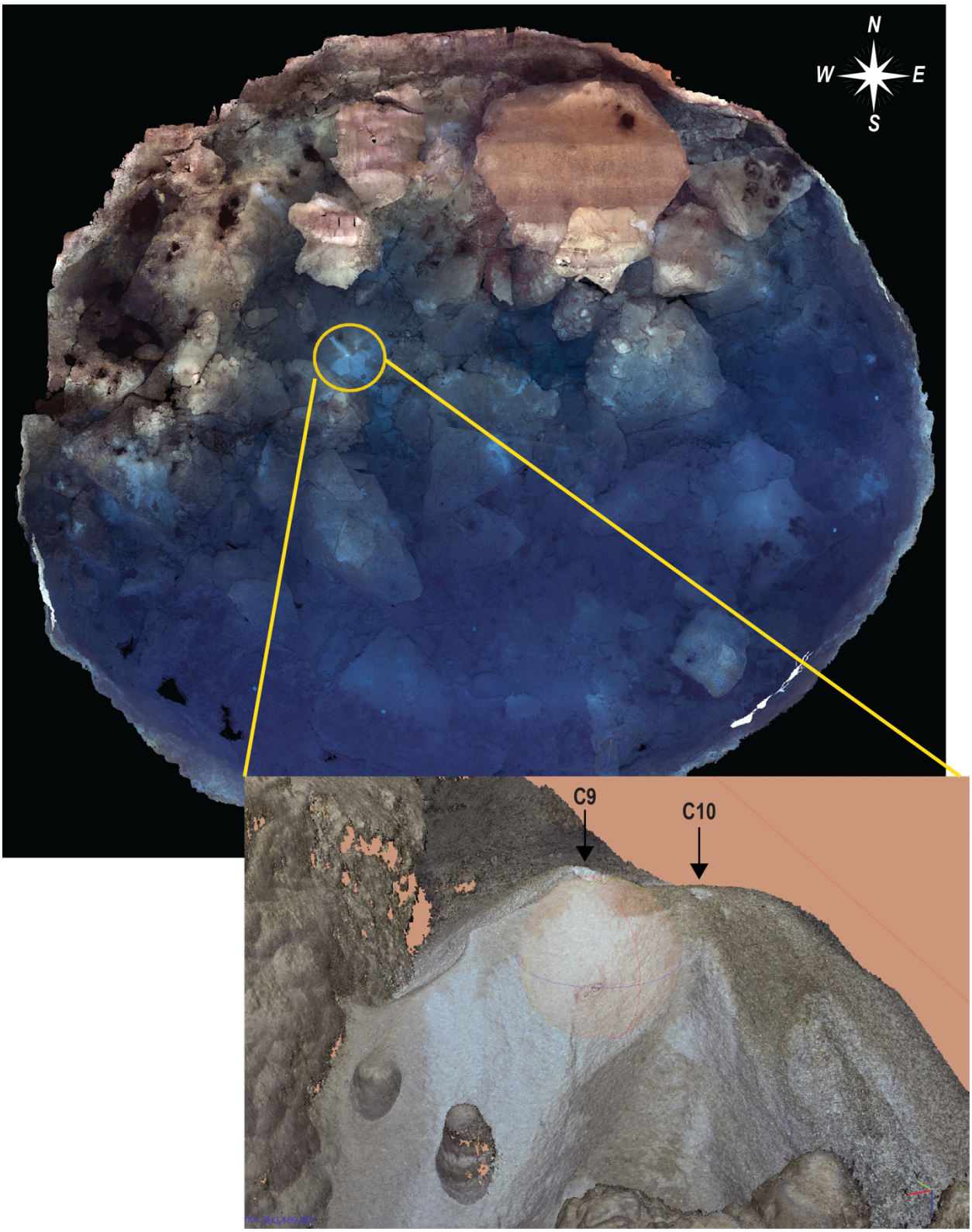

Fig. 6 – Underwater photomosaic of HN compiled from 2200 images aligned on a 3-D model and projected in 2-D. Detailed 3-D image shows the geometry of the calcite raft pile and core locations (C9 and C10). Pit bottom is ~ 62 min diameter.

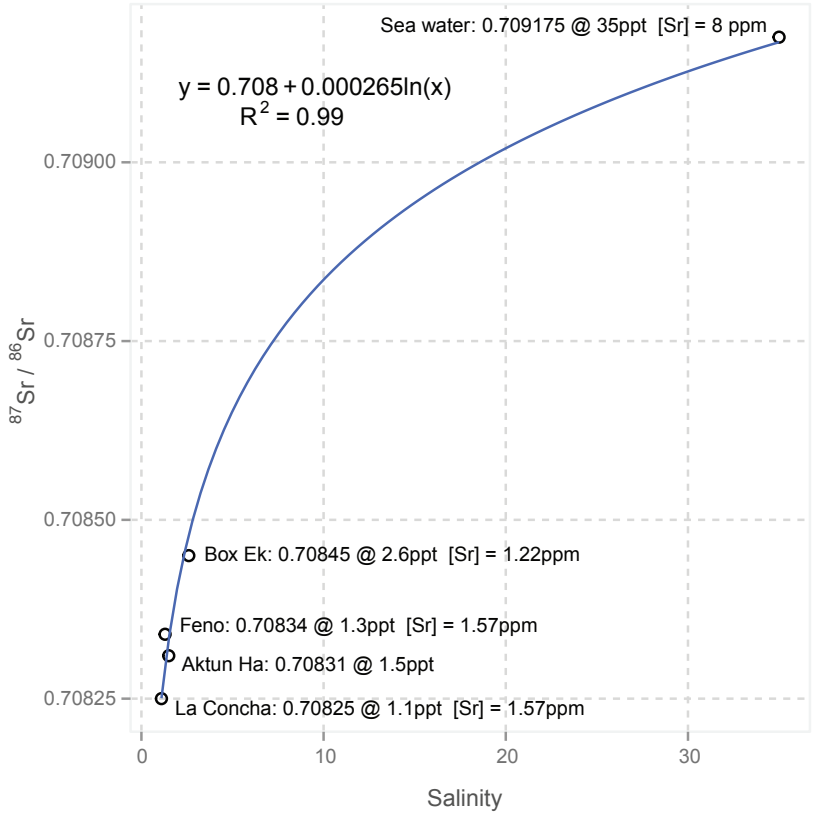

Fig. 7 – Salinity mixing curve empirically compiled with salinity (ppt) and $^{87}Sr/^{86}Sr$ measured from calcite rafts precipitating in nearby cenotes.

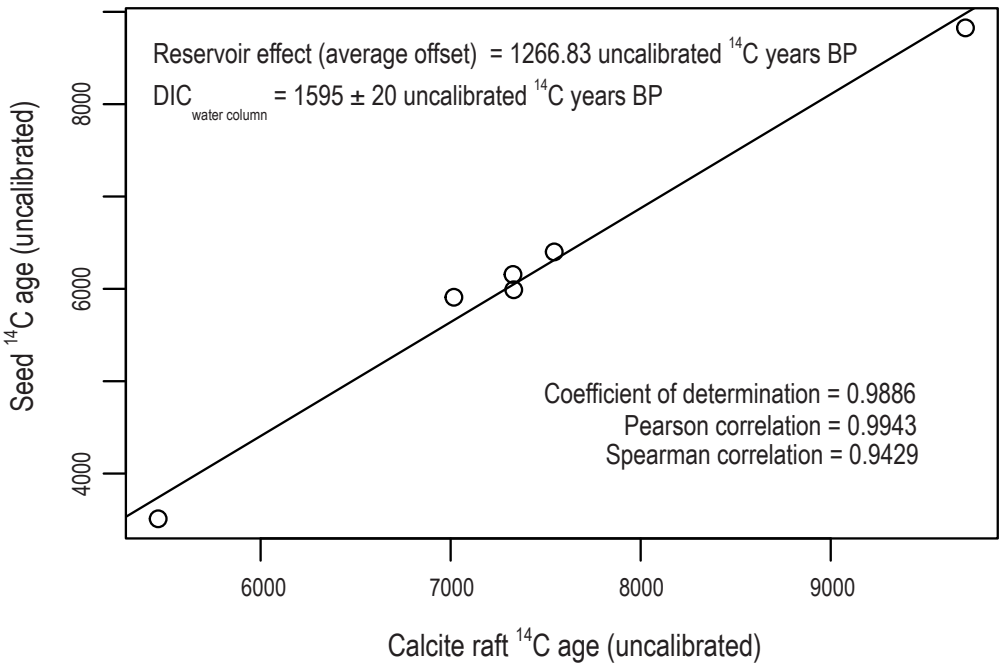

Fig. 8 – Reservoir correction based on paired seed and calcite raft radiocarbon ages from selected intervals using cores C4 and C9 from this study, as well as cores from Collins et al. (2015), (C3, C5, C6; 2015; Table 1).

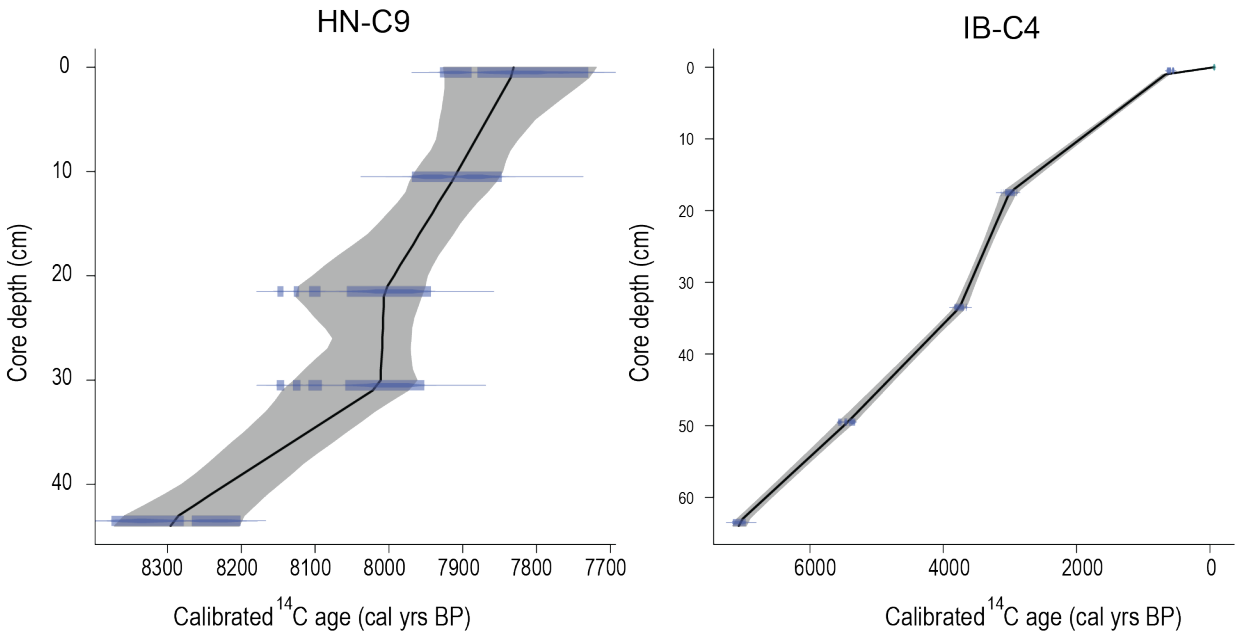

Fig. 9 – Age Models of IB-C4 and HN-C9 produced using Clam 2.1 (R; Blaauw, 2010; Reimer et al., 2013). Grey area represents calibrated age ranges (yrs. BP) at 2σ confidence intervals.

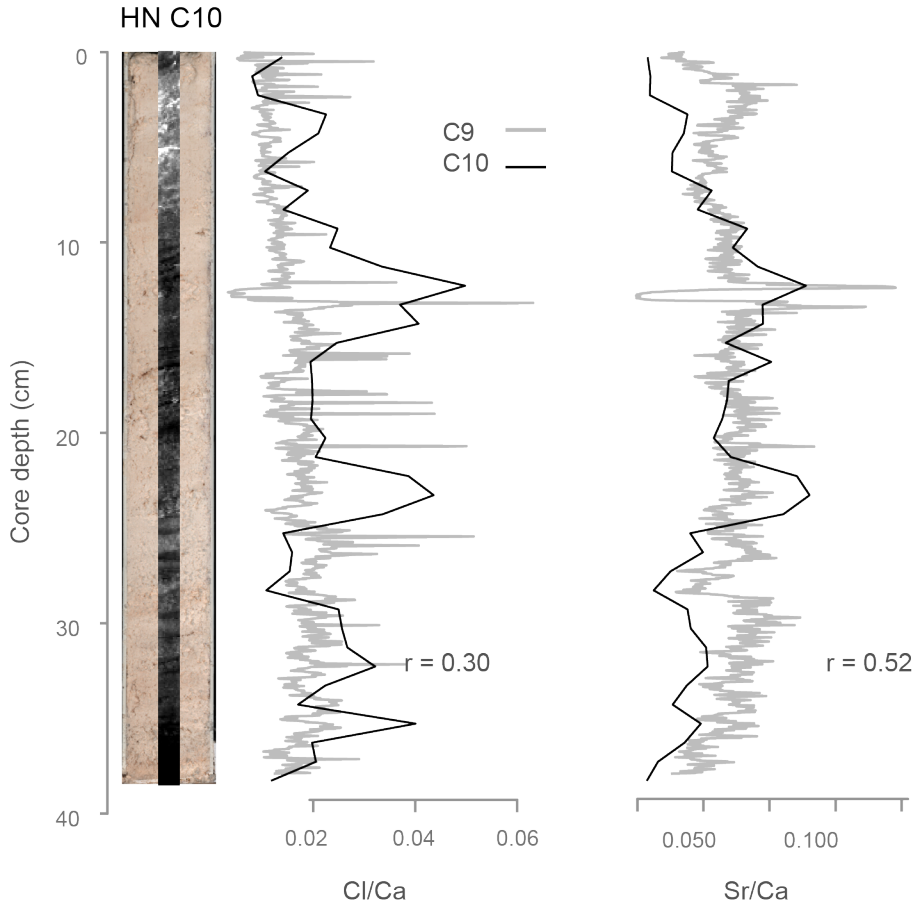

Fig. 10 – Correlation between Cl/Ca and Sr/Ca data in C9 and C10. C9 was analyzed at 1 cm resolution vs. C10 which was intact, and analyzed sampled at 200 μm. Correlation coefficients (r value) between C9 and C10 are also shown. The optical and radiographic image of C10 shows slightly inclined bedding and laminae which is a reflection of calcite rafts accumulating from a point source and forming a cone-shaped pile. There were no cemented or indurated layers within the core.

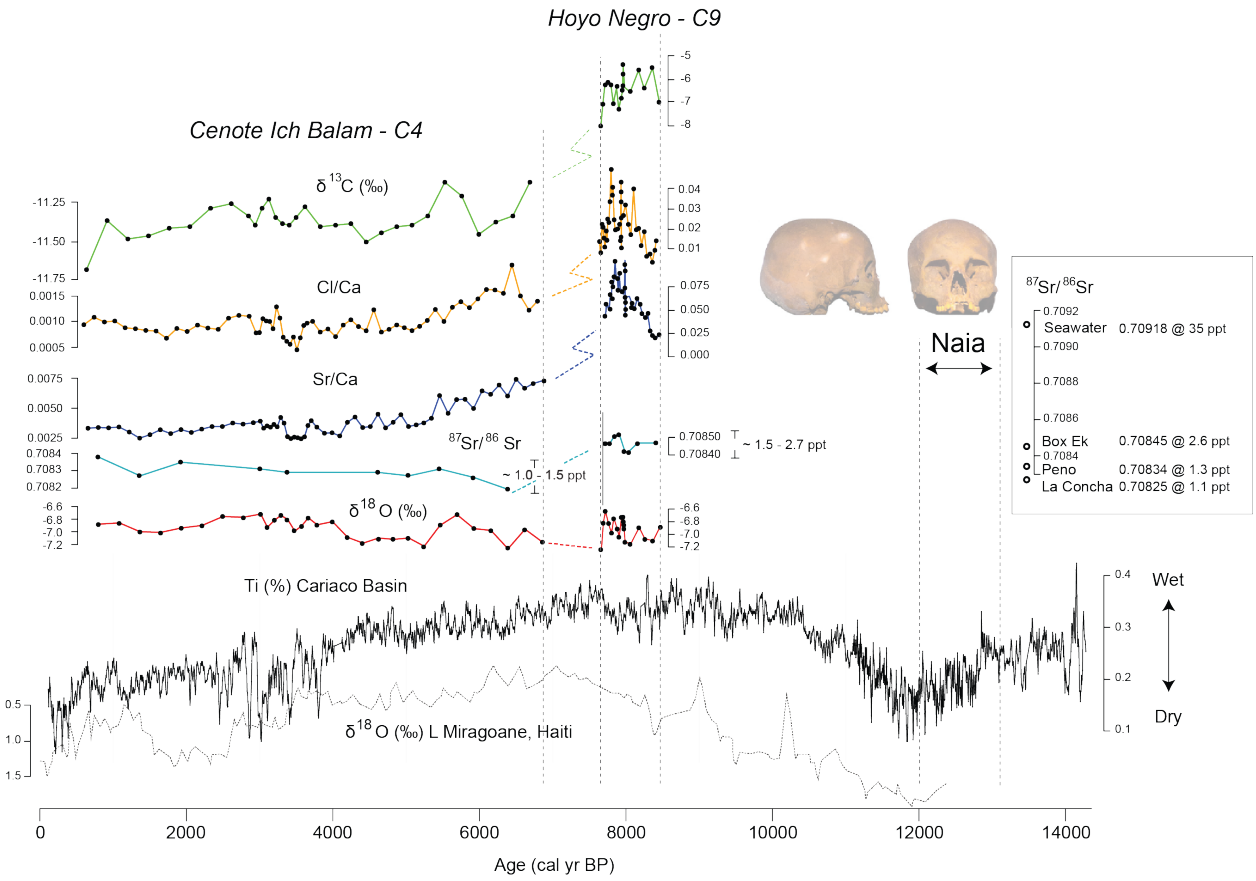

Fig. 11 – Geochemical data for IB and HN plotted vs age (note different scales for C4 and C9) and comparisons with the (Ti) record from the Cariaco Basin (see Fig. 1 for geographical position; Haug et al., 2001) and Lake Miragoane in Haiti (Hodell et al., 1991). Inset figure provides reference to $^{87}Sr/^{86}Sr$ and salinity based on measured values.

CHAPTER 5 – CONCLUSIONS

The anchialine cave environments of the Yucatán Peninsula offer the ideal location to study and assess the forcing mechanisms (climate and sea-level) influencing groundwater conditions. Instrumental monitoring of the accessible meteoric and marine water mass can offer supplementary and/or modern analogues to paleoenvironmental records. Previous work has documented the effectiveness of sedimentary deposits to provide information regarding paleo-environmental change. Calcite rafts, one of the most ubiquitous sedimentary deposits found within these anchialine settings, has received no attention in regards to their potential as a paleohydrological proxy. This dissertation describes the modern interaction between meteoric and marine water masses in response to precipitation events, the contemporary environmental factors influencing calcite raft formation and the development and calibration of calcite raft geochemical as a paleohydrological proxy.

In project one, the 4-year record of water level, salinity and precipitation were used to investigate the seasonal (wet and dry period) interaction between the meteoric and marine water masses as well as how the aquifer salinity responds to precipitation events (scale and frequency). The results provides the first long-term record of groundwater salinity in the Yucatán and describes how salinity in the meteoric WM responds to large precipitation events. The record shows that meteoric water mass salinity is strongly influenced by precipitation and mixing with the underlying marine water mass. Further investigation is needed to understand this relationship as well as to establish spatiotemporal trends in regards to depth and proximity to the coast. However, based on our results, it would be hypothesized that during drier periods with less hurricane activity, the meteoric water mass would be less saline than during wetter periods associated with episodic and intense precipitation (i.e. as caused by hurricanes and tropical

storms). Our results indicate that even though the meteoric water mass may be thicker during the wet periods, induced turbulent mixing will cause an increase in salinity that could render the meteoric WM non-potable. On the contrary, the meteoric water mass would be thinner during dry period but less saline as a result of minimized turbulent flow regimes. Future research should investigate how spatial precipitation patterns and regional differences in hydrology affect this relationship. However, if our hypothesizes holds true and with the predictions of increased hurricane frequency on the Atlantic coast, the groundwater will become increasingly saline. Further studies consisting of additional monitoring and modelling will be needed to understand the range of effects, both on local and regional scale. However, records of this study underline the importance of increased precipitation on groundwater salinity, which can be applied to both paleo-environmental records or predicating future groundwater salinity conditions based on numerical models/simulations.

The second project comprises of a 2-year monitoring study that documented the first record of environmental variables influencing calcite raft formation. Methodology consisted of measuring air temperature, relative humidity, water level, salinity and utilizing sediment traps as well as time-lapse photography (the first time for utilizing visual observations as a record in a cave). Results indicated that calcite rafts precipitate quite consistently (with varying accumulation rates depending on seasonality) throughout the year and deposit on the cave floor despite episodic changes in flow and salinity. Supersaturation of $CaCO_3$ in surface waters is the primary factor influencing calcite raft precipitation, which in turn, is controlled by the intensity and duration of precipitation. Large rainfall events temporarily reduces calcite raft abundance but raft precipitation appears to return within days to weeks after the precipitation event, which is assumed to be when supersaturation of $CaCO_3$ is once again achieved in surface waters. With

the cavern architecture varying across all the monitoring sites, results show that ventilation and size of the cave pool does not influence or inhibit calcite raft precipitation. However future studies should consider employing monitoring stations in cenote environments where calcite raft precipitation is not occurring to understand the characteristics in which would be deemed as unfavorable. An important paleohydrological implication of this study is that accumulation records are expected to be continuous, recording only minor bias due to intense precipitation events.

The third project complemented the conclusions obtained from Project 1 and Project 2 and applied it to the first attempt of calcite rafts as a paleohydrological proxy. Methodology consisted of multiple geochemical analyses including $^{87}Sr/^{86}Sr$, $\delta^{18}O$, $\delta^{13}C$, Sr/Ca and Cl/Ca as well as radiocarbon dating for chronologically constraining the calcite rafts. This was the first study to determine radiocarbon hard water effects based on contemporaneous organic seed and raft deposits. Geochemical records in IB and HN show similar and congruent trends and allow reconstruction of aquifer salinity through the Holocene. Overall, the geochemical results showed that hydrology of the aquifer responded to regional climate with wet periods consistent with higher meteoric water mass salinity vs. drier periods corresponding to less saline conditions. The position of sea-level plays a significant role in regional hydrology which is documented by the overall system shifting during Holocene sea-level rise flooding of the upper passage. Future studies should consider examining the spatial and temporal extent of the variability in the aquifer.

REFERENCES

Alcocer, J., Lugo, A., Marín, L.E., Escobar, E., 1998. Hydrochemistry of waters from five cenotes and evaluation of their suitability for drinking-water supplies, northeastern Yucatán, Mexico. Hydrogeol. J. 6, 293–301. doi:10.1007/s100400050152

Alley, W.M., 2001. Ground Water and Climate. Ground Water 39, 161. doi:10.1111/j.1745-6584.2001.tb02295.x

Back, W., 1995. Water management by early people in the Yucatán, Mexico. Environ. Geol. 25, 239–242. doi:10.1007/BF00766752

Beddows, P.A., 2004. Groundwater Hydrology of a Coastal Conduit Carbonate Aquifer : Caribbean Coast of the Yucatán Peninsula , México. University of Bristol.

Beddows, P.A., Smart, P.L., Whitaker, F.F., Smith, S.L., 2007. Decoupled fresh-saline groundwater circulation of a coastal carbonate aquifer: Spatial patterns of temperature and specific electrical conductivity. J. Hydrol. 346, 18–32. doi:10.1016/j.jhydrol.2007.08.013

Bishop, R.E., Humphreys, W.F., Cukrov, N., Žic, V., Boxshall, G. a., Cukrov, M., Iliffe, T.M., Kršinić, F., Moore, W.S., Pohlman, J.W., Sket, B., 2015. "Anchialine" redefined as a subterranean estuary in a crevicular or cavernous geological setting. J. Crustac. Biol. 35, 511–514. doi:10.1163/1937240X-00002335

Chatters, J.C., Kennett, D.J., Asmerom, Y., Kemp, B.M., Polyak, V., Blank, A.N., Beddows, P.A., Reinhardt, E., Arroyo-Cabrales, J., Bolnick, D.A., Malhi, R.S., Culleton, B.J., Erreguerena, P.L., Rissolo, D., Morell-Hart, S., Stafford, T.W., 2014. Late Pleistocene human skeleton and mtDNA link Paleoamericans and modern Native Americans. Science (80-.). 344, 750–4. doi:10.1126/science.1252619

Collins, S. V., Reinhardt, E.G., Werner, C.L., Le Maillot, C., Devos, F., Meacham, S.S., 2015a. Regional response of the coastal aquifer to Hurricane Ingrid and sedimentation flux in the Yax Chen cave system (Ox Bel Ha) Yucatán, Mexico. Palaeogeogr. Palaeoclimatol. Palaeoecol. 438, 226–238. doi:10.1016/j.palaeo.2015.07.030

Collins, S. V., Reinhardt, E.G., Werner, C.L., Le Maillot, C., Devos, F., Rissolo, D., 2015b. Late Holocene mangrove development and onset of sedimentation in the Yax Chen cave system (Ox Bel Ha) Yucatán, Mexico: Implications for using cave sediments as a sea-level indicator. Palaeogeogr. Palaeoclimatol. Palaeoecol. 438, 124–134. doi:10.1016/j.palaeo.2015.07.042

Coutino, A., Stastna, M., Kovacs, S., Reinhardt, E., 2017. Variations in salinity of the meteoric lens in cave networks on the Yucatán. J. Hydrol. 551, 715 – 729. doi:10.1016/j.jhydrol.2017.04.022

Escolero, O.A., Marin, L.E., Steinich, B., Pacheco, A.J., Cabrera, S.A., Alcocer, J., 2002. Development of a protection strategy of karst limestone aquifers: The Merida Yucatán, Mexico case study. Water Resour. Manag. 16, 351–367. doi:10.1023/A:1021967909293

Fleury, P., Bakalowicz, M., de Marsily, G., 2007. Submarine springs and coastal karst aquifers: A review. J. Hydrol. 339, 79–92. doi:10.1016/j.jhydrol.2007.03.009

Gabriel, J.J., Reinhardt, E.G., van Hengstum, P.J., Beddows, P.A., Peros, M.C., Davidson, D.E., 2009. Palaeoenvironmental evolution of cenote aktun ha (Carwash) on the Yucatán Peninsula, Mexico and its response to holocene sea-level rise. J. Paleolimnol. 42, 199–213. doi:10.1007/s10933-008-9271-x

Gondwe, B.R.N., Lerer, S., Stisen, S., Marín, L., Rebolledo-Vieyra, M., Merediz-Alonso, G., Bauer-Gottwein, P., 2010. Hydrogeology of the south-eastern Yucatán Peninsula: New

insights from water level measurements, geochemistry, geophysics and remote sensing. J. Hydrol. 389, 1–17. doi:10.1016/j.jhydrol.2010.04.044

Gonzalez, S., Hedges, R., Huddart, D., Ohman, J.C., Turner, A., Pompa, A., 2003. Earliest humans in the Americas: new evidence from México. J. Hum. Evol. 44, 379–387. doi:10.1016/S0047-2484(03)00004-6

Kambesis, P.N., Coke, J.G., 2013. Overview of the Controls on Eogenetic Cave and Karst Development in Quintana Roo, Mexico 5, 347–373. doi:10.1007/978-94-007-5016-6_16

Kovacs, S.E., Reinhardt, E.G., Stastna, M., Coutino, A., Werner, C., Collins, S. V., Devos, F., Le Maillot, C., 2017. Hurricane Ingrid and Tropical Storm Hanna's effects on the salinity of the coastal aquifer, Quintana Roo, Mexico. J. Hydrol. 551, 703 – 714. doi:10.1016/j.jhydrol.2017.02.024

Kovacs, S.E., Reinhardt, E.G., Werner, C., Kim, S.T., Devos, F., Le Maillot, C., 2017. Seasonal trends in calcite raft formation from Cenotes Rainbow, Feno and Monkey Dust, Quintana Roo, Mexico – Implications for paleoenvironmental studies. *Paleogeo. Paleoclim. Paleoecol. (Submitted:* PALAEO_2017-354)

Marin, L.E., Perry, E.C., 1994. The hydrogeology and contamination potential of northwestern Yucatán, Mexico. Geofis. Int. doi:10.1016/0148-9062(95)92312-6

Metcalfe, C.D., Beddows, P.A., Bouchot, G.G., Metcalfe, T.L., Li, H., Van Lavieren, H., 2011. Contaminants in the coastal karst aquifer system along the Caribbean coast of the Yucatán Peninsula, Mexico. Environ. Pollut. 159, 991–997. doi:10.1016/j.envpol.2010.11.031

Metcalfe, S.E., O'Hara, S.L., Caballero, M., Davies, S.J., 2000. Records of Late Pleistocene-Holocene climatic change in Mexico - A review. Quat. Sci. Rev. 19, 699–721. doi:10.1016/S0277-3791(99)00022-0

Moore, Y.H., Stoessell, R.K., Easley, D.H., 1992. Fresh-Water/Sea-Water Relationship Within a Ground-Water Flow System, Northeastern Coast of the Yucatán Peninsula. Ground Water 30, 343–350.

Municipalidad de Solidaridad, 2005. Programa director de desarrollo urbano del centro de población Tulum (2002-2026). Actual. Marzo 2005.

Neuman, B.R., Rahbek, M.L., 2007. Modeling the groundwater catchment of the Sian Ka'an Reserve, Quintana Roo. Assoc. Mex. Cave Stud. Bulletin 1, 1–209.

Perry, E., Velazquez-Oliman, G., Socki, R. a, 2003. Hydrogeology of the Yucatán Peninsula. Lowl. Maya three Millenn. Human–wildl. interface 115–138.

Pohlman, J.W., Iliffe, T.M., Cifuentes, L.A., 1997. A stable isotope study of organic cycling and the ecology of an anchialine cave ecosystem. Mar. Ecol. Prog. Ser. 155, 17–27. doi:10.3354/meps155017

Quintana Roo Speleological Survey, 2017. List of Long Underwater Caves in Quintana Roo, Mexico: Tulum, Quintana Roo Speleological Survey.

Smart, P.L., Beddows, P.A., Coke, J., Doerr, S., Whitaker, F.F., 2006. Cave Development on the Caribbean coast of the Yucatán Peninsula, Quintana Roo, Mexico. Geol. Soc. Am. 2404, 105–128. doi:10.1130/2006.2404(10).

Stoessell, R.K., 1995. Dampening of Transverse Dispersion in the Halocline in Karst Limestone in the Northeastern Yucatán Peninsula. Groundwater. doi:10.1111/j.1745-6584.1995.tb00291.x

Stoessell, R.K., Coke, J.G., 2006. An Explanation for the Lack of a Dilute Freshwater Lens in Unconfined Tropical Coastal Aquifers : Yucatán Example. Gulf Coast Assoc. Geol. Soc. Trans. 56, 785–792.

Taylor, M.P., Drysdale, R.N., Carthew, K.D., 2004. The formation and environmental significance of calcite rafts in tropical tufa-depositing rivers of northern Australia. Sedimentology 51, 1089–1101. doi:10.1111/j.1365-3091.2004.00661.x

Taylor, P., Chafetz, H.S., 2004. Floating rafts of calcite crystals in cave pools, central Texas, USA: crystal habit vs. saturation state. J. Sediment. Res. 74, 328–341. doi:10.1306/111603740328

van Hengstum, P.J., Reinhardt, E.G., Beddows, P.A., Gabriel, J.J., 2010. Linkages between Holocene paleoclimate and paleohydrogeology preserved in a Yucatán underwater cave. Quat. Sci. Rev. 29, 2788–2798. doi:10.1016/j.quascirev.2010.06.034

van Hengstum, P.J., Richards, D.A., Onac, B.P., Dorale, J.A., 2015. Coastal caves and sinkholes, in: Handbook of Sea-Level Research. pp. 83–103. doi:10.1002/9781118452547.ch6

van Hengstum, P.J., Scott, D.B., Gröcke, D.R., Charette, M.A., Bay, G., 2011. Sea level controls sedimentation and environments in coastal caves and sinkholes 286, 35–50. doi:10.1016/j.margeo.2011.05.004

Veni, G., 1990. Maya utilization of karst groundwater resources. Environ. Geol. Water Sci. 16, 63–66. doi:10.1007/BF01702224

Werner, C., 2007. Double-Diffusive Fingering in Porous Media. Florida State University.

Whitaker, F.F., Smart, P.L., 1990. Active circulation of saline ground waters in carbonate platforms: Evidence from the Great Bahama Bank. Geology 18, 200–203. doi:10.1130/0091-7613(1990)018<0200:ACOSGW>2.3.CO;2